117
FERMILAB
DEC 19 1997
LIBRARY
JAERI-REVIEW-97-012

JAERI-Review
97-012

PROGRESS REPORT ON NEUTRON SCATTERING RESEARCH
(April 1, 1996 – March 31, 1997)

NAME | DATE | M.S
RETURN TO FERMILAB LIBRARY

October 1997

Fermilab Library
0 1160 0058254 8

(Eds.) Yoshinobu ISHII, Jun-ichi SUZUKI and Satoru FUJIWARA

日本原子力研究所
Japan Atomic Energy Research Institute

本レポートは，日本原子力研究所が不定期に公刊している研究報告書です。
入手の問合わせは，日本原子力研究所研究情報部研究情報課（〒319-11 茨城県那珂郡東海村）あて，お申し越しください。なお，このほかに財団法人原子力弘済会資料センター（〒319-11 茨城県那珂郡東海村日本原子力研究所内）で複写による実費頒布をおこなっております。

This report is issued irregularly.
Inquiries about availability of the reports should be addressed to Research Information Division, Department of Intellectual Resources, Japan Atomic Energy Research Institute, Tokai-mura, Naka-gun, Ibaraki-ken, 319-11, Japan.

© Japan Atomic Energy Research Institute, 1997

編集兼発行　日本原子力研究所
印　　刷　いばらき印刷㈱

JAERI-Review 97-012

中性子散乱成果報告集
（1996年度次報告）

日本原子力研究所先端基礎研究センター
（編）石井　慶信・鈴木　淳市・藤原　　悟

（1997年９月９日受理）

この小冊子は、従来より発行の'JAERI NSL REPORT'を引き継いだものであり、日本原子力研究所の先端基礎研究センターに結集された中性子散乱研究グループ：生体物質中性子回折研究グループ、強相関電子系中性子散乱研究グループ、超低温中性子散乱研究グループの研究を中心に、改３号炉（ＪＲＲ－３Ｍ）を利用した所内の中性子散乱研究、所外との協力研究および共同研究の1996年４月～1997年３月の期間における成果をまとめたものである。

日本原子力研究所（東海駐在）：〒319－11　茨城県那珂郡東海村白方白根２－４

JAERI-Review 97-012

Progress Report on Neutron Scattering Research
(April 1, 1996 - March 31, 1997)

(Eds.) Yoshinobu ISHII, Jun-ichi SUZUKI and Satoru FUJIWARA

Advanced Science Research Center
(Tokai Site)
Japan Atomic Energy Research Institute
Tokai-mura, Naka-gun, Ibaraki-ken

Jaeri, Tokai

(Received September 9, 1997)

The present issue following a previous issue as 'JAERI NSL REPORT' summarizes research progress in neutron scattering at Japan Atomic Energy Research Institute (JAERI) by utilizing the research reactor (JRR-3M) mainly during the period between April 1, 1996 and March 31, 1997.

Keywords: Neutron Scattering, Crystal Structure and Dynamics, Magnetic Structure and Dynamics, Strongly Correlated Electron System, Polymer, and Biology

PREFACE

Neutron scattering research is now coming to a transitional stage where not only the scientific interests but also the research methodologies are gradually changing with their historical inevitability. Applications to the condensed matter physics have been dominated in recent decades but there is an increasing interest in applying neutron scattering to the structural biology research especially because of getting the positions and functions of water molecules surrounding proteins. On the other hand, an international tendency for shifting to the pulsed neutron source is becoming clear after the success in KEK(Japan) and ISIS(UK). A new plan of constructing Neutron Science Research Center in JAERI with an intensive proton beam linear accelerator may be situated along the international current.

The neutron scattering research group in JAERI was rearranged about two years ago with special concerns for these movements and it is now in the Advanced Science Research Center with three groups mentioned in the Section 1. It is widely recognized in these groups that the most important points in such a transitional stage is to pursue advanced and innovative scientific programs with wide and sensitive mind. The readers will find many interesting and suggestive new ideas and results in the present review. At the same time, we are aware of the importance that the key technologies in future should be obtained by improving and brushing up the steady neutron beam technologies around JRR-3M. Many technological attempts now carried in our groups such as an innovative neutron imaging plate, concaved silicon crystal monochromator, WAND spectrometer and ultralow temperature neutron scattering facility now under construction are also shown in this review, and the next problem is how to extend these methods to the pulsed neutron facilities which will be realized in future.

September 19, 1997.

Muneyuki Date

Director
Advanced Science Research Center
Japan Atomic Energy Research Institute

Members of Neutron Scattering Groups ; Neutron Crystallography in Biology Group, Strongly Correlated Electron Systems Group and Neutron Scattering at Ultralow Temperatures Group

Contents

1. Overview of the Research Activity of Neutron Scattering in the Fiscal Year 1996 1
2. Research Reports
2.1 Crystal Structures and Excitations
2.1.1 A Powder Neutron Diffraction Study of $(ND_4)_3D(SO_4)_2$ 9
I. Tamura, Y. Noda and Y. Morii
2.1.2 Neutron Diffraction Study of Proton-conducting Oxides 10
T. Nagasaki, N. Noda, Y. Ishii, T. Matsui and Y. Morii
2.1.3 Structure and Properties of Perovskite-related Transition-metal Oxides 11
Y. Inaguma, D. Iwanaga, M. Itoh, K. Aizawa, Y. Shimojo and Y. Morii
2.1.4 Diffuse Neutron Scattering from Ag_3SI at High and Low Temperatures 12
Aziz K. Jahja, Y. Ishii, N. Minakawa, Y. Hamaguchi, Y. Morii, T. Sakuma and Marsongkohadi
2.1.5 Phonons of RbCl under High Pressure 14
A. Onodera, A. Mori, Y. Ishii, Y. Morii and S. Kawano
2.1.6 Phonon Measurement of RbCl under High Pressure 16
Y. Ishii, A. Mori, A. Onodera, S. Kawano and Y. Morii
2.1.7 Phonon Anomaly of $Ti_{50}Ni_{30}Cu_{20}$ 17
Y. Morii, X. Ren, K. Taniwaki and K. Otsuka
2.1.8 Neutron Powder Diffraction Study of Chalcopyrite, $CuFeS_2$ 18
K. Sugimoto, T. Kobayashi, K. Ishida, S. Kumazawa, Y. Ishii and Y. Morii
2.1.9 Structure of Lithium Titanogallate Prepared by Ion Exchange Reaction 19
Y. Michiue, M. Watanabe, F. Izumi, Y. Morii and Y. Shimojo
2.2 Magnetic Structures and Excitations
2.2.1 Magnetic Structure of $DyCu_2$ 23
Y. Koike, N. Metoki, Y. Morii, Y. Yoshida, R. Settai and Y. Ōnuki
2.2.2 Neutron Diffraction of Helimagnetic $Y(Tb)Mn_2$ 25
M. Shiga, H. Nakamura and N. Metoki
2.2.3 Neutron Scattering Study on $CuGe_{1-x}Si_xO_3$ 26
O. Fujita, J. Akimitsu, S. Katano and M. Nishi
2.2.4 Neutron Diffraction Study on Potassium Uranate KUO_3 28
Y. Hinatsu, N. Nitani, Y. Shimojo and Y. Morii
2.2.5 Magnetic Structure of Orthorhombic Phase in γ-MnT (T=Fe, Pd) Alloys 29
T. Hori, Y. Tsuchiya, Y. Shimojo, H. Shiraishi, S. Funahashi and K. Hojou

2.2.6 Magnetic Diffuse Scattering of $Zn_{1-x}Mn_xTe$ with x=0.432 at B=0 and 5 Tesla 30
K. Sato, Y. Ono, S. Shamoto, Y. Morii, T. Sato, Y. Oka and T. Kajitani
2.2.7 Magnetic and Structural Properties of Reduced Praseodymium Titanates 31
A. Nakamura and K. Yoshii
2.3 Strongly Correlated Electron Systems and Superconductivity
2.3.1 Coupling between Magnetic and Superconducting Order Parameters and Evidence for the Spin Excitation Gap in the Superconducting State of a Heavy Fermion Superconductor UPd_2Al_3 35
N. Metoki, Y. Haga, Y. Koike, N. Aso and Y. Ōnuki
2.3.2 Interplay between Magnetism and Superconductivity in a Heavy Fermion Superconductor UPd_2Al_3 37
Y. Koike, N. Metoki, Y. Haga, Y. Morii and Y. Ōnuki
2.3.3 Anomaly in the Spin Wave Excitation Associated with the Superconductivity in UPd_2Al_3 39
Y. Haga, N. Metoki, Y. Koike and Y. Ōnuki
2.3.4 Magnetic Structure of a Heavy Fermion Superconductor UNi_2Al_3 41
N. Aso, N. Metoki, N. Sato, T. Komatsubara and Y. Endoh
2.3.5 Neutron Scattering Studies of Ternary Uranium Antiferromagnet UNiSn 43
T. Osakabe, T. Takabatake, M. Shirase, E. Yamamoto, Y. Haga and Y. Ōnuki
2.3.6 Magnetic Strucutres of CeP under High Pressure 44
T. Osakabe, M. Kohgi, K. Iwasa, Y. Haga and T. Suzuki
2.3.7 Vortex Lattice Structure in $CeRu_2$ 45
J. Suzuki, N. Metoki, Y. Haga, E. Yamamoto, H. Kadowaki, K. Kakurai, M. Hedo and Y. Ōnuki
2.3.8 Existence of Mesoscopic Structure in $NdBa_2Cu_3O_{7-\delta}$ Observed by Small-angle Neutron Scattering Method 47
S. Miyata, K. Osamura, J. Suzuki, K. Kuroda and N. Koshizuka
2.3.9 Charge Ordering in $Pr_{1-x}Ca_xMnO_3$ 48
O. Hino, N. Ikeda, Y. Yamada, T. Inami and S. Katano
2.3.10 Neutron Scattering Study on the Structure of the S=1/2 Quasi-one-dimensional Magnet $Sr_{14-x}Y_xCu_{24}O_{41}$ 49
M. Matsuda, K. Katsumata, T. Inami and S. Katano
2.3.11 Correlation between Rhombic Distortion and Electronic Anomaly in $La_{1.775}Tb_{0.1}Sr_{0.125}CuO_4$ 50
Y. Koike, T. Adachi, H. Sato and S. Katano
2.4 Amorphous, Liquid and Disordered Materials
2.4.1 Structure of Molten YCl_3-NaCl System by Neutron Diffraction 53
H. Hayashi, Y. Okamoto, T. Ogawa, Y. Tsuchiya and S. Katano

2.4.2 Characterization of Single Crystal Ni-base Superalloy CMSX-4 with Creep Damage 54
K. Aizawa, H. Tomimitsu, H. Tamaki and A. Yoshinari
2.4.3 Characterization of As-deposited Pyrolytie Carbon by Small-angle Neutron Scattering ... 55
K. Aizawa, H. Tomimitsu and T. Iwata
2.4.4 SANS Study on Fe-Cu-Nb-Si-B and Fe-Zr-B-(Cu) Nanocrystalline Alloys 56
M. Ohnuma, K. Hono, H. Onodera and J. Suzuki
2.4.5 Correlation between Medium Range Order and Ionic Conduction in Superionic Conducting Glasses 57
H. Takahashi, T. Sakuma, Y. Nakamura, Y. Shimojo and Y. Ishii
2.5 Polymers
2.5.1 Neutron Scattering Study on Non-Gaussian Behavior for Highly Oriented Copolyester Glass 61
S. Koizumi
2.5.2 Development of Dynamic Data Acquisition System (DDAS) for Small-angle Neutron Scattering 63
S. Suehiro, S. Koizumi, O. Makino and T. Hashimoto
2.5.3 Phase-resolved Neutron Scattering Study of a Semidilute Polymer Solution under Shear Flow 65
S. Saito, S. Suehiro, S. Koizumi, O. Makino, G. Shin and T. Hashimoto
2.5.4 Anomalous Neutron Scattering Behaviors of Polymer Blends near the Glass Transition Temperature 66
H. Takeno, S. Koizumi, H. Hasegawa and T. Hashimoto
2.5.5 Small Angle Neutron Scattering of N-isopropylacrylamide Gel 67
T. Okamoto, Y. Hirokawa, K. Kimishima, H. Jinnai, S. Koizumi and T. Hashimoto
2.5.6 Isothermal Crystallization Mechanism of Isotactic Polystyrene Viewed from Molecular Level 68
K. Tashiro, S. Sasaki, N. Gose and S. Koizumi
2.5.7 Small-angle Neutron Scattering Study of Star-shaped Polystyrenes Having One Deutrium-labeled Arm in Solution 69
A. Takano, A. Fukushi, Y. Isono, S. Koizumi and Y. Morii
2.5.8 Microphase-separated Interfaces of Three-component Triblock Copolymers 70
N. Torikai, Y. Matsushita, N. Metoki and Y. Morii
2.5.9 Heat Induced Gelation of Bovine Serum Albumin 71
Y. Izumi, A. Endo, A. Sakakibara, K. Aizawa, S. Koizumi and H. Tomimitsu
2.6 Biology
2.6.1 An Analysis of Hydrogen-deuterium Exchange Reaction in Cobaloxime Crystals by Single-crystal Neutron Diffraction 75
T. Ohhara, Y. Ohgo, J. Harada, Y. Ohashi, I. Tanaka, S. Kumazawa and N. Niimura

2.6.2 A New Diffractometer for Neutron Crystallography in Biology Using Neutron Imaging Plates 76
S. Fujiwara, Y. Karasawa, I. Tanaka, Y. Minezaki, Y. Yonezawa and N. Niimura

2.7 Instrumentation and Methods

2.7.1 Performance of LLL-neutron Interferometer at PNO 79
Y. Hasegawa, H. Tomimitsu, K. Aizawa and T. Takahashi

2.7.2 Determination of the Scattering Lengths of the Gallium-isotopes by Neutron Interferometry at the PNO in JRR-3M 81
H. Tomimitsu, Y. Hasegawa, K. Aizawa and S. Kikuta

2.7.3 Fabrication and Characterization of NiC/Ti Monochromator with a Period 40 Å 83
K. Soyama

2.7.4 Tunneling Abstraction Reactions of Tritium Atoms with Mixtures of H_2 and D_2 in Super-and Normalfluid ^{3}He-^{4}He Media at 1.3K 84
Y. Aratono, T. Matsumoto, T. Takayanagi, T. Kumada, K. Komaguchi and T. Miyazaki

2.7.5 Performance Test of a System for Generating Triple Extreme Conditions for Neutron Scattering Experiments 86
A. Moriai, S. Ichimura, A. Ohtomo, S. Kawano, S. Fukui, A. Onodera, F. Amita and S. Katano

2.7.6 Development of Liquid ^{4}He Free Dilution Refrigerator for Neutron Scattering 87
Y. Koike, Y. Morii, T. Igarashi and M. Kubota

2.7.7 Polarization Analysis Option on TAS-1 88
T. Inami and S. Katano

2.7.8 Application of Techniques for Intense Beam Reflection to Neutron Monochromator 89
N. Minakawa, Y. Morii, Y. Shimojo and A. Moriai

2.7.9 An Elastically Bent Silicon Monochromator for Neutron Diffractometers
— Thickness Optimization — 90
I. Tanaka and N. Niimura

2.7.10 What to be Considered for Practical Use of Neutron Imaging Plate 91
Y. Karasawa and N. Niimura

2.7.11 Development of Nondestructive Method for Evaluation of Material Strength 93
K. Tanaka, M. Hayashi, K. Inoue, Y. Tsuchiya and N. Minakawa

2.7.12 Residual Strain Measurements of a Heat Treated Steel Pipe 94
K. Inoue, H. Kawashima, J. Sakaguchi, T. Horikawa, N. Minakawa, Y. Tsuchiya, Y. Morii and Y. Yamaguchi

2.7.13 Residual Stress Measurement of Butt-welded Stainless Steel Pipe by Neutron Diffraction 95
S. Okido, M. Hayashi, Y. Morii, N. Minakawa and Y. Tsuchiya

2.7.14 Residual Stress of A Jacket Material for ITER Super-conducting Coil 97
Y. Tsuchiya, N. Minakawa, Y. Morii, T. Kato, H. Nakajima, K. Hamada, I. Watanabe, K. Ishio, T. Abe and H. Tsuji

Appendix A Neutron Scattering Research Committee of 1996 98
Appendix B Themes of Cooperative Research Projects with Universities in JFY 1996 99
Appendix C Themes of Cooperative Research Projects with Private Enterprises and National Laboratories in JFY 1996 101
Appendix D Publication List in the Period of JFY 1996 102
Author Index 105

1. OVERVIEW OF THE RESEARCH ACTIVITY OF NEUTRON SCATTERING IN THE FISCAL YEAR 1996

Since the JRR-3 was upgraded for neutron beam researches in 1990, the Neutron Scattering Laboratory (NSL) of Japan Atomic Energy Research Institute (JAERI) has intensively worked for construction of the seven neutron scattering instruments and has conducted researches on basic science and materials science by means of neutron scattering. Another group for the study on structural analysis of biological crystals was established in Advanced Science Research Center (ASRC) in 1993.

At the beginning of FY 1996, the members of NSL moved to ASRC. As a result, most of the neutron scattering staffs in JAERI are unified under M. Date, the director of ASRC. Members are introduced in the photograph at the first page of this booklet. They consist of three groups for 1) neutron crystallography in biology, 2) neutron scattering of strongly correlated electron systems and 3) neutron scattering at ultralow temperatures as shown in Fig.1.

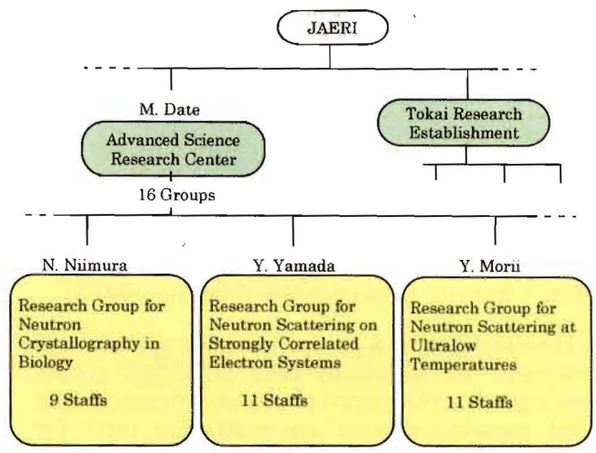

Fig. 1. Organization related neutron scattering groups in JAERI.

Our neutron scattering instruments installed at the JRR-3M are shown in Fig. 2. Four instruments, HRPD, BIX-I, TAS-1 and PNO, are in the reactor hall. In the guide hall, five instruments, RESA, BIX-II, TAS-2, LTAS and SANS-J, are installed. The specifications of most of these instruments are summarized in the "Current status of the neutron scattering facility at NSL-JAERI" (JAERI-memo 8-36). Recently some parts of the TAS-2 were replaced by non-magnetic materials for projected experiments under high magnetic field in near future. A new instrument LTAS (Low-energy Triple-Axis Spectrometer) has been running for users to study magnetic materials, strongly correlated electron systems and super ionic conductors. The typical specifications of this spectrometer are as follows; 1) neutron incident energy, E_i: 2 meV-15.6 meV, 2) total neutron flux : $\approx 1 \times 10^7$ n/cm^2/sec, 3) energy resolutions : 14 μeV at E_i = 2 meV and 183 μeV at E_i = 5 meV. For SANS, "Dynamic data acquisition system" is being developed. This system will greatly extend the capability of the present SANS-J for studies on non-equilibrium phenomena. The BIX-II is in a tuning status of the acquisition of the fundamental data of this diffractometer. This instrument will be commissioned for users at the beginning of next year.

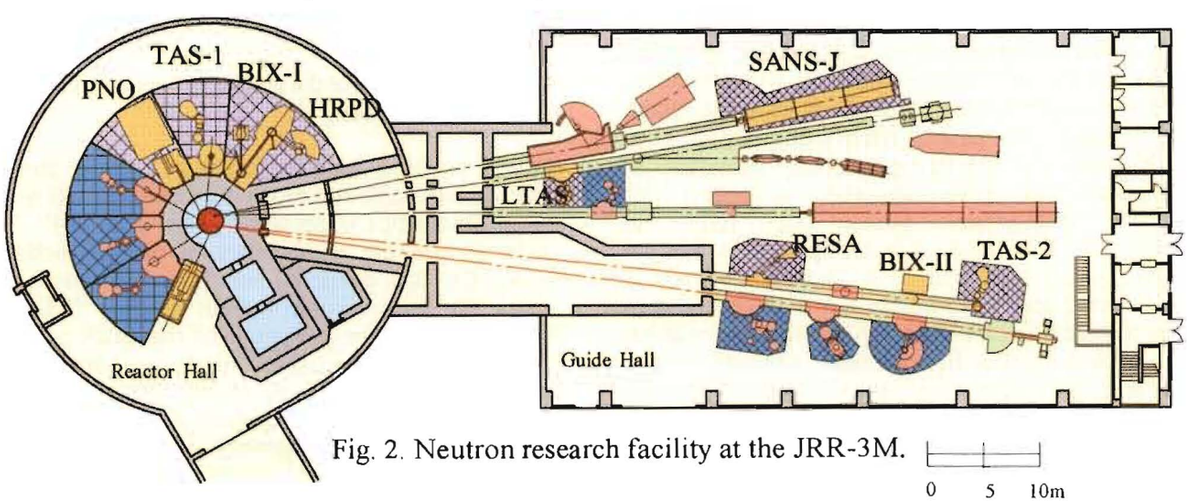

Fig. 2. Neutron research facility at the JRR-3M.

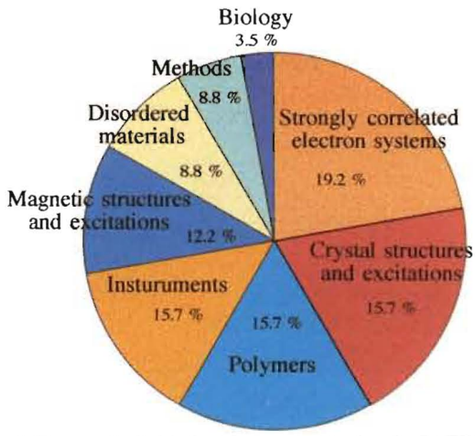

Fig. 3. Research fields in neutron scattering in JAERI.

Development of a monochromator system is in progress. An elastically bent Si perfect crystal has a good performance of monochromation. The bent monochromators are practically used for HRPD, BIX-I, BIX-II and RESA.

Auxiliary equipments have been developed for neutron scattering experiments. These include a ^{3}He cryostat with a 6 T vertical field magnet, a 5 T horizontal field cryomagnet (1.5 K), an 'Orange cryostat' with an insert which can install a clamp-type high-pressure cell, and a dilution refrigerator cooling down to 10 mK with 5 T vertical field. The insert of this dilution refrigerator can set a small non-magnetic high-pressure cell. A development of a 10 T magnet which is cooled by closed cycle refrigerators (a liquid He-free superconducting magnet) is now in progress. A high pressure cell using sapphire anvils (up to 6 GPa) is also under development.

The research reactor, JRR-3M, ran in a rather good condition during the planned operation cycles (7 cycles, 4 weeks/cycle) except for 17 days which were required to repair the vacuum seal of a cold neutron system. As a result, the available beam time of the SANS-J and the LTAS installed at the cold neutron guides, C1 and C3, was 139 days and for the other instruments was 158 days.

Thirty eight research proposals were conducted by the three groups and other staffs in JAERI in JFY 1996. For the complementary research, 20 proposals with universities and 4 proposals with private enterprises which are listed in APPENDIX B were also conducted. In this report, progress reports of all research proposals mentioned above are submitted. Figure 3 shows the research field of the reports in this booklet. As shown in this figure, main interests of our groups are structures and excitation in the strongly correlated electron systems, crystal structures of solids and biological materials, and magnetic structures of solids.

Some highlights of the activities in this reporting period are briefly described by each group as follows.

Research group of neutron crystallography in biology

Neutron diffraction provides an experimental method of directly locating hydrogen atoms in biological macromolecules which dominate the structure-function relationship of proteins, viruses, t-RNA and DNA. We have constructed two kinds of dedicated diffractometers for neutron crystallography in biology. The most serious disadvantage of neutron diffraction is the low flux of neutrons irradiated on the sample. In order to overcome the intensity problem, three points have been considered carefully. These are 1) how to get intense neutron flux on a sample position, 2) how to get a large area detector system, and 3) how to get a large single crystal.

The requirements on the monochromator for neutron crystallography in biology are as follows: Since a single crystal of the biological macromolecules is small, a neutron beam size at the sample position must be less than 5mm x 5mm, and since the unit cell dimension is about 10 nm, beam divergence is preferably less than 0.4°. In order to meet the requirement of the monochromator for this purpose, we have designed an elastically bent silicon perfect crystal (EBSi). Figure 4 shows the prototype of the EBSi monochromator, and 3 pieces of silicon are bent elastically by tensioned piano wires. The diffracted intensity increases by bending the crystal. The basic research for optimization of EBSi is still in

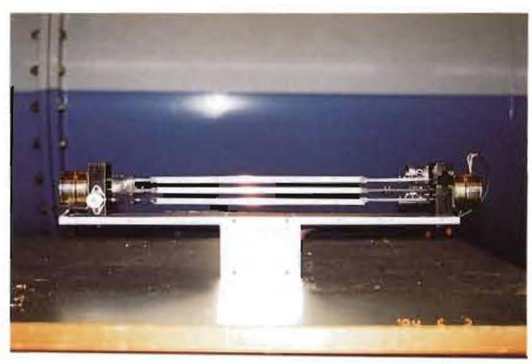

Fig.4. The prototype of the elastically bent silicon perfect crystal monochromator.

progress and the preliminary results on Si thickness optimization were given in the report.

We have also developed a neutron imaging plate (NIP), where neutron converter, ^{6}Li or Gd are mixed with photostimulated luminescence (PSL) material. The properties are wide dynamic range 1 to 10^5 and spatial resolution better than 0.2 mm. The virtual efficiency of the NIP is correlated with the kind of a neutron converter, the molar ratio of PSL material to neutron converter, the NIP thickness and neutron wavelength. The NIP optimization has been carried out by changing the above parameters. Although the NIP is an effective detector applicable for neutron beam experiments, we found several problems to be solved, which are 1) neutron wavelength dependence, 2) γ-ray sensitivity and 3) the effect of the radioactive products created by irradiated neutron. These effects have been examined and reported.

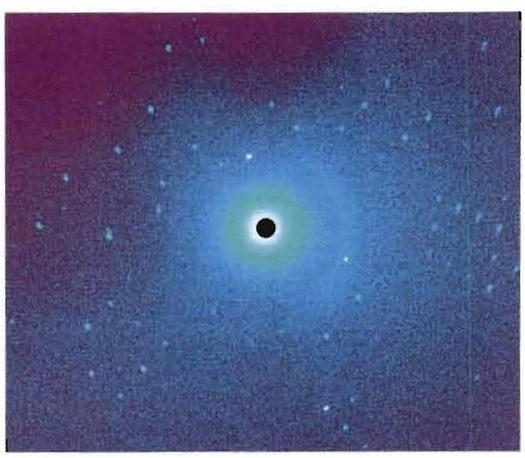

Fig.5. The neutron diffraction pattern from the triclinic form of hen egg-white lysozyme obtained by 1.0° crystal oscillation for 20 hours.

The BIX-I has been constructed and utilized in neutron structure analysis. The neutron flux at the sample position was 5.9 x 10^6 n/cm^2/sec or 1.4 x 10^6 n/cm^2/sec when the EBSi (111) or (220) was used, respectively. Two sets of ^{3}He-area detectors (active area: 250 x 250 mm^2, spatial resolution: 2mm) are equipped. We have constructed a new diffractometer, BIX-II, dedicated to neutron crystallography in biology equipped with the optimized NIP. The performance of the BIX-II is summarized in this report and one of the preliminary results is shown in Fig.5.

An analysis of hydrogen-deuterium exchange reaction in cobaloxime crystals has been carried out by using the BIX-I. Neutron diffraction experiments from hen egg-white lysozyme (tetragonal form) have been carried out by using the BIX-I. Neutron diffraction experiments from hen egg-white lysozyme (triclinic form) have been carried out by using the BIX-II.

Neutron Laue diffraction 2Å data (a total number of 38,278 reflections) from tetragonal hen

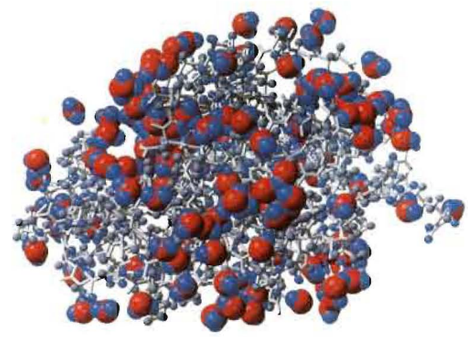

Fig.6. The structure of hen egg-white lysozyme determined by neutron diffraction. 960 hydrogen atoms in the molecule and 157 bound water molecules were successfully identified.

egg-white lysozyme were collected for 10 days with neutron imaging plates in a Laue diffractometer (LADI) at the Institut Laue-Langevin, Grenoble. The X-PLOR program which is commonly used for the X-ray protein crystallography refinement has been successfully modified for neutron crystallography refinement by introducing hydrogen (deuterium) atoms. 960 hydrogen atoms in the molecule and 157 bound water molecules were successfully identified as shown in Fig. 6.

Research group for neutron scattering on strongly correlated electron systems

Correlations between magnetism and superconductivity in UPd_2Al_3 (5f-electron systems) have been studied. The intensity of an antiferromagnetic peak decreases at below the superconducting transition temperature of 2 K, which indicates a coupling between magnetic and superconducting order parameters. Magnetic excitation gap has also been observed in its superconducting state. Figure 7 shows the intensity map in the Q-ΔE space for 4.2 K and 0.4 K. As is clearly seen in the figure for 0.4 K, the excitation gap appears at around 0.4 meV for Q = (0 0 1/2), and this excitation shows a dispersion relation with a minimum energy at this Q. These results

indicate that the antiferromagnetic spin fluctuations can be an origin of the superconductivity of this system.

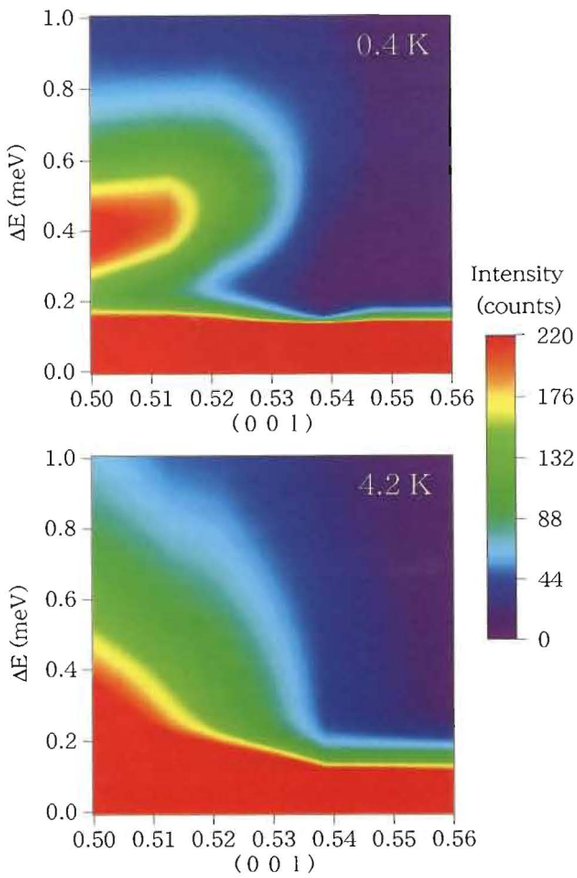

Fig. 7. Intensity map in the Q-E space for 4.2 K and 0.4 K of the UPd_2Al_3 compound. The superconducting transition temperature is 2 K.

Crystal field excitations were observed in UNiSn. The excitation energies are about 10 and 40 meV, and these can explain the magnetic susceptibility of this compound. The result shows that 5f electrons in this uranium compound are rather localized.

In 3d electron systems, structural transitions in perovskite manganites $(La,Sr)MnO_3$ and $(Pr,Ca)MnO_3$, showing colossal magnetoresistance, have been extensively studied. Figure 8 shows the satellite reflections observed in $La_{1-x}Sr_xMnO_3$ (x = 0.1 and 0.15) at 10 K. The result indicates that holes introduced by the Sr substitution form a new lattice and localize at low temperatures. (Pr, Ca) manganites also reveal similar hole orderings. However, their ordering patterns are different from those in $(La,Sr)MnO_3$. The formation of the hole lattices was explained

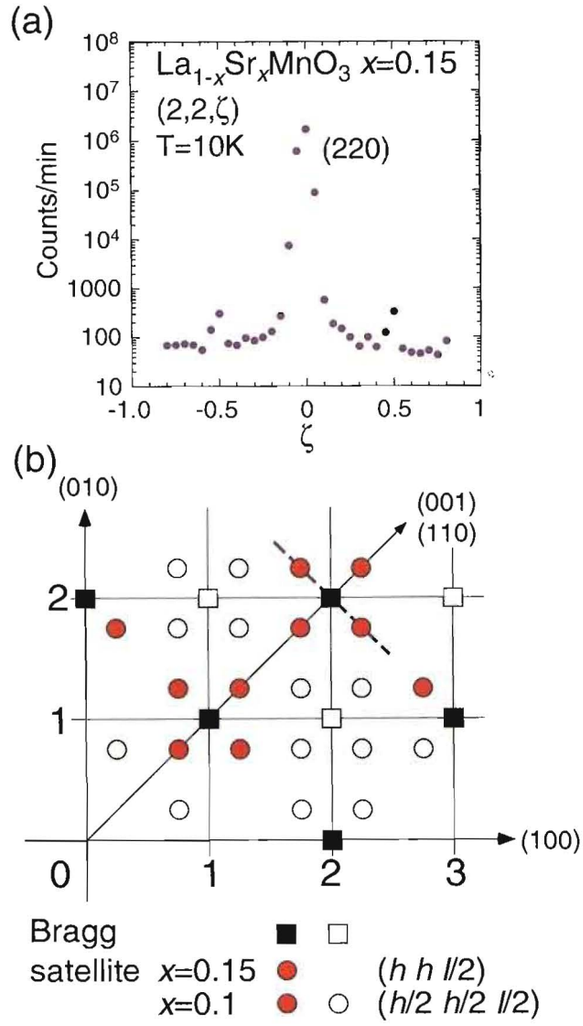

Fig. 8. (a). Satellite peaks observed in $La_{1-x}Sr_xMnO$ (x 0.15). (b). Observed satellite peaks shown in a reciprocal lattice plane. Solid and open squares are Bragg reflections which comes from (hk0) plane. Bragg reflections in (hhl) plane are omitted. Red circles indicate satellite points observed in x = 0.15 sample. Red and open circles are in x = 0.1 sample. Broken line shows the scan range in (a).

by orderings of polarons accompanied by Jahn-Teller distortions. A doping effect on the spin-Peierls transition of $CuGeO_3$ was also studied. With the substitution of Ge by a small amount of Si, the original spin-Peierls state is greatly affected and the antiferromagnetic ordering turns up. Neutron scattering experiments suggest a co-

existence of these spin-Peierls dimerization and antiferromagnetism. The phase diagram for the Si concentration was obtained.

Magnetic flux lattices of a superconductor $CeRu_2$ has been studied in connection with the peak effect in its magnetization. Through this work unusual field dependence of the flux lattices - a difference in the formations of the flux lattices between in a field cooled and in a zero-field cooled run, etc.- were observed.

The structural relaxation in the glassy state of the highly-oriented random copolyester, Vectra, has been investigated. The local relaxation shows distinctive anharmonisities depending on its spatial anisotropy of this material.

Research group for neutron scattering at ultralow temperatures

The research is developing a new type of dilution refrigerator (DR) which has not a 1K-pot but a pulse tube refrigerator to liquefy ^3He-^4He mixture gas. We have designed a DR named "mK cryocooler" and made a prototype of refrigerator to develop.

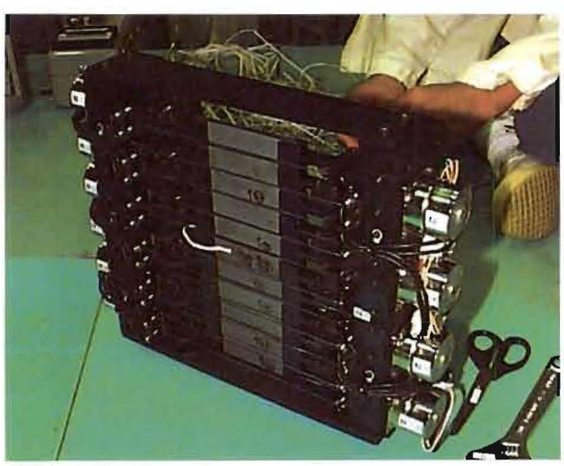

Fig. 9. Photograph of a monochromator of HRPD.

The group also develops various kind of neutron scattering techniques. A high resolution powder diffractometer, HRPD, was installed at the 1G beam port. HRPD is equipped with Ge331 focusing monochromator which provides wavelength of 0.182 nm and beam intensity of 1 x 10^5 n/cm^2/sec at the sample position for a high spatial resolution ($\Delta d/d = 2 \times 10^{-3}$) analysis. To observe magnetic peaks at lower scattering angles, we recently made a monochromator shown in Fig. 9. The monochromator consists of eleven bent silicon slabs with 311 reflection enables us to focus neutrons both horizontally and vertically. The neutron intensity obtained by the monochromator was about 45 % of that of pyrolytic graphite, which was quite good and could be improved in future. Crystal structures and/or magnetic structures of permanent magnet material Y_2Fe_{17}, dielectric material $(ND_4)_3D(SO_4)_2$, functional oxides Ba_2CuWO_6 and $SrCe_{0.95}Yb_{0.05}O_3$, uranium compound KUO_3 and others have been studied.

Phonon anomalies related to structural phase transitions of RbCl at 4.9 kbar at ambient temperature, and Ti-Ni-Cu alloy at 320 K at ambient pressure were studied.

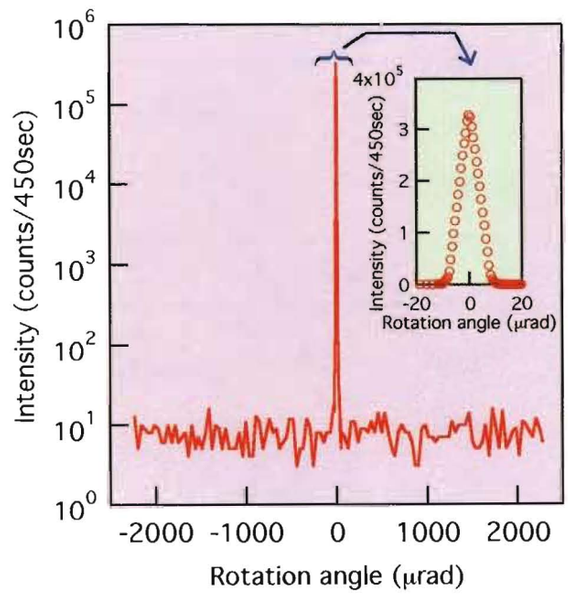

Fig. 10. A rocking curve profile of the second channel-cut silicon of the double crystal diffractometer.

Methods of very small-angle neutron scattering have been developed with a double crystal diffractometer (DCD) at the apparatus for Precise Neutron Optics (PNO) at the 3G beam port. Channel-cut silicon perfect single crystals with (5,-5) setting at λ=0.25 nm were used. The obtained peak intensity of the second silicon rocking curve without sample was about 1000 cps and signal to noise ratio was 3.9 x 10^4 as shown in Fig. 10. Porous structure of as-deposited pyrolytic carbon was studied using the DCD in the q range from 2 x 10^{-2} nm^{-1} to 2 x 10^{-4} nm^{-1} which extends that of the SANS-J. The PNO has also been used for interferometry experiments to evaluate neutron scattering amplitude of Ga isotopes and for neutron topography experiments to

observe single crystal imperfection of the industrial products such as turbine blades made of Ni-based superalloy.

Residual stress analysis has been carried out with the diffractometer, RESA, at the T2-1 beam port. Neutron beam size and intensity of the RESA are 1 to 20 mm^2 and 10^5 n/cm^2sec, respectively. A jacket material INCOLOY-908 of the central solenoid superconducting coil of the experimental fusion reactor ITER was investigated. Figure 11 shows that evaluated tensile residual stress exceeds 200 MPa in some areas inside the jacket which would cause a fracture due to stress accelerated grain boundary oxidation. Residual stress in welded joint of stainless steel tube and steel pipe for oil well was also studied

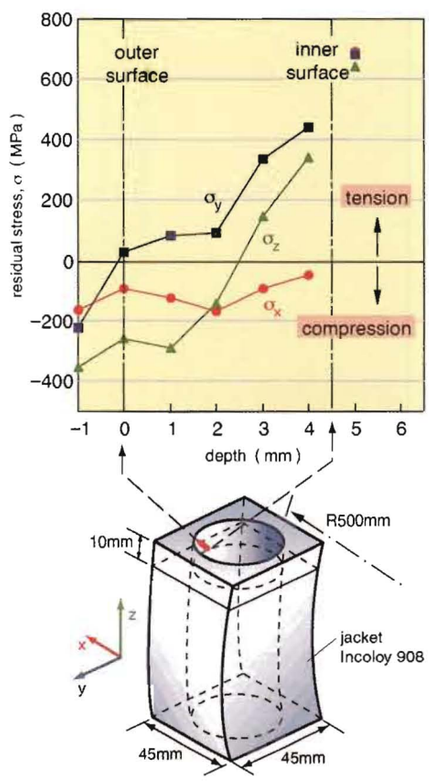

Fig. 11. Evaluated residual stress σx, σx, σx in a jacket material of the central solenoid superconducting coil. Horizontal axis represents depth from the outer surface of the jacket. Directions x, y, z are shown by the arrows in the lower figure.

International collaboration

Under the Japan-US collaboration, the upgrade of the WAND (Wide-Angle Neutron Diffractometer) is now going on. The main part of this project is the development of a new one-dimensional curved ^3He detector that covers 130 degree of the scattering angle. This detector will be a multi-anode counter (624 anodes on a 0.2 degree pitch), and the data acquisition will be done by a newly developed microprocessor controlled system. As a result, this detector will achieve in high counting rate (2 x 10^5 cps/pixel and 10^7 cps in overall) with high resolution and good uniformity. A prototype of this detector fabricated last year met the required performance. The upgrade will be completed in this calendar year. (Refer to "Progress report on JAERI-ORNL cooperative neutron scattering research".) For a new accessory a cryomagnet (1.5 K, 5 T) has been made. Its performance is satisfactory. Figure 12 shows the present WAND with this new cryomagnet.

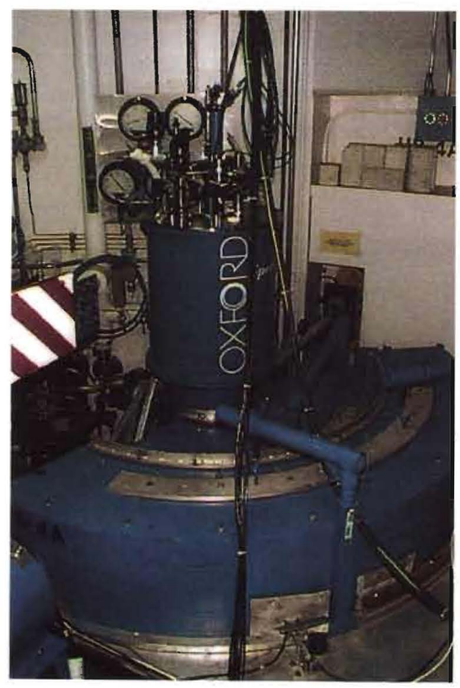

Fig. 12. WAND with a new cryomagnet.

The cooperative research program with BATAN, National Atomic Energy Agency of Indonesia, was also carried out. Two researchers stayed at JAERI for a few months to study diffuse scattering from super ionic conductor Ag_3SI and to develop operation softwares. Five Japanese researchers made short visits to BATAN to discuss various studies at the Indonesian research reactor RSG-GAS..

2. RESEARCH REPORTS

2.1 CRYSTAL STRUCTURES AND EXCITATIONS

2.1.1 A Powder Neutron Diffraction Study of $(ND_4)_3D(SO_4)_2$

I. Tamura, Y. Noda and Y. Morii[1]

Department of Physics, Faculty of Science, Chiba University, Yayoi, Inage, Chiba 263
[1]Research Group for Neutron Scattering at Ultralow Temperatures, Advanced Science Research Center, JAERI, Tokai, Ibaraki 319-11

$(ND_4)_3D(SO_4)_2$ (abbreviated as d-A_3HS) undergoes a ferroelectric phase transition at T_c(III'-VII)=182K while $(NH_4)_3H(SO_4)_2$ undergoes a ferroelectric phase transition at T_c(V-VII)=84K[1)] associated with the transformation from a monoclinic phase (paraelectric phase) to a triclinic phase (ferroelectric phase) with decreasing temperature. The complex domains were caused by this transformation, so that it is very difficult to perform the structure analysis using a single crystal. In order to study the origin of the ferroelectricity and a large isotope effect, structure analyses were performed on d-A_3HS by powder neutron diffraction at 293K and 10K.

Neutron powder diffraction intensities of d-A_3HS were measured by using HRPD constructed in JRR-3M and analyzed by the Rietveld method using the program RIETAN94. Fig. 1 shows diffraction patterns obtained in d-A_3HS at 293K and 10K. The space group of d-A_3HS had been determined to be A2/a at room temperature[2)]. However, the space group of d-A_3HS was newly determined as A2 at room temperature in our neutron scattering experiment. The reliability factor R_{wp}, R_p, R_I, R_F at 293K with the space group A2 were 3.91%, 3.02%, 6.19%, 4.84%, respectively while at 10K they were 5.38%, 4.14%, 10.48%, 6.94%, respectively with the space group A1. The structural difference between A2 and A2/a was mainly seen in the distortion of NH_4 molecules. The precise structure analysis at 10K is not completed and underway.

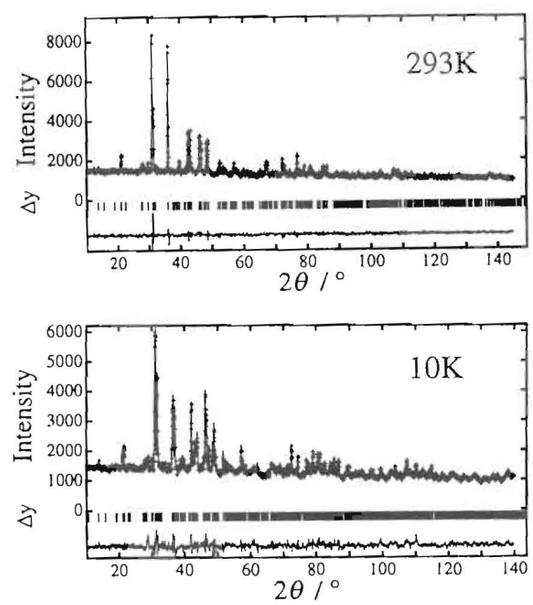

Fig.1 Powder diffraction pattern of d-A_3HS at 293K and 10K. λ=1.8232.

Reference

1) T. Osaka et al: J. Phys. Soc. Japan **43**(1977)933.
2) M. Tanaka and Y. Shiozaki: Acta Cryst. **B37**(1981)1171.

2.1.2 Neutron Diffraction Study of Proton-conducting Oxides

T. Nagasaki, N. Noda, Y. Ishii[1], T. Matsui and Y. Morii[1]

Graduate School of Engineering, Nagoya University, Nagoya 464-01
[1] Japan Atomic energy Research Institute, Tokai, Ibaraki 319-11

Such perovskite-type oxides as $SrCeO_3$ and $BaCeO_3$ doped with, e.g., Yb_2O_3 show protonic conductivity in hydrogen or water vapor atmosphere. Although various properties of these materials have been extensively studied, hydrogen (proton) sites in them are still an open question. The purpose of the present study is to identify the hydrogen sites in them by using neutron powder diffraction and to thereby cast light on the conduction mechanism.

As a sample material, we have selected $SrCe_{0.95}Yb_{0.05}O_3$ because it has high protonic conductivity as well as high hydrogen solubility and because it undergoes no phase transition between room temperature and the temperature at which it exhibits high protonic conductivity. However, its crystal structure is not simple (space group Pnma[1]), possibly making the data analysis difficult.

Powders of $SrCO_3$, CeO_2, and Yb_2O_3 were mixed and pressed into pellets, which were then sintered at 1770 K for 35 h in air and ground into powder again. To dissolve deuterium in it, we heated it at 873 K for 120 h in air saturated at room temperature with deuterium oxide vapor. (We refer to this process as D_2O treatment.) According to Uchida et al.,[2] a few mol% deuterium atoms dissolve in $SrCe_{0.95}Yb_{0.05}O_3$ under the above condition. For both samples with and without the D_2O treatment, we measured the diffraction patterns with HRPD.

We analyzed the diffraction data using a Rietveld analysis program RIETAN[3]. Table 1 shows the refined structure parameters of the sample without the D_2O treatment. The obtained values are in good agreement with the literature values[1] determined by XRD. It is noteworthy, however, that the present study gives much smaller uncertainties in the parameters for oxygen, which is a light element.

Table 1 Refined structure parameters of $SrCe_{0.95}Yb_{0.05}O_3$ without the D_2O treatment

		this work	Saiki (XRD) [1]
Space group		Pnma	Pnma
R_{wp}		9.38 %	10.97 %
R_e		3.95 %	—
a / nm		6.1455(1)	6.1409(2)
b / nm		8.5887(1)	8.5783(7)
c / nm		6.0050(1)	5.9997(4)
Sr	x	0.456(1)	0.455(1)
4(c)	y	0.25	0.25
	z	-0.012(1)	-0.013(1)
Ce, Yb	x	0	0
4(a)	y	0	0
	z	0	0
O(1)	x	0.042(1)	0.036(5)
4(c)	y	0.25	0.25
	z	0.105(1)	0.113(6)
O(2)	x	0.299(1)	0.300(4)
8(d)	y	-0.056(1)	-0.056(3)
	z	0.200(1)	0.206(4)

The diffraction pattern for the sample with D_2O treatment is hardly different from that for the sample without it. We have not yet deduced any significant structure parameters relating to the hydrogen sites. Further experiments seem necessary.

References

1) A. Saiki, Y. Seto, H. Seki, N. Ishizawa, M. Kato and N. Mizutani: Nihonkagakukaishi (1991) 24.
2) H. Uchida, H. Yoshikawa and H. Iwahara: Solid State Ionics **35** (1989) 229.
3) F. Izumi: "The Rietveld Method," ed. by R. A. Young, Oxford University Press, Oxford (1993), Chap. 13; Y.-I. Kim and F. Izumi: J. Ceram. Soc. Jpn. **102** (1994) 401.

2.1.3 Structure and Properties of Perovskite-related Transition-metal Oxides

Y. Inaguma, D. Iwanaga, M. Itoh, K. Aizawa[1], Y. Shimojo[1] and Y. Morii[1]

Materials and Structures Laboratory, Tokyo Institute of Technology, 4259 Nagatsuta, Midori-ku, Yokohama 226
[1]Japan Atomic Energy Research Institute, Tokai, Ibaraki 319-11

Transition-metal oxides with perovskite-related structure show various attractive properties. It is of great necessity to clarify the relation between the properties and the structure. Since in these compounds the structural information about oxygen has great importance, neutron diffraction is a supreme method for the structural analysis.

Among them, B-site ordered perovskites $A_2BB'O_6$, where B is the only paramaganetic ion present, become antiferromagnetic at low temperatures and that the most important exchange mechanism between the paramagnetic B ions over two anions and one diamagnetic cation is a superexchange interaction of the type BOB'OB (distance BB' is about 8 Å; angle 90° and 180°)[1]. Our attention is especially focused on the relation between the structure(including magnetic structure) and magnetic behavior of the Cu^{2+} ion containing ordered perovskites. They show a tetragonal distortion of the structure owing to the cooperative Jahn-Teller effect[2]. Furthermore, it is believed that these copper compounds are ferroelectrics. In this study, to investigate them the structural analysis by neutron diffraction method was carried out.

Neutron powder diffraction data for an ordered perovskite Ba_2CuWO_6 at 10 K and room temperature were collected on HRPD angle-dispersive type diffractometer at the JRR-3 reactor at JAERI. Neutron diffraction data were analyzed by Rietveld method with RIETAN[3].

Figure 1 shows the neutron powder diffraction pattern with Rietveld refinement at room temperature and 10 K. As shown in Fig.1, the structural phase transition could not be observed below room temperature. When the centro-symmetric space groups *I4/m* or *I4/mmm* was adopted, the least reliable factors can be obtained. This implies that this compound is not a ferroelectrics. The schematic arrangement of oxygen-octahedra in *ac*-plane was presented in Fig.2. As seen in Fig.2, the CuO_6 octahedron is elongated parallel to *c*-axis due to the Jahn-Teller effect, while WO_6 octahedron is compressed. This indicates the $d\gamma$ orbital of the Cu^{2+} ion is splited into $d_{x^2-y^2}$ and $d_{3z^2-r^2}$ orbitals, and the former is occpied by one electron, while the latter is fully occupied by a couple of electrons. Therefore it is expected that the anti-ferromagnetic superexchange interaction between Cu ions two-dimesionally occurs in the *ab*-plain and this compound shows two-dimensional anti-ferromagnetism. This is supported by the magnetic susceptibility data.

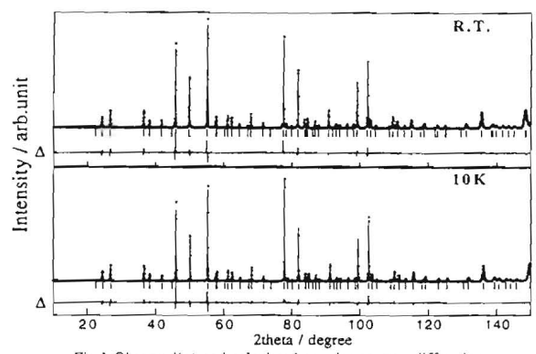

Fig.1 Observed(+) and calculated powder neutron diffraction intensities of $Ba_2(CuW)O_6$ at room temperature and 10K. Δ indicates the difference between both intensities.

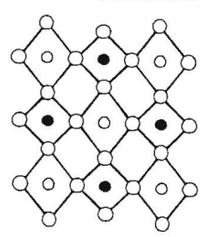

Fig.2 Schematic structure of $Ba_2(CuW)O_6$ at ac-plane.

References

1) G. Blasse, *Philips Res. Rep.*, **20**, (1965) 327-336.
2) G. Blasse, *J. Inorg. Nucl. Chem.*, **27**, (1965) 993-1003.
3) F. Izumi, "*The Rietveld Method* (R. A. Young, Ed.), Chap. 13, Oxford Univ. Press, Oxford(1993).

2.1.4 Diffuse Neutron Scattering From Ag_3SI at High and Low Temperatures

Aziz K. Jahja, Y. Ishii[2], N. Minakawa[2], Y. Hamaguchi[2], Y. Morii[2], T. Sakuma[3], Marsongkohadi[4]

Materials Science Research Centre, National Atomic Energy Agency
Kawasan Puspiptek Serpong, Tanggerang, Indonesia 15314
[2]Advanced Science Research Centre, Tokai Research Establishment, JAERI, Tokai-mura, Naka-gun,Ibaraki-ken,319-11
[3]Department of Physics, Faculty of Science, Ibaraki University, Mito 310
[4]Department of Physics, Faculty of Natural Sciences, Bandung Institute of Technology, Jln. Ganesha 10, Bandung 40132 Indonesia

Silver sulfur iodide has an antiperovskite structure, space-group O^1_h-Pm3m, with an ordered lattice of anions and a disordered arrangements of cations in the β-phase, and transforms at 246 °C to an α-AgI type solid electrolyte, space-group O^9_h-im3m with disordered arrangement of both cations and anions. At -116 °C it experiences a structural phase-transformation to an ordered γ-phase Space-Group C^4_3-R3 [1]. Ion disorder in α-AgI type superionic conductors has been associated with many physical properties of this type of materials, such as specific heat anomaly [1,2], frequency dispersion of the dielectric constant at low temperatures[1] and at high temperatures[2], as well as the appearance of a comparatively strong diffuse background in the measured x-ray and neutron scattering intensity. In order to understand the nature of ion disorder and its relationship to the observed physical properties of these materials, it is necessary to study the oscillatory diffuse scattering. Recently, a detailed theoretical treatment of the thermal diffuse scattering including the effects of the correlation between the thermal displacements of the atoms has been applied to the analysis of the diffuse scattering for α-AgI by X-ray and neutron scattering [3,4] and to Ag_3SI at room temperature [5]. In this report we present the results of diffuse scattering measurements of Ag_3SI at 538 K (α-phase), 498K (high-temperature β-phase), 187 K (low-temperature β-phase) and 127 K (γ-phase) investigated by elastic diffuse neutron scattering method over the 2-Θ range 0f 5 - 100° (corresponds to Q range of 0.3 - 7.1 $Å^{-1}$) is presented. Structural refinement results using the RIETAN[6] program and parameters from previous analysis[1] will be presented. The theoretical analysis of the diffuse intensities using detailed theoretical treatment of ion-disorder[3] is still in progress, and the results will be reported elsewhere. The neutron intensity was collected using the TAS-2 instrument set in double-axis mode installed in the neutron guidehall of the JRR-3M research reactor at JAERI,Tokai. The refined parameters are presented in Table1. and the refined elastic neutron scattering intensity is presented in fig. 1. At 498 K, the [111] peak intensity, becomes somewhat weaker than the room temperature result from previous report[1], therefore it is assumed that at 498 K, well below the β→α transition temperature 519 K, anisotropic and anharmonic thermal vibration must have played a larger role than at room temperature. Around the major peaks [110],[111],[200],[210] diffuse background was very prominent indicating disorder of the Ag^+ cation sublattice.At 265 °C (α-phase), the specimen underwent an

additional disordering, now that the S^- and I anion sublattice also become disordered, as indicated by the disappearance of the [111] peak, the Debye lines decrease in intensity and the diffuse background becomes more intense. RIETAN analysis shows that only the [200] peak was strong enough to be observable.

Tabel 1. Refined structural parameters of Ag_3SI

Parameter	128 K (γ)	186K (β)	498K (β)
a/Å	4.8459±0.0037	4.8882±0.0029	4.8807±0.0216
α	89.887±0.0614		
x_{Ag}/Å	0.5169±0.0099	0.3904±0.0075	0.3929±0.0194
y_{Ag}	0.3749±0.0058		
z_{Ag}	-0.0198±0.0140		
x_S	0.4394±0.01184		
B_{ag}/Å^{-2}	4.4398±1.2386	3.3798±2.9927	2.5682±7.2129
B_S	2.9045±2.0503	1.9321±2.6857	2.3207±7.9980
B_I	0.8897±0.7632	2.3752±2.9569	0.2334±6.1459
R_{wp}	13.89%	9.92%	13.25%
R_p	10.53%	7.63%	10.31%
R_F	3.18%	4.62%	7.01%

At -86 °C, the measurement result reveals the [111] peak as the most intense, and comparison of the Debye lines intensity indicate a more consistent result with previous measurements [1]. At -116 °C, Ag_3SI underwent a structural phase transition, and the Ag-,S- and I ions become ordered. This is indicated by a drastic decrease of the diffuse background, at low as well as high angles, and considerable increase in the intensity of previously weak [100],[110],[210] peaks etc. The most essential fact of the above RIETAN refinement results, is that these results confirm the the various phases of Ag_3SI as indicated by the reliable factors, and the refined structural parameters provide good starting points for the theoretical and detailed analysis of ion disorder now in progress.

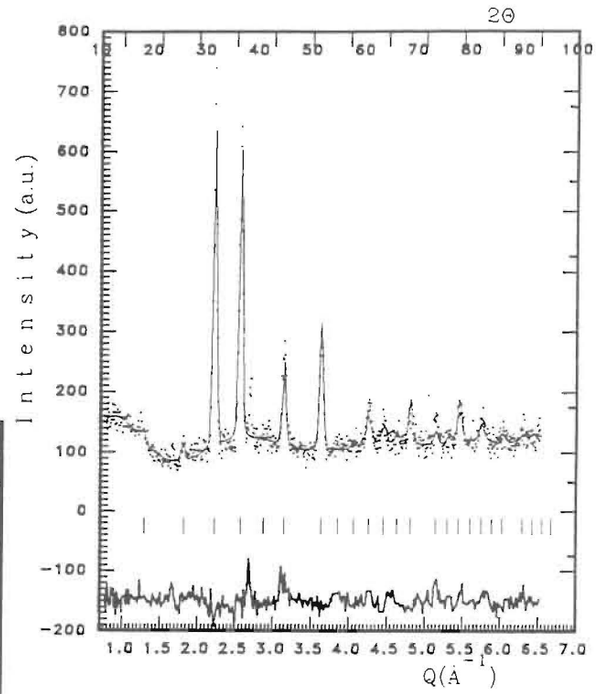

Fig. 1. Typical neutron scattering pattern of Ag_3SI measured at -86 °C and result of RIETAN refinement. Solid circles and solid line show the measured and calculated intensity, respectively.

References

1) S. Hoshino, T. Sakuma and Y. Fujii, J.Phys.Jpn. **47**(4), 1252 (1979)

2) A.K. Jahja, Marsongkohadi and W. Loeksmanto, Proceedings XVIth National Symposium on Physics and ASEANIP Regional Seminar on the Physics of Metals and Alloys, Bandung Dec 12-14, 1996, 178

3) T. Sakuma, J. Phys. Soc. Jpn. **62**, 4150 (1993)

4) T. Sakuma, J. Phys. Soc. Jpn. **61**, 4041 (1992)

5) T. Sakuma, F. Suzuki and S. Hoshino, Solid State Ionics **72**, 94 (1994)

6) RIETAN-94 by F. Izumi, in the Rietveld Method, edited by RA Young (Oxford University Press, Oxford, 1993)

2.1.5 Phonons of RbCl under High Pressure

A.Onodera, A.Mori, Y.Ishii[1], Y.Morii[1] and S.Kawano[2]

School of Engineering Science, Osaka University, Toyonaka, Osaka 560
[1]Japan Atomic Energy Research Institute, Tokai, Ibaraki 319-11
[2]Research Reactor Institute, Kyoto University, Kumatori, Osaka 590-04

One of the most dramatic phenomena that an application of pressure to solids can cause is the pressure-induced structural phase transition. This is exemplified by alkali halides which undergo the NaCl-type (B1) to the CsCl-type (B2) transition. Despite the extensive studies done for the phase diagrams, relatively little work has been undertaken on the mechanism of this transition.

The mechanism of the pressure-induced B1-B2 transition in alkali halides has been primarily discussed on the basis of the observations of crystallographic orientation relationships probed by x-ray diffraction[1-3] and neutron scattering[4,5]. In these cases, the mechanism put forth remains only provisional without knowing the dynamical behavior of the crystal under study. Any direct observation of the lattice dynamics is required for more deep understanding of the mechanism of the transition.

In this work, we have carried out neutron scattering measurement of RbCl in order to study the phonon dispersion of this material prior to the pressure-induced phase transition. RbCl is known to undergo the B1-B2 transition at about 5 kbar at room temperature[5]. We have developed a high-pressure cell which is accessble to this pressure and, at the same time, can accommodate a sample whose size is comparable to that of ambient-pressure studies.

The cell, shown in Fig. 1, is basically a piston-cylinder type. The cylinder is made of a Ti alloy and the pistons are of sintered alumina. The sample to be studied is placed inside a capsule made of Teflon along with the a pressure-transmitting medium, Fluorinert in our case. A cylindrical single crystal of RbCl, 20 mm long and 10 mm in diameter was studied. The crystallographic [001] axis was oriented parallel to the cylindrical axis of the crystal and, hence, to the axis of the Ti-alloy cylinder. This geometry permits the phonon measurements along the [001] and [110] directions. The cell was tilted for the measurement along the [111] direction.

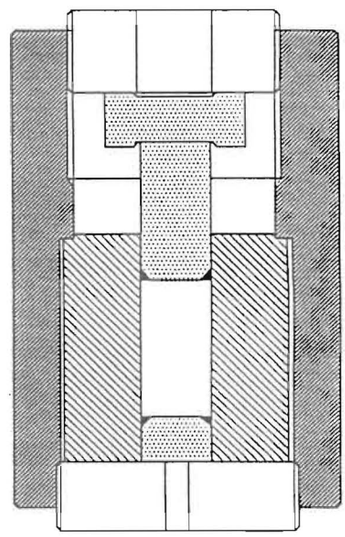

Fig.1 Cross-sectional view of the high-pressure cell.

High pressure on the B1 phase of RbCl was applied stepwise by measuring the (220) Bragg reflection. The volume derived from this reflection provided an estimation of the pressure. After the pressure was reached at 4.6 kbar which was close to the transition pressure, we locked the pressure. The cell was then mounted on TAS-1 of JRR-3. All the measurements were performed at room temperature.

Figure 2 shows the phonon dispersion relations of RbCl at ambient and high pressures. Also shown in Fig.2 are data of Raunio and Rolandson[6] who measured the phonons at 80 K at ambient pressure. At ambient pressure, there is essentially no change in the profiles of the dis-

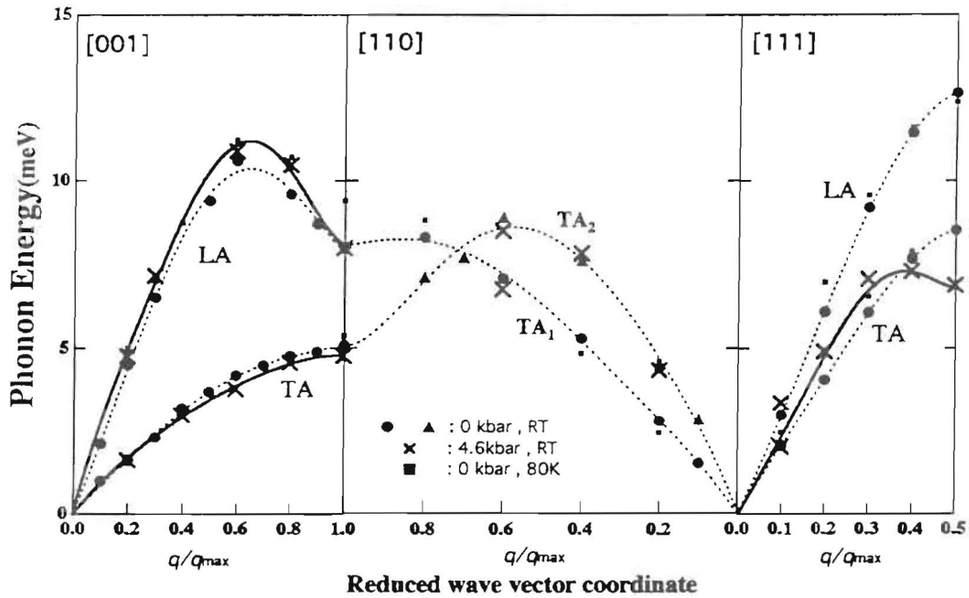

Fig.2 Phonon dispersion relations of RbCl at ambient and high pressures.

persion relations between 80 K and room temperature. A slight lowering of energies with elevation of temperature from 80 K to room temperature is seen in the LA mode along the [001] and [111] directions and in the TA mode along the [111] direction. The effect of pressure on the phonon dispersion relation at room temperature is much more complicated. Along the [001] direction, the energies of LA mode increase whereas those of TA mode decrease. The most prominent effect of pressure occurs at the zone boundary of TA mode along the [111] direction. The energy at this points is lowered by about 15% from the ambient-pressure value.

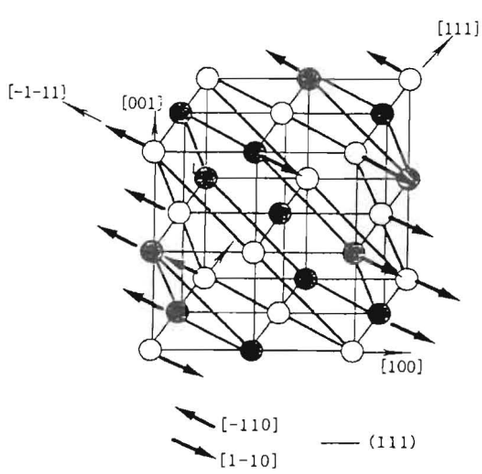

Fig.3 Proposed mechanism of the B1-B2 transition in RbCl.

This observation, together with our previous measurement on the orientaiton relationships[5], allow us to derive the mechanism of the B1-B2 transition as shown in Fig.3. It is likely that the (111) planes of B1 phase exhibit sliding relative to each other with a shear wave propagating along the [111] direction.

References

1) B.Okai: J.Phys.Soc.Jpn. **48** (1980) 514.
2) B.Okai: J.Phys.Soc.Jpn. **50** (1981) 3189.
3) H.Fujiwara, N.Nakagiri and M.Nomura: J. Phys.Soc.Jpn. **52** (1983) 1665.
4) O.Blaschko, G.Ernst, G.Quittner, G.Pepy and M.Roth: Phys.Rev. B**20** (1979) 1157 .
5) A.Onodera, Y.Nakai, S.Kawano and N.Achiwa:High Temp.High Press. **24** (1992) 55.
6) G.Raunio and S.Rolandson: J.Phys. C**3** (1970) 1013.

2.1.6 Phonon measurement of RbCl under High Pressure

Y.Ishii, A.Mori[a], A.Onodera[a], S.Kawano[b] Y.Morii

Japan Atomic Energy Research Institute, Tokai, Ibaraki 319-11 Japan
[a]Faculty of Engineering Science, Osaka University, Osaka 560 Japan
[b]Research Reactor Institute, Kyoto University, Kumatori, Osaka 590-04 Japan

Alkali halides which have the NaCl-type crystal structure(B1) at ambient condition transform to the CsCl-type crystal structure(B2) under high pressure. This phase transition has been discussed in terms of both reconstructive and displacive transition mechanisms. The reconstructive mechanism based on nucleation and crystal growth processes has been proposed for the phase transition of KCl[1]. On the other hand, for displacive one the transition mechanisms seem to be complex, depending on the results of many experiments using single crystals[2-4]. However, these studies have been mainly focused on the phase transition paths between B1 and B2 crystal structures. For further understanding of the mechanism of the B1-B2 phase transition, lattice dynamical studies at just below the transition pressure are very important. In this paper, some results regarding the phonon energy of RbCl at 4.9 kbar which is 0.3 kbar below the phase transition pressure are reported.

To get high-quality data, we have developed a pressure cell that can accommodate a large single crystal of 10 mm in diameter and 20 mm in length. Experiments were conducted with a triple-axis spectrometer, TAS-1, installed at JRR-3M in JAERI. Phonon energy measurements were carried out with an energy loss and a constant-q method. Used neutron energies were 14.8 meV and 30 meV. A pyrolytic graphite filter was used to eliminate $\lambda/2$ contamination. All measurements were carried out at room temperature.

The phonon energies of RbCl were measured at ambient pressure and at 4.9 kbar(see Fig.2. p15 in this book). From this figure, one can see that the phonon energies measured at ambient pressure at room temperature are almost same as those at 80K except for the LA-mode along [001] direction. At the zone boundary (X-point) the energy difference is prominent. This difference can be related to an anharmonicity of the thermal vibration of ions, because Debye temperature of RbCl is about 168 K[5].

The pressure effect on the phonon dispersion relations at room temperature is much interesting. Phonon energies of the [001]LA mode at 4.9 kbar are large compared to those at ambient pressure at all wave numbers except at the zone boundary. On the other hand, the energy of the [001]TA mode slightly decreased. The most prominent effect of pressure was observed for the [111]TA mode. The phonon energy of this mode increases with increasing the wave vector and exhibits a maximum value at q/q_{max}= 0.35. Then the energy decreases toward the zone boundary. At the zone boundary (L-point) this energy becomes about 85% of that at ambient pressure. Sanderson[6] reported a similar pressure effect; the energy of the TA-mode at the X-point of RbI was decreased with pressure and the phonon energy at just below its transition pressure became to be 87%.

The pressure-induced B1-B2 transition is the first order phase transition between the phases which have high crystal symmetries. Then any softening of the phonon energies is not expected to the acoustic branches. However, a decrease in the phonon energy of RbCl was observed at just below its transition pressure in the [111]TA mode at the zone boundary. This pre-transition phenomena should be closely related to an anharmonicity of the thermal vibration of the atoms of RbCl under high pressure, because the third order asymmetric anharmonitic term of potential causes the asymmetric thermal vibrations along the [111] direction in the cubic crystals. Therefore, the energy decrease observed in this experiment should be related to the third order anharmonicity and this anharmonic thermal vibration under high pressure can be the origin for the B1-B2 transition of RbCl.

References

1. N.Hamaya and S.Akimoto, High Temp. High Press., **13**, 347 (1981)
2. M.Watanabe, M.Tokoname and N.Morimoto, Acta Crystallogr., **A33**, 294 (1977)
3. B.Okai, J. Phys. Soc.Jpn., **48**, 514 (1980)
4. A.Onodera, S.Kawano, Y.Nakai and N.Achiwa, Physica B, **180&181**, 279 (1992)
5. G.Raunio and S.Rolandson, J. Phys., **C3**, 1013 (1970)
6. D.K.Sanderson, Phys. Rev. Lett., **17**, 530 (1966)

2.1.7 Phonon anomaly of $Ti_{50}Ni_{30}Cu_{20}$

Y. Morii, X. Ren[1], K. Taniwaki[1], K. Otsuka[1]

Advanced Science Research Center, Japan Atomic Energy Research Institute, Tokai, Ibaraki 319-11
[1]Institute of Materials Science, University of Tsukuba, Tsukuba, Ibaraki 305

Ti-Ni alloy is well known for its reversible shape memory effect originating from martensitic phase transformation (MPT). Parent phase of equiatomic TiNi has cubic (B2) structure and transforms to monoclinic phase (B19', space group $P2_1/m$) via a premartensitic phase called R-phase. Associated with this MPT, many anomalous phenomena were observed. Among them it was reported by Tietze et al.[1)] that energy of the $[110]TA_1$ (e//[1-10]) phonon decreased to zero at $q_{110}=q_{max}/3$ associated with the premartensitic phase.

Alloy with twenty atomic percent substituting copper $Ti_{50}Ni_{30}Cu_{20}$ has narrow transformation hysteresis under load. Therefore the alloy is expected to be a quite good actuator material for electric over-current protectors and rice cookers for example. In the alloy MPT takes place from cubic (B2) to orthorhombic (B19) structure via no premartensite phase. The martensitic phase has so called 2H layered structure of (110) plane.

From our previous studies on noble metal based alloys[2)], it is expected in $Ti_{50}Ni_{30}Cu_{20}$ that (1) $[110]TA_1$ phonon energy tends to decrease at the zone boundary, (2) force constants of (110) plane show a typical combination characteristics for 2H martensite. Therefore we started to measure $[110]TA_1$ phonon dispersion relations at the temperatures above MPT of this alloy to understand expected anomalies from microscopic point of view.

A triple axis spectrometer TAS-2 installed at JRR-3M was used. The incident neutron energy of 14.7 meV (wavelength of 2.35 A) was used with a PG filter to reduce higher order wavelength contamination. The collimation of TAS-2 was 17'-40'-40'-40'.

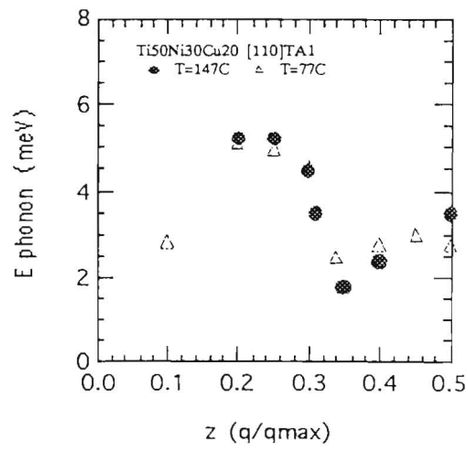

Figure shows preliminary results on $[110]TA_1$ phonon at 420 K (100 K above MPT) and 350 K (30 K above MPT). It is clearly shown that (1) There is a big 'dip' in the phonon dispersion curve at $q_{110}=q_{max}/3$ similar to that observed in the equiatomic TiNi, (2) The 'dip' seems to get smaller at the lower temperature or the closer point to MPT, (3) Phonon energy at the zone boundary decreased at the closer temperature to MPT.

Further experimental evidences should be obtained to see (1) whether a complete softening takes place at $q_{110}=q_{max}/3$, (2) whether a further decrease in the phonon energy at the zone boundary is observed at the temperatures near MPT.

References

1) H.Tietze, M.Mullner, B.Renker; J. Phys. C: Solid State phys., **17** (1984) L529-L532
2) A.Nagasawa, Y.Morii; Materials Trans. JIM, **10** (1993) 855-873

2.1.8 Neutron powder diffraction study of Chalcopyrite, $CuFeS_2$

K.Sugimoto, T.Kobayashi, K.Ishida, S.Kumazawa[1], Y.Ishii[1] and Y.Morii[1]

Depertment of Phisics, Science University of Tokyo, Noda, Chiba 278
[1]Japan Atomic Energy Research Institute, Tokai, Ibaragi 319–11

Chalcopyrite-type compounds are semiconductors and known as useful materials for solar batteries, nonlinear optical devices and luminescence diodes. The purpose of the present work is to study the relation between the physical property and the structural feature of chalcopyrite, $CuFeS_2$. The chalcopyrite is a tetragonal structure, the space group of No.122. The sites of Cu, Fe and S are reported as $4a$, $4b$ and $8d$, respectively. From Rietvelt refinement of X-ray powder diffraction patterns, we obtained that a=5.28813(19)Å, c=10.42004(44)Å and x=0.2540(15). From X-ray measurements, however, the further refinement of the structure is difficult, since atomic numbers of Cu and Fe are close each other. Therefore, we performed neutron powder diffraction measurements of chalcopyrite with the high resolution neutron powder diffractometer (HRPD) at JRR-3M. The chalcopyrite is antiferromagnetic at room temperature, with the moments aligned parallel to the c-axis[1]. Therefore, the neutron diffraction pattern is formed by magnetic scattering as well as nuclear one. However, we have not a Rietvelt code which is applied for a powder diffraction pattern from a magnetic material. So that we make a new Rietvelt code which is an extended code of the PFLS[2] for including magnetic scattering.

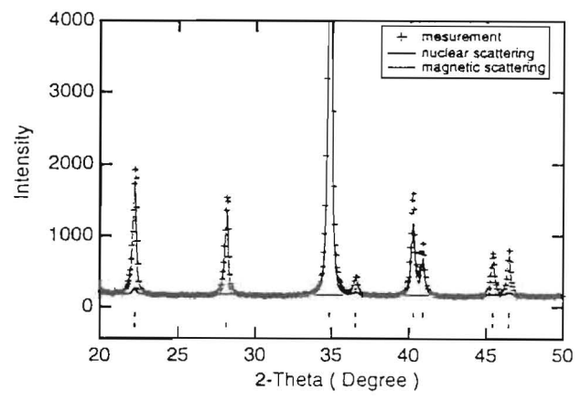

Fig.1 Nuclear, magnetic calculations (bold and fine lines) and measurements (+) of chalcopyrite

In Fig.1 shows an example of an experimental and calculated result. The agreement between the experiment and calculation is fairly good. Further investigations are now in progress.

References

1) G.Donnay, L.M.Corliss, J.D.H.Donnay, N.Elliot, and J.M.Hastings: Phys.Rev.112, (1958) 1917–1923

2) H.Toraya and F.Marumo: Report of the Research Laboratory of Engineering Materials, Tokyo Institute of Technology, 5, (1980) 55–64

2.1.9 Structure of Lithium Titanogallate Prepared by Ion Exchange Reaction

Y. Michiue, M. Watanabe, F. Izumi, Y. Morii[1] and Y. Shimojo

National Institute for Research in Inorganic Materials, Namiki 1-1, Tsukuba, Ibaraki, 305 Japan
[1]Japan Atomic Energy Research Institute, Tokai, Ibaraki, 319-11 Japan

We have been studying ion exchange reaction utilizing one-dimensional tunnel-like pathways in crystal structures. Only a little studies for such a reaction has been reported so far, because the one-dimensional pathway is unfavorable for ion transport. Application of ion exchange technique for one-dimensional pathways will, however, enlarge the possibility of obtaining new materials.

In the present study, neutron diffraction measurement for lithium titanogallate, $Li_{0.85}Ti_{1.15}Ga_{4.85}O_{10}$, has been performed. This compound has never been obtained by the conventional calcination methods but by heating a polycrystalline sample of the parent Na-salt, $Na_{0.85}Ti_{1.15}Ga_{4.85}O_{10}$[1], at *ca.*450 °C in molten $LiNO_3$.

The Rietveld analysis by using *RIETAN* (R_{wp}=8.30, R_p=6.14, R_I=3.70, R_F=2.02%, S (=R_{wp}/R_e) =1.53) has confirmed that the framework structure (Fig. 1) is retained after the ion exchange reaction. Two Ga positions, *Ga1* and *Ga2*, are tetrahedral and octahedral coordination site, respectively. Another octahedral coordination site *M* is occupied by Ga and Ti. The linkage of these coordination polyhedra makes up the framework structure containing one-dimensional tunnels along the *b*-axis. Cell parameters have been anisotropically changed according to exchange of Li for Na; differences are -2.0, +0.5 and -0.4 % for *a*, *b* and *c*-axis, respectively. Considerable decrease in the *a*-axis is understandable by seeing the geometry of the tunnel. Li ions are located at two positions which were found from difference Fourier maps. One is close to the tunnel center, while the other is much deviated from it as shown in Fig. 1. This is characteristically different from the distribution of Na ions in the parent compound[1].

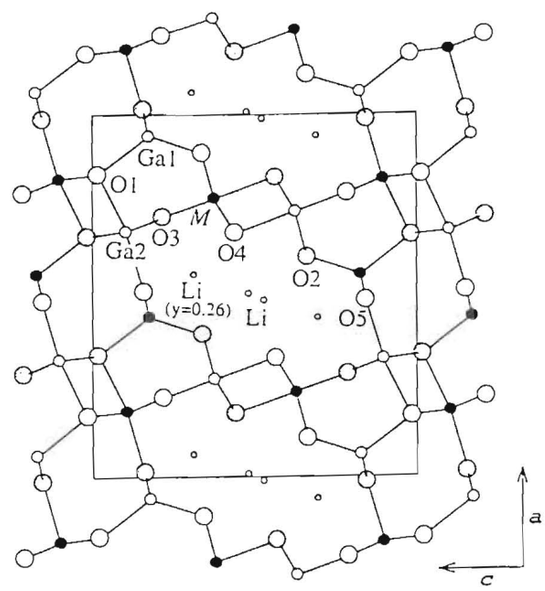

Fig. 1 Framework structure of $Li_{0.85}Ti_{1.15}Ga_{4.85}O_{10}$ projected along the *b*-axis. *C2/m*, *a*=11.860, *b*=3.026, *c*=10.374 Å, *β*=90.10°. Atoms represented by open and filled circles are at y=0 and 0.5, respectively.

Reference

1) Y. Michiue and M. Watanabe, *Solid State Ionics* **70/71** (1994) 186.

2.2 MAGNETIC STRUCTURES AND EXCITATIONS

2.2.1 Magnetic Structure of $DyCu_2$

Y. Koike[1], N. Metoki[1], Y. Morii[1], Y. Yoshida[2], R. Settai[2] and Y. Ōnuki[1,2]

[1] *Advanced Science Research Center, JAERI, Tokai, Ibaraki 319-11*

[2] *Graduate School of Science, Osaka University, Toyonaka, Osaka 560*

Rare earth intermetallic compounds RCu_2 with the orthorhombic $CeCu_2$ type structure have been widely investigated. This system exhibits successive magnetic transitions and complicated magnetic structures at low temperatures [1-2]. The origin is considered to be a competing effect of RKKY interaction with crystalline anisotropy.

$DyCu_2$ is one of the compound of this series. A recent neutron scattering study reported the antiferromagnetic structure with the modulation vector [1/3 0 0] below 15 K. The thermal expansion data[3] showed sharp peaks at T = 19.5 K and 31.5 K. The peak at 31.5 K attributes to the magnetic ordering, while the one at 19.5 K has not been understood yet. The purpose of this study is to reveal the magnetic phase diagram and structure of $DyCu_2$.

Neutron scattering experiments were carried out using a triple-axis spectrometer TAS-1 installed at JRR-3M. The incident beam (E_i = 30.5 meV) is monochromatized by a vertically bent PG(0 0 2) monochromator. Higher harmonics were removed by a PG filter. The collimation was 40'-40'-40'-40'. A single crystal sample (3$^{\phi}$ x 20 mm) cooled in a displex type cryostat with (h 0 l) plane parallel to the scattering plane. The full width of the (2 0 0) rocking curve was about 0.3°.

We observed two magnetic phases. The low temperature phase (below 19.5 K) is characterized by two types of magnetic reflections; (i) (h±1/3 0 l) with $h+l = 2n$, and (ii) (h 0 l) with $h+l = 2n+1$, where n is an integer (Fig. 1). These two types of reflections involve that there are two different antiferromagnetic modulations with Q=[1/3 0 0] and [001] for (i) and (ii), respectively. This phase would correspond to the magnetic structure as reported before [1].

For 19.5 K < T < 31 K another magnetic phase is stable. We observed strong magnetic reflections at (i') (h±[1/3+δ] 0 l) with $h+l = 2n$. It should be noted that this magnetic phase has an incommensurate structure with δ=0.012. This phase is found for the first time in this study.

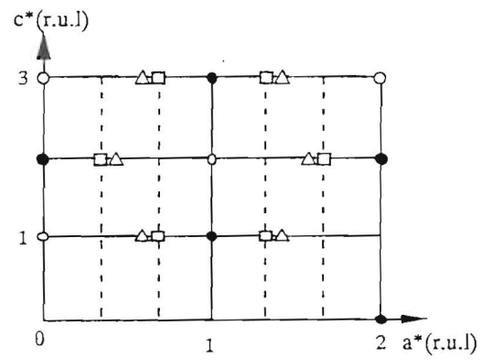

Fig. 1 Observed Bragg reflections of $DyCu_2$. Open squares and circles denote the magnetic reflections (i) and (ii), respectively (T < 19.5 K). Open triangles indicate magnetic reflections (i') (19.5 K < T < 31.5 K). Close circles are nuclear peaks.

Figure 2 is the temperature dependence of the (-1/3 0 2) and (-1/3-δ 0 2) magnetic peak profile. For T<19.5 K we observed a commensurate peak at (-1/3 0 2). The peak intensity decreases continuously with increasing the sample temperature. No systematic temperature dependence of the peak position and the line width has been observed. At T=19.5 K, however, the (-1/3 0 2) peak disappears and switches to (-1/3-δ 0 2) in a very narrow temperature range. This peak shows a small change of the peak position and the line width.

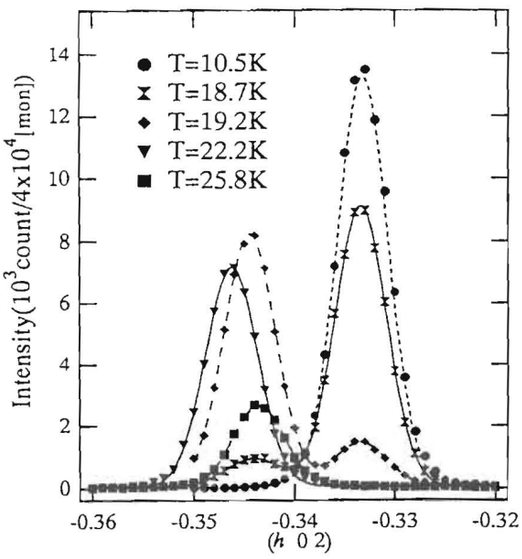

Fig.2. Temperature dependence of the neutron scattering profile of (-1/3 0 2) msgnetic Bragg peak.

However we observed no continuous shift of the peak position from δ=0 to 0.012, indicating the first order transition between these two phases. The (2 0 0) and (0 0 2) nuclear Bragg peak showed no change at this transition both in longitudinal and transverse directions. Therefore we conclude that the small shift δ is due to an incommensurate magnetic structure. The magnetic modulation length L=360 Å was estimated from the incommensurability δ of this peak ($L=a/\delta$)

Figure 3 shows the temperature dependence of the (-1/3-δ 0 2), (-1/3 0 2) and (0 0 3) magnetic peak intensities. The (-1/3-δ 0 2) peak intensity increases continuously below the Néel temperature T_N=31.5 K. At T=19.5 K the (-1/3-δ 0 2) peak vanishes very rapidly. Instead, (-1/3 0 2) peak appears and increases in intensity. The intensity of the (-1/3 0 2) peak connects to the one of (-1/3-δ 0 2) smoothly and these peaks behave as a magnetic order parameter. In addition to the abrupt change of (-1/3 0 2) peak, the magnetic reflections (ii) start to grow below 19.5 K. The (0 0 3) peak intensity increases continuously with decreasing temperature. It means that the antiferromagnetic modulation with the modulation vector [001] is the second component of the order parameter of the low temperature phase.

In conclusion, the magnetic structure of $DyCu_2$ has been studied by means of neutron scattering. We observed successive magnetic transitions at T=19.5 K and 31.5 K. The high temperature phase has an incommensurate magnetic structure. As the next step we are going to determine the spin structure.

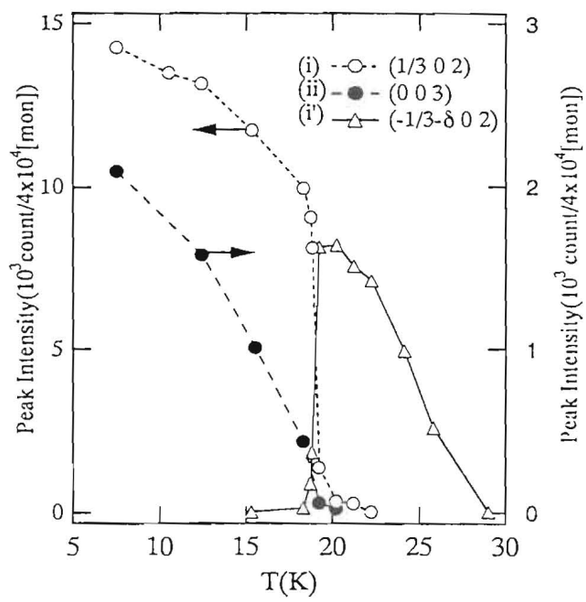

Fig.3. Temperature dependence of the peak intensity of (-1/3 0 2), (0 0 3) reflections.

References

1) B. Lebech, Z. Smetana, and V. Sima: J. Magn. Magn. Mater. **70** (1987) 97.
2) Y. Hashimoto, H. Fujii, H. Fujiwara, and T. Okamoto: J. Phys. Soc. Jan. **47** (1979) 67.
3) N.H. Luong, J.J.M, Franse, and T.D. Hien: J. Magn. Magn. Mat. **50** (1985) 153.

2.2.2 Neutron Diffraction of HelimagneticY(Tb)Mn_2

M. Shiga, H. Nakamura and N. Metoki [1]

Department of Materials Science and Engineering, Kyoto University, Kyoto 606-01
[1] Japan Atomic Energy Research Institute, Tokai, Ibaraki 319-11

A Laves phase compound YMn_2 is a well-known helimagnet with an extremely long period of 400 Å along the [100] direction. We have found that the direction of the helix propagation vector changed to [110] form [100] of YMn_2 by substituting only 3 % Tb for Y [1]. Low-energy neutron diffraction measurements using a long wave length (4.750 Å) beam enabled to obtain this result. The origin of the long-period helimagnetism of YMn_2 and of the dramatic change of the modulation vector by the small substitution remains to be explained, but seems to be related to the small tetragonal distortion appeared below the Néel temperature. On the other hand, Bertier et al. [2] reported that the Tb-8% substituted sample loses the modulation and becomes a simple collinear antiferromagnet. It is of interest to investigate the evolution of the helix in the concentration range of $x \leq 0.08$ for $Y_{1-x}Tb_xMn_2$. As the first trial we prepared an polycrystalline sample of $Y_{0.92}Tb_{0.08}Mn_2$ and measured neutron diffraction at 10 K and room temperature using the high-resolution powder diffractometer (HRPD) installed at JRR-3M reactor at JAERI. The wave length is 1.8230 Å.

Figures 1 (a) and (b) are the principal magnetic Bragg peaks of the Tb-8% sample obtained at 10 K. Contrary to the previous report (ref. 2), the structures similar to those observed for Tb-3% were obtained; triplet structure for $(110)_M$ and doublet for $(201)_M$. This result indicates that the Tb-8% sample also exhibits helical modulation along [110]. From the separation of the peaks, the modulation period was estimated as about 430 Å, which is longer than that of YMn_2 (~ 400 Å) but somewhat shorter than the Tb-3% sample (530 Å). We also observed the splittings of some nuclear Bragg peaks, which indicates the tetragonal distortion. From the separation of $(400)_N$, the distortion was estimated to be $1 - a/c = 0.51$ %. Although disappearance of the helical modulation by the substitution of small amount of third elements has been reported for several pseudo-binary systems, our result suggests that it is necessary to reexamine multiplet structures of the magnetic peaks by using long wave-length neutron beam.

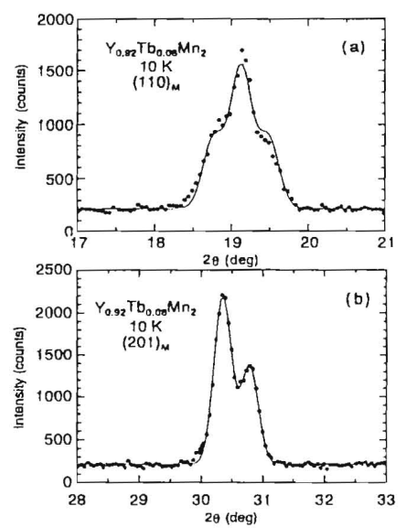

Fig. 1 Magnetic Bragg peaks of $Y_{0.92}Tb_{0.08}Mn_2$ obtained at 10 K.

References

1) H. Nakamura, M. Shiga and N. Metoki, J. Magn. Magn. Mater. **163** (1996) L1.
2) Y. Berthier, J. Deportes, M. Horvatic and P. Rouault, J. Phys. (Paris) **49** C8 (1988) 261.

2.2.3 Neutron Scattering Study on $CuGe_{1-x}Si_xO_3$

O. Fujita, J. Akimitsu, S. Katano[2], M. Nishi[3]

Department of Physics, Aoyama-Gakuin University, Setagaya-ku Tokyo 157
[2]Advanced Science Research Center, Japan Atomic Energy Research Institute , Tokai 319-11
[3]Neutron Scattering Laboratory, ISSP, University of Tokyo, Tokai 319-11

The first inorganic spin-Peierls material $CuGeO_3$ dicovered by Hase *et al.* [1] has received much attention and extensive studies have been performed. Among them, the impurity effect was a most important subject because of the difficulty for the substitution of magnetic impurity in the organic spin-Peierls material.

The $CuGeO_3$ indicates the antiferromagnetism in the case that Cu and Ge ions are slightly replaced by Zn and Si ions, respectively. Regnault [2] *et al.* experimentally indicated for the first time the temperature dependence of neutron scattering intensity both for the superlattice and magnetic reflections in 0.7 % Si doped sample. Neutron scattering experiment was performed and the existence of the spin-Peierls gap was confirmed in Si doped material. These results suggest that the spin-Peierls phase coexists with the antiferromagnetism. Hase *et al.* [3] also deteced the coexistence in $Cu_{1-x}Zn_xGeO_3$. Fukuyama *et al.* [4] proposed the theoretical model which explains the coexistence of dimerization and antiferromagnetism. This model suggests that the latiice distortion along the chain direction changed spatially.

In order to obtain the phase diagram vs. Si concentration, we performed the neutron scattering experiment on $CuGe_{1-x}Si_xO_3$. We measured the intensities of antiferromagnetic reflection at (0, k, l/2) and superlattice reflection at (h/2, k, l/2) using the triple-axis spectrometer TAS-1 installed in JRR-3M at JAERI.

The typical peak profiles of (0, 0, 1) and (0, 1, 1/2) are shown in Fig. 1. The width of the magnetic reflection is almost the same as that of the nuclear

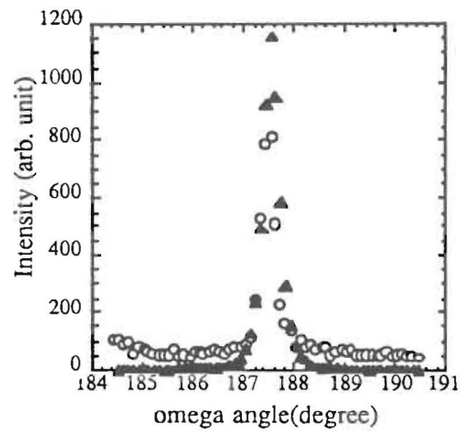

Fig. 1 Peak profile of (0, 1, 1) (solid triangle) and (0,1,1/2) (open circle).

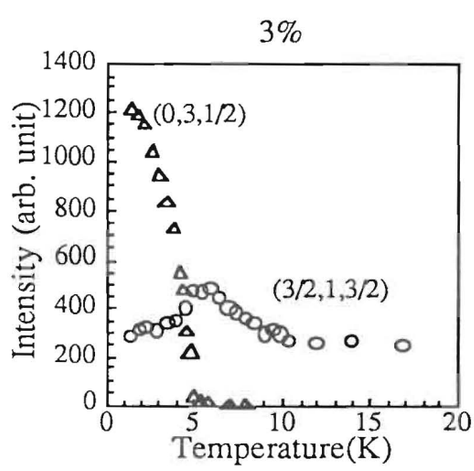

Fig. 2 Temperature dependence of both magnetic and superlattice reflection in 3% Si doped sample.

reflection, suggesting that the antiferromagnetism is of long range order. Figure 2 and 3 show the temperature dependence of superlattice reflection (3/2, 1, 3/2) and magntic reflection (0, 3, 1/2), respectively. These figures correspond to the sample with x=0.03 and x=0.005. The intensity of tsuperlattice reflection increases at the spin-Peierls transition temperature. In 3% Si sample, the intensity of superlattice reflection definitely decreases at the antiferromagnetic transition temperature. On the contrary, the intensity of magnetic reflection, however, is too small to be recognized in 0.5 % Si doped sample.

The phase diagram (transition temperature vs. Si concentration) is shown in fig. 4. This phase diagram is different from that obtained by Renard *et al.* [5] by using magnetization measurment. The spin-Peierls transition temperature decreases with increasing Si concentration and the decreasing rate of transition temperature against Si concentration in Renard *et al.*'s results is twice as large as that of our's.

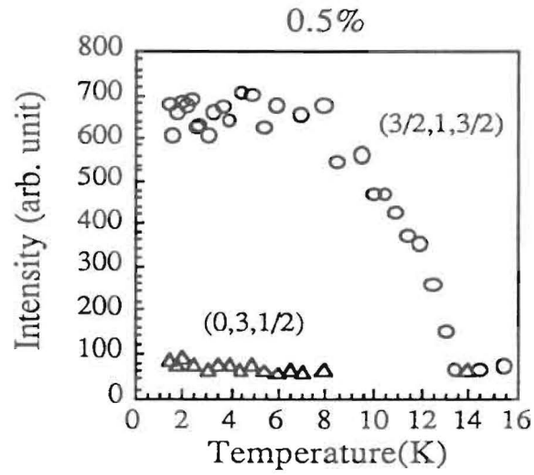

Fig. 3 Temperature dependence of both magnetic and superlattice reflection in 0.5% Si doped sample.

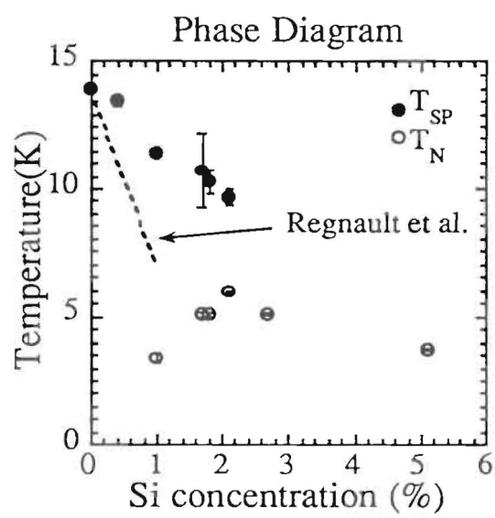

Fig. 4 Temperature vs. Si concentration phase diagram. The dotted line is the result of Regnalt et al.

References

[1] M. Hase, I. Terasaki, K. Uchinokura, Phys. Rev. Lett. 70 (1993) 4723.
[2] L. P. Regnault, J. P. Renard, G. Dhalenne, A. Revcolevschi, Europhys. Lett., 32 (1995) 579.
[3] M. Hase, K. Uchinokura, R. J. Birgeneau, K. Hirota, G. Shirane, J. Phys. Soc. Jpn., 65 (1996) 1392.
[4] H. Fukuyama, T. Tanimoto, M. Saito, J. Phys. Soc. Jpn., 65 (1996) 1182.
[5] J. P. Renard, K. Le Dang, P. Veillet, G. Dhalenne, A. Revcolevschi, L. P. Regnault, Europhys. Lett. 30 (1995) 475.

2.2.4 Neutron Diffraction Study on Potassium Uranate KUO_3

Yukio Hinatsu, Noriko Nitani[1], Yutaka Shimojo[1] and Yukio Morii[1]

Division of Chemistry, Graduate School of Science, Hokkaido University, Sapporo 060
[1]Japan Atomic Energy Research Institute, Tokai-mura, Ibaraki 319-11

Potassium uranate KUO_3 shows an antiferromagnetic-type of transition at ca 17 K in the magnetic susceptibility vs temperature curve. In this study, neutron diffraction analysis has been performed on the powdered KUO_3 below and above the transition temperature. The measurements have been performed with a High Resolution Powder Diffractometer (HRPD) in the JRR-3M reactor with a neutron incident wave length (λ = 1.823 Å). The powders of KUO_3 were filled into a cylinder of vanadium thin foil, about 6 mm in diameter and about 40 mm long.

Figure 1 shows the neutron diffraction patterns measured at 10 K and at 50 K. No appreciable differences have been found between them. No extra peak due to antiferromagnetic ordering of U^{5+} moment is observed at 10 K, i.e., no magnetic ordering was found by the neutron diffraction experiments, although the antiferromagnetic behavior is found in the magnetic susceptibility vs. temperature curve. For these experimental results, we consider that a small ordered magnetic moment of U^{5+} (which is expected from its too small effective magnetic moment of 0.66 μ_B) will make it very difficult to observe magnetic diffractions, even if a magnetic ordering occurs. If the magnetic spin alignment occurs in a small domain, no magnetic diffraction will be found in the neutron experiments.

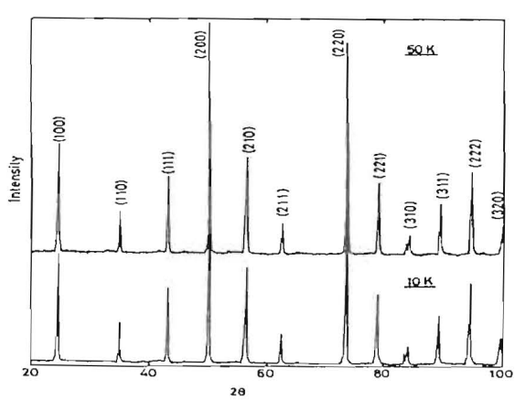

Fig. 1. Neutron powder diffraction patterns for KUO_3 measured at 10 K (lower) and 50 K (upper).

The profile of the powder neutron diffraction could be refined with the space group Pm-3m. Figure 2 shows the results: the calculated and observed diffraction patterns are shown on the top solid line and the dots, respectively. The reliability factor R defined as $R = \Sigma|I_{obs} - I_{cal}|/\Sigma I_{obs}$ was 0.063, where I_{obs} and I_{cal} are observed and calculated intensities, respectively. The obtained R factor is small enough for the present statistics of neutron counts.

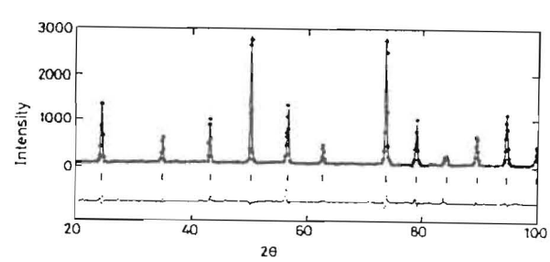

Fig. 2 Neutron powder pattern fitting for KUO_3 (10 K).

2.2.5 Magnetic Structure of Orthorhombic Phase in γ-MnT (T = Fe, Pd) Alloys

T. Hori, Y. Tsuchiya[1], Y. Shimojo[1], H. Shiraishi, S. Funahashi[1] and K. Hojou[1]
Shibaura Institute of Technology, Omiya, Saitama 330
[1]Japan Atomic Energy Research Institute, Tokai, Ibaraki 319-11

It is well known that many Mn-rich γ-Mn alloys undergo a distortion from the face-centered cubic (f.c.c.) phase to the face-entered tetragonal (f.c.t.) phase with c/a <1 below the Néel temperature. In γ-MnNi alloys, the f.c.t. phase with c/a >1 and the face centered orthorhombic (f.c.o.) phase are also observed [1]. Jo et al. [3] have proposed a theoretical phase diagram for the γ-Mn alloys on the basis of a Landau expansion of the free energy. They have also suggested some possible magnetic structure; the a-, b- and c-axis components of the magnetic moment, μ_a, μ_b and μ_c are related to the lattice as follows: $\mu_c^2 > \mu_b^2 > \mu_a^2$ in the f.c.o. phase with $a>b>c$, and $\mu_c^2 > \mu_b^2 = \mu_a^2$ in the f.c.t. phase with $c/a < 1$. Recently, we found that γ-MnGa alloys with 23 at % Ga distort to f.c.t. with $c/a < 1$ and to f.c.o. at a lower temperature, and determined the magnetic structures [4] as shown in Fig. 1. The results are consistent with the theoretical prediction by Jo et al.

We also found that there is the f.c.o. phase in γ-MnPd alloys and γ-MnFe alloys with a small amount of Cu. Neutron diffraction experiments were made by a diffractome-ter installed at the JRR-3M reactor at JAERI for the f.c.o. phase in γ-MnPd and γ-MnFe(Cu).

The neutron diffraction pattern for the γ-MnPd alloy with 10.5 at % Pd at 10 K is explained by assuming the f.c.o. structure with a = 3.836, b = 3.776 and c = 3.709 A and a non-collinear antiferromagnetic structure with μ_a= 0, μ_b = 1.01 and μ_c = 1.71 μ_B / Mn atom. The angle between the z-axis and the magnetic moment is 31° . This magnetic structure is very similar to that of the γ-MnGa alloy shown in Fig. 1 (b).

Since the face-centered structure (γ-phase) of Mn rich MnFe alloys can not easily be retained at room temperature, a small amount of third element, Cu, should be added into the alloys for the possible quenching from a temperature of the stable region to room temperature. A powder sample of γ-$(Mn_{0.74}Fe_{0.26})_{0.95}Cu_{0.05}$ was prepared for the neutron diffraction experiment. We have confirmed by X-ray diffraction experiments that the sample shows the f.c.o. structure with a = 3.682, b = 3.648 and c = 3.627 A at 16 K. In the neutron diffraction pattern at 10 K, no nuclear reflections appear since the composition of the sample corresponds to a null lattice for the neutron diffraction, i.e. the average nuclear scattering amplitude, b, is nearly zero. However, magnetic reflection intensities are strong enough. Thus we have determined relative magnetic moments: μ_a= 0 and μ_b/μ_c=0.60. Thus the angle between z-axis and the magnetic moment is 31° , being equal to that for the γ-MnPd alloy. Results of the present work are also consistent with the theoretical presentation by Jo et. al.

References

[1] N. Honda et al: J. Phys. Soc. Jpn. **41** (19976) 1931.
[2] N. Cowlan et al: Physica B+C. **86-88** (1977) 267
[3] T. Jo et al: J. Phys. Soc. Jpn. **55** (1986) 2017.
[4] T. Hori et al: Physica B **213 & 214** (1995) 354.

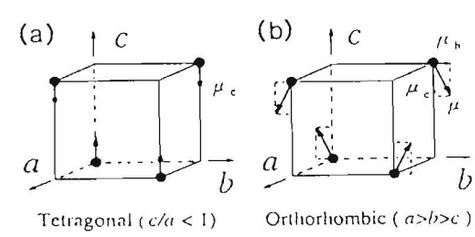

Fig. 1. Magnetic structure for γ-Mn alloys. (a) the magnetic moment μ_a= 0, μ_b = 0 and μ_c >0 and (b) the magnetic moment $\mu_c > \mu_b > \mu_a = 0$.

2.2.6

Magnetic Diffuse Scattering of $Zn_{1-x}Mn_xTe$ with x = 0.432 at B = 0 and 5 Tesla

K.Sato,Y.Ono,S.Shamoto,Y.Morii[1] ,T.Sato[2],Y.Oka[2] and T.Kajitani

Department of Applied Physics, Faculty of Engineering, Tohoku University, Sendai 980-77
Japan Atomic Energy Research Institute, Tokai, Ibaraki 319-11
[2]Research Institute for Scientific Measurements, Tohoku University, Sendai 980-77

The title crystal is a typical II-VI-type semiconductor doped with magnetic atoms, termed as a magnetic semiconductor. It undergoes paramagnet - spin glass transition at about 20K. The transition temperature, Tg, increases from 0K to 45K with increasing Mn content up to x=0.7. High Resolution Powder Diffractometer (HRPD) was used to study magnetic ordering in the powder and single crystal samples, either. The magnetic field up to 5 Tesla was applied vertically to the scattering plane by the use of a superconducting magnet. Powder and single crystal samples were prepared by melting and mixing pure Zn, Mn and Te in thick walled quartz tubes. The Bridgeman method was adopted to grow single crystals. The neutron diffraction measurements were carried out with the incident monochromatic radiation at λ =1.8232 Å.

The powder diffraction patterns exhibit strong diffuse intensity in the scattering angles from 10 to 25 degree at 5K, being in the spin-glass regime, but the intensity is not observed at room temperature. The central position of the diffuse intensity corresponds to the wave number of Q = (1/2 1 0) which is the characteristic reciprocal lattice point of the type-III antiferromagnetic ordering of fcc lattices, an indication of the type-III short range magnetic ordering of the Mn moment. Mn atoms are situated in the Zn-position (one of the two fcc sublattices) of the Zinc-blende type ordered crystal. Extra small Bragg peaks indexed as 1/2 1/2 1/2 and 1/2 1/2 1 are also observed at 5K. The single crystal diffraction measurement was performed at temperature in a range from 10K to 80K at the magnetic field of B=0 and 5 Tesla. The measurement was done in the hk0 plane in the Q-space. Since HRPD has many neutron counters and can observe diffraction intensities with high S/N ratio at different wave numbers simultaneously, the machine is suitable to measure weak scattering intensities spread over the reciprocal space 2- or 3-dimensionally. The diffuse scattering was observed in the vicinities of 1/2 1 0 , 1 1/2 0 and their equivalent positions through the above temperature range, but the intensity increases with decreasing temperature. The diffuse intensities are elongated to 010 and 100 from 1/2 1 0 and 1 1/2 0 positions in the hk0 plane at B=0. The 0 1 0 and 1 0 0 reciprocal lattice points correspond to the type-I antiferromagnetic ordering of fcc lattices. Figure shows obtained diffuse intensities at 10K with B= 5 Tesla. The diffuse intensities at 010 and 100 seems lowered in the magnetic field of B=5 Tesla, suggesting the stabilization of the type-III ordering relative to the type-I. Similar diffuse magnetic scattering was observed in the $Cd_{1-x}Mn_xTe$ with x=0.44 by Gibultowicz et al. (T.M.Gibultowicz et al.: J.Magn.Magn.Mater. 54-57(1986)1149.)

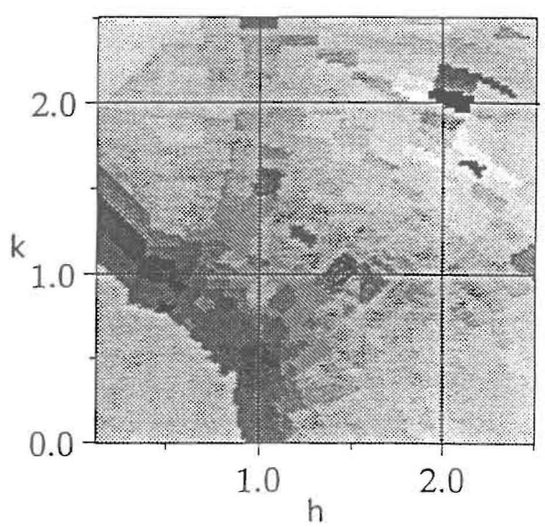

Fig.1 Diffraction intensity in hk0 plane at 10K and 5Tesla

2.2.7

Magnetic and Structural Properties of Reduced Praseodymium titanates

A. Nakamura and K. Yoshii[2]

Dept. of Chemistry & Fuel Research and [2]Advanced Science Research Center,
Japan Atomic Energy Research Institute, Tokai, Ibaraki, 319-11

As a part of our research program on the highly reduced 3d and 4d metal-complex oxides, a series of new perovskite- type reduced Pr titanates: $Pr_{2/3}TiO_{3-x}$ ($0 \leq x \leq 1.0$) were prepared by conventional ceramic methods, and their formation process, structural and physical properties are being studied by means of EPMA method, powder XRD and HRPD methods and magnetic susceptiblity(χ) measurements, etc.. Fig.1 shows the results of χ measurements of various systems prepared in the present study. It is apparent that with increasing the oxygen deficiency(x) from 0 to 1.0, i.e., with reducing the Ti mean-valence from 4+ to 2+, magnetic ordering of the system is brought about, the highest transition temperature reaching at ~127K for the

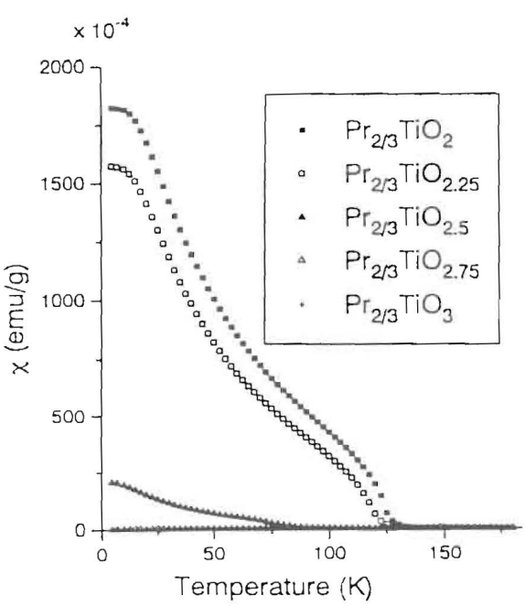

Fig.1 χ vs. T Plots of $Pr_{2/3}TiO_{3-x}$

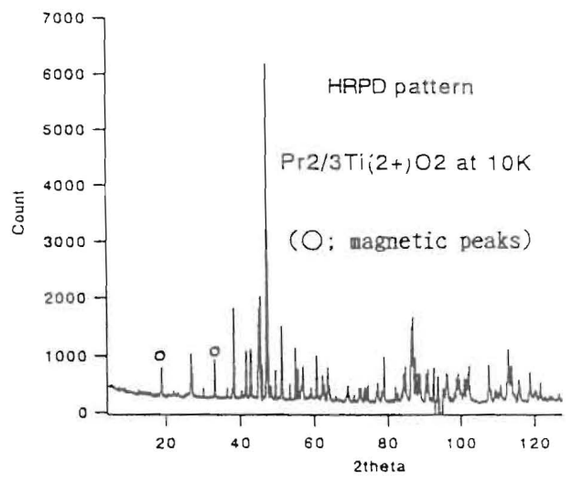

Fig.2 HRPD Pattern of $Pr_{2/3}TiO_2$ at 10K:

most reduced Ti^{2+} system(oxygen nonstoichiometry(x) and Ti mean-valence denoted here are those of the starting mixtures). Fig.2 shows the HRPD pattern of this most reduced $Pr_{2/3}TiO_2$ system at 10K. Compared to that at room temperature, several magnetic peaks appear and grow at temperatures below T_N ~127K(100, 50 and 10K). In previous study on similar system($PrTiO_3$), it is suggested that the magnetic ordering of these reduced Pr titanates is a multi-step type, that of Ti spin first at higher temperature and then also that of Pr spin at lower temperature. The present χ result in Fig.1 also exhibit a similar two-step magnetic ordering behavior. In order to elucidate more in detail the structural and magnetic properties of these systems, detailed analysis of HRPD(and XRD) results, together with the EPMA phase analysis, are now in progress.

2.3 STRONGLY CORRELATED ELECTRON SYSTEMS AND SUPERCONDUCTIVITY

2.3.1 Coupling between Magnetic and Superconducting Order Parameters and Evidence for the Spin Excitation Gap in the Superconducting State of a Heavy Fermion Superconductor UPd_2Al_3

N. Metoki[A,B], Y. Haga[A], Y. Koike[A], N. Aso[A,B], Y. Ōnuki[A,C],

[A]*Advanced Science Research Center, JAERI, Tokai, Ibaraki 319-11*
[B]*Physics Department, Graduate School of Science, Tohoku University, Sendai 980-77*
[C]*Department of Physics, Osaka University, Toyonaka, Osaka 560*

Heavy fermion superconductor (HFSC) attracts strong interests in recent study of strongly correlated electron systems. The most important issue for HFSC's is the interplay between the magnetism and superconductivity. Because of the strong repulsion between *f*-electrons, non-BCS superconductivity is expected to be favorable. In fact recent NMR study of UPd_2Al_3 reported *d*-wave paring with anisotropic gap, vanishing on lines.[1] Furthermore, as an origin of the non-BCS superconductivity, spin fluctuations are considered to be the most plausible candidate for the pairing interaction. In order to study (i) the interplay between the magnetism and superconductivity, (ii) non-BCS gap, and (iii) the origin of the superconductivity, We have carried out neutron scattering experiments on UPd_2Al_3.

A cold neutron triple-axis spectrometer LTAS was used. The incident beam (E_i = 4.4 meV) was monochromatized by a vertically bent PG with a Be filter. The collimation was 26'-70'-72'-72'. The resolution was 0.18 meV in the elastic condition. The single crystal samples were grown by the Chochralski pulling method in a tetra-arc furnace. T_c and the residual resistivity ratio are 1.9 K and 60, respectively.[2]

A resolution-limited AFM Bragg peak is observed below T_N. Figure 1 shows the temperature (T) dependence of the (0 0 0.5) AFM peak intensity under the magnetic field H ($\perp$ scattering plane). We have observed anomalous suppression of the peak intensity below the superconducting transition temperature denoted by arrows in Fig. 1. The intensity increases monotonically for H = 3 T. At this field the sample exhibits no superconducting transition. These results are understood in terms of the coupling between magnetic and superconducting order parameters. The coupling would be a characteristic feature in HFSC, since similar results are reported in UPt_3 [3] and UNi_2Al_3.[4] It should be noted that there is a close correlation between the reduction rate and the moment value; about 10% in UPt_3 (0.02 μ_B), 3 % in UNi_2Al_3 (0.2 μ_B) and 1 % in UPd_2Al_3 (0.85 μ_B/U).

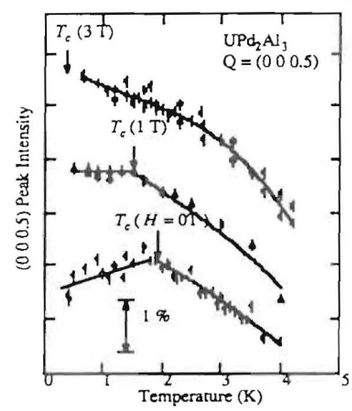

Fig. 1. Temperature-dependence of the (0 0 0.5) AFM peak intensity.

Figure 2 shows constant-Q scan at (0 0 0.5) as a function of temperature. At T = 4.2 K, the profile can be described by a broad quasi-elastic (dotted line) and an inelastic Lorentzian at ΔE = 1.5 meV (dashed line). The inelastic peak is attributed to a spin-wave excitation as reported before. The quasi-elastic scattering would be some kind of thermal fluctuation, because the intensity decreases with decreasing the temperature. Below T_c, however, the quasi-elastic scatterung exhibits a remarkable shift of the peak position. At 0.4 K we observed an

inelastic peak with the excitation energy of about 0.4 meV. The data can be fitted by an inelastic Lorentzian. This peak can not be explained by the quasi-elastic lineshape. The transition from quasi-elastic to inelastic profile corresponds to the formation of the gap. This is the first observation of the spin excitation gap emerging in the superconducting state of a HFSC.

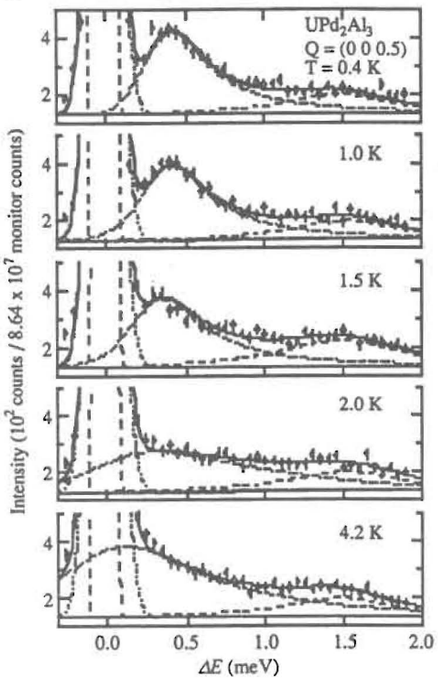

Fig. 2. Temperature-dependence of the magnetic excitation spectra at $Q = (000.5)$.

The gap energy of about 0.4 meV = 2 $k_B T_c$ is in the same order as the superconducting gap expected from the weakly-coupled BCS theory, $2\Delta = 3.5\ k_B T_c$. Moreover, the gap exhibits a clear T-dependence comparable to the BCS theory (dotted line). Therefore, it is concluded that the observed gap corresponds to the superconducting gap. The line width of the inelastic peak exhibits a sharp decrease below T_c, idicating an increase of the lifetime of this spin fluctuation. Analogous to the phonons relevant to the BCS superconductivity, this behavior would be evidence that the superconductivity in UPd_2Al_3 is magnetic origin. The peak intensity shows a continuous increase below T_c, roughly following the BCS order parameter (Fig. 3 (b)).

A similar behavior is observed in the T-dependence of the scattering intensity at ΔE = 0.4 meV (Fig. 3(b) Inset). This behavior is reminiscent of the T-dependence of a so called 41 meV peak in YBaCuO.[5]

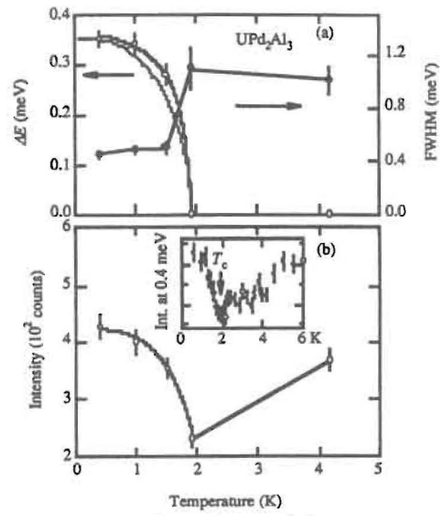

Fig. 3. Temperature-dependence of the gap energy, line width, and intensity.

With applying H, the gap and the intensity of the peak decreases, and it disappears for $H > H_{c2}$. From these results we can conclude that the inelastic peak is related to the superconductivity.

Inelastic neutron scattering profile has been measured as a function of Q. The gap becomes larger as Q deviates from the AFM Bragg point (0 0 0.5). It would be a signiture of the anisotropic gap (See Overview, Fig.7).

In conclusion, we have observed the close coupling between the magnetic and the superconducting order parameter. Spin excitation gap is found for the first time in the heavy fermion superconductors. These results are indicative of the strong interplay between magnetism and superconductivity in UPd_2Al_3.

References

1) M. Kyogaku et al., J. Phys. Soc. Jpn. **62** (1993) 4016
2) Y. Haga et al., J. Phys. Soc. Jpn. **65** (1996) 3646.
3) G. Aeppli et al., Phys. Rev. Lett. **60** (1988) 615.
4) N. Sato et al., to be published.
5) H.A. Mook et al., Phys. Rev. Lett. **70** (1993) 3490.
6) N. Sato et al., to be published in J. Phys. Soc. Jpn.

2.3.2 Interplay between Magnetism and Superconductivity in a Heavy Fermion Superconductor UPd_2Al_3

Y. Koike[1], N. Metoki[1], Y. Haga[1], Y. Morii[1] and Y. Ōnuki[1,2]

[1] *Advanced Science Research Center, JAERI, Tokai, Ibaraki 319-11*

[2] *Graduate School of Science, Osaka University, Toyonaka, Osaka 560*

Heavy fermion superconductor has attracted strong interest because of the interplay between magnetism and superconductivity. UPd_2Al_3 has the highest superconducting transition temperature with T_C = 2 K and relatively large magnetic moment of $0.85\mu_B$. Our recent neutron scattering study revealed the coupling between magnetic and superconducting order parameters. The spin excitation gap is found to emerge below the superconducting transition temperature T_C = 2 K [1]. Following the first paper, neutron scattering experiments have been carried out in order to elucidate the coupling between antiferromagnetic ordering and the superconductivity.

The neutron scattering experiments were carried out using a cold neutron triple-axis spectrometer LTAS with ^{3}He cryostat. The configuration of the spectrometer and samples were the same as before.

Figure 1 shows the temperature dependence of the peak intensities. The (0 0 0.5), (0 0 1.5), (1 0 0.5) magnetic peak exhibits continuous increases with decreasing temperature below the Néel temperature T_N = 14.5 K. The intensities begin to decrease below T_C and show about 1% reduction of the maximum value. Meanwhile (0 0 1) nuclear peak shows no anomaly at T_C. The reduction of the magnetic peak intensities is understood in terms of the coupling between magnetic and superconducting order parameter. The no temperature dependence of the nuclear peak rules out the possibility that the behavior of the magnetic peak is due to a lattice distortion and/or a slight change of the absorption for neutrons associated with superconductivity.

The inelastic neutron scattering profiles at fixed Q = (0 0 0.5), (0 0 1.5), (1 0 0.5) and (0 0 1) are measured below and higher than T_C. When the scattering vector is fixed at the magnetic Bragg points, an inelastic peak has been observed at the excitation energy ΔE = 0.4 meV below T_C. These inelastic peaks are considered to be due to magnetic excitation gap, emerging in the superconducting state. At Q = (0 0 1), we observed

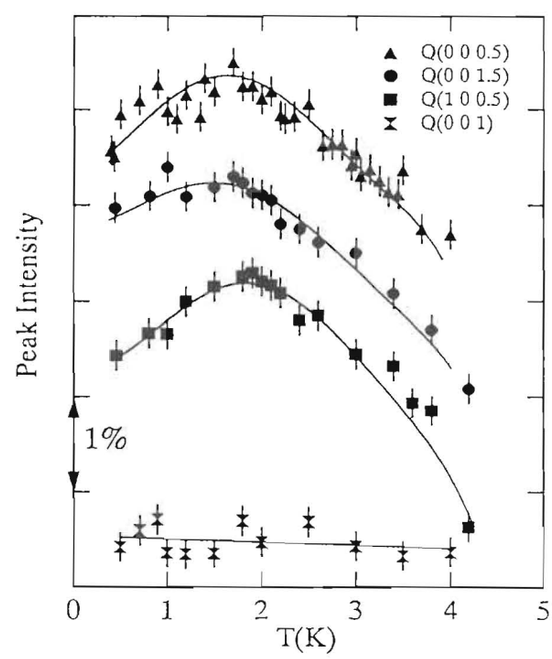

Fig.1 Temperature dependence of peak intensities at Q=(0 0 0.5), (0 0 1.5), (1 0 0.5) and (0 0 1). Lines are guide to eyes. Each data are shifted for convenience of comparison.

no inelastic scattering beyond the statistic error of the background. Furthermore, the integrated intensity of the inelastic peak is proportional to the one of magnetic Bragg peak. Therefore we conclude that the observed inelastic peak is due to magnetic fluctuations related to the antiferromagnetic ordering of UPd_2Al_3. Our recent study reported that the magnetic excitation gap exhibits a remarkable temperature dependence similar to the superconducting gap. These results indicate that the antiferromagnetism and superconductivity are strongly correlated.

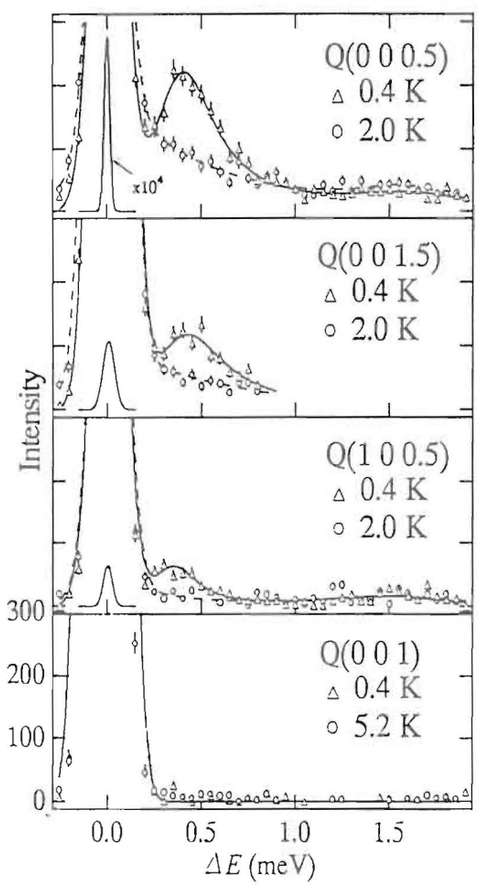

Fig.2. Q-dependence of the inelastic neutron scattering profile. Notaions of triangle and circle are experimental value which is subtract farst nutron back ground.

Figure 3 is the constant-E scan along the (0 0 l) direction with the fixed ΔE = 0.4 meV. We found that the inelastic peak at (0 0 0.5) becomes sharp and strong below T_c. Except for the (0 0 0.5) peak, no significant difference in scattering intensity was observed. We obtained similar result for (h 0 0.5), where $-0.1 < h < 1.3$. It means that the inelastic scattering peak is observed in a very narrow region around the magnetic Bragg point, and exhibits strong damping in the other region of the q-ω space.

In conclusion, we observed remarkable temperature dependence of the elastic and inelastic scattering at antiferromagnetic Bragg points, indicating the strong coupling between antiferromagnetism and superconductivity in UPd_2Al_3.

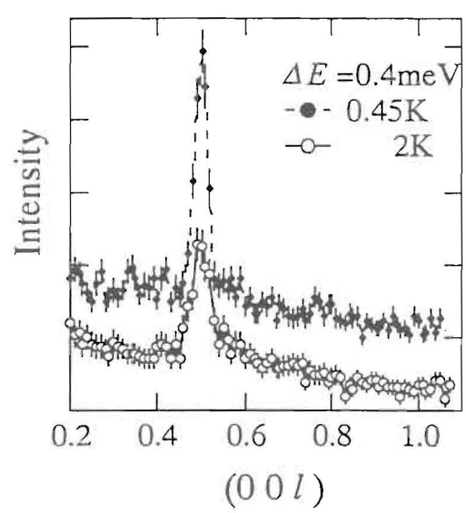

Fig.3. Q-dependence of the inelastic neutron scattering intensity. Each data are shifted for convenience.

Reference

1) N. Metoki, et al., to be published in J. Phys. Soc. Jap.

2.3.3

Anomaly in the spin wave excitation associated with the superconductivity in UPd_2Al_3

Y. Haga[1], N. Metoki[1], Y. Koike[1] and Y. Ōnuki[1,2]

[1] *Advanced Science Research Center, JAERI, Tokai, Ibaraki 319-11*
[2] *Graduate School of Science, Osaka University, Toyonaka 560*

Among the heavy fermion superconductors, UPd_2Al_3 has the highest superconducting transition temperature $T_c = 2$ K and the largest magnetic moment 0.85 μ_B/U. [1,2] The d-wave pairing is revealed from NMR studies.[3] Recent our neutron scattering experiment provided clear evidence for the interplay between magnetism and superconductivity in this compound. [4] First, the temperature dependence of the (0 0 0.5) Bragg intensity exhibited a remarkable kink at T_c. Second, a magnetic excitation gap of $2k_BT_c$ was obseved below T_c.

At higher energy ($\Delta E \simeq 1.5$ meV) than the magnetic excitation gap we observed a broad inelastic peak which would be attributed to the *spin wave excitation* reported previously.[3] The *spin wave excitaion* shows strong damping in the normal state, and it is quite different from usual localized magnets. The purpose of this study is to reveal the influence of the superconductivity on this *spin wave excitation*.

Experiments were carried out using a thermal neutron spectrometer TAS-2 ($k_i = 2.58$ Å^{-1}). The resolution was 0.9 meV at $\Delta E = 0$. Single crystalline samples ($T_c = 1.9$ K) were grown in a tetra-arc furnace. [6] Samples were mounted with the ($h0l$) plane parallel to the scattering plane and cooled to 0.4 K in a ^{3}He cryostat. The magnetic field is applied perpendicular to the scattering plane.

Figure 1 shows the spin wave excitation measured at 0.4 K around the (0 0 0.5) magnetic Bragg point. Peterson et al. reported that the spin wave excitation is gapless at the zone center. However our recent high resolution experiments with cold neutrons revealed that the observed spectrum is fitted with a gap better than the gapless profile. Therefore we fit the spectra of this low energy-resolution experiment by an inelastic Lorentzian line shape. The obtained dispersion curve is shown in the inset of Fig. 1.

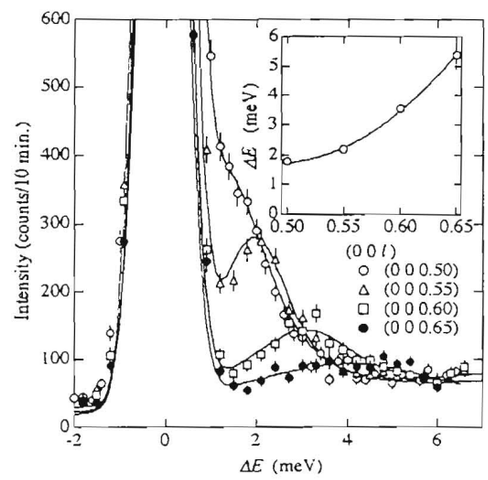

Figure 1: Spin wave excitation spectra of UPd_2Al_3 measured at 0.4 K. Inset: The dispersion curve of the spin wave.

The spin wave excitation spectra at $Q = (0\ 0\ 0.5)$ is measured below and above T_c. As shown in Fig. 2 we found significant difference in the scattering intensity around 1.8 meV. This energy roughly corresponds to the peak position of the spin wave excitation obtained by fitting the data.

Figure 3 is the temperature dependence of the scattering intensity at 1.8 meV in various magnetic fields. For $H = 0$ the scattering intensity increases from the Néel Temperature T_N. Surprisingly, an enhancement of the intensity is observed at $T_c = 1.9$ K. Below T_c the scattering intensity exhibits an unusual decrease with decreasing temperature. At $H = 1.5$ T, the scattering intensity exhibits very similar temperature dependence with the zero-field data. The enhancement of the

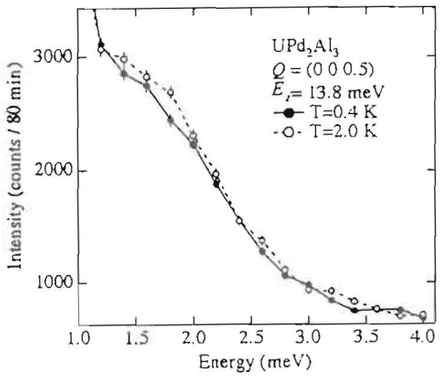

Figure 2: Inelastic scattering profile at Q = (0 0 0.5) in superconducting state (T = 0.4 K) and normal state (2.0 K).

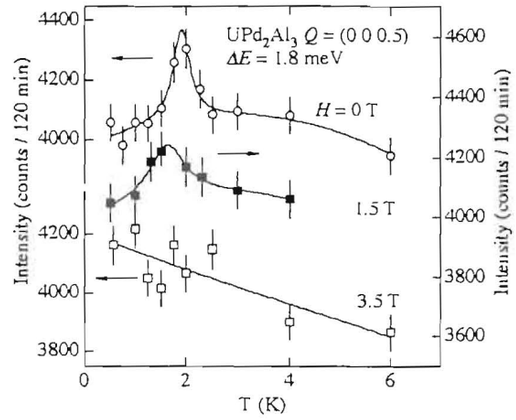

Figure 3: Temperature dependence of the intensity at 1.8 meV under magnetic fields.

of the peak becomes weak and appears at 1 K, which corresponds to T_c in this field. At H = 3.5 T the scattering intensity shows a continuous increase below T_N. We expect no superconducting transition in this field which is larger than the critical field H_{c2} = 3 T. From these results it is clear that the enhancement of the peak and the decrease of the intensity below T_c are closely related to the superconductivity in UPd_2Al_3. It is of particular interest that we observed influence of superconductivity at the energy transfer 1.8 meV $\simeq 10k_BT_c$, which is considerably larger than the energy scale of T_c.

The origin of the anomalous behavior of the *spin wave excitation* is not so clear yet. It should be noted that the enhancement of the scattering intensity starts above T_c, and observed in the very narrow temperaure range. Therefore it would be due to the fluctuation of the superconductivity, which exhibits an anomalous enhancement of the spin wave excitation through the coupling between magnetism and superconductivity. On the other hand, the decrease of the scattering intensity would be understood in terms of the *sum rule* for spin excitations. As revealed previously the intensity of the inelastic peak at ΔE = 0.4 meV increases very rapidly below T_c like a superconducting order parameter. Assuming the *sum rule* we would expect a decrease of the spin wave excitation in the corresponding way.

In conclusion, we observed an anomalous enhancement and a decrease of the spin wave excitation in the superconducting state of UPd_2Al_3. The present result demonstrates that the superconductivity has influence on the magnetic excitation up to considerably high energy transfer. The anomaly in the magnetic Bragg intensites (ΔE = 0 meV) and the magnetic excitation gap (0.4 meV) published previously, as well as the anomaly in the spin wave excitation spectra (1.8 meV) would give an insight into the novel mechanism of the heavy fermion superconductors.

References

1) C. Geibel et al.: Z. Phys. B84 (1991) 1.
2) A. Krimmel et al.: Z. Phys. B86 (1992) 161.
3) H. Tou et al.: J. Phys. Soc. Jpn. 64 (1995) 725.
4) N. Metoki et al.: to be published in J.Phys.Soc.Jpn.
5) T.E. Mason et al.: *RisøReport* R-660 (1993) 37.
6) Y. Haga et al.: J. Phys. Soc. Jpn. 65 (1996) 3646.

2.3.4 Magnetic Structure of a Heavy Fermion Superconductor UNi_2Al_3

N. Aso[A,B], N. Metoki[A,B], N. Sato[B], T. Komatsubara[C] and Y. Endoh[B]

[A]*Advanced Science Research Center, Japan Atomic Energy Research Institute, Tokai, Ibaraki 319-11*
[B]*Physics Department, Graduate School of Science, Tohoku University, Sendai 980-77*
[C]*Center for Low Temp. Sci., Tohoku University, Sendai 980-77*

The uranium intermetallic compound UNi_2Al_3 is well known to exhibit the coexistence of antiferromagnetic ordering (T_N≈4.6K) and superconductivity (T_c≈1.0K). We reported[1] that the incommensurate (IC) magnetic Bragg peak intensity was affected by the onset of the superconductivity, implying the coupling between magnetic and superconducting order parameters. It was suggested that the magnetic phase is the longitudinal spin density wave (LSDW) with k=[0.5±0.11,0,0.5][2]. But so far it was not clear, if the modulation is sinusoidal or rectangular type. The difference of the magnetic structure is of particular important in order to understand the origin and the character of the magnetic ordering which shows strong correlation with superconductivity. The purpose of our neutron scattering experiments is to clarify the magnetic structure of a high-quality single crystal showing superconductivity[3].

The measurements were performed on the triple-axis spectrometer TAS-1 with ^{3}He cryostat. The neutron energy (E_i=14.7 meV) is monochromatized and analyzed by PG crystals. Higher harmonics were removed by a PG filter. The sample is grown by Chochralsky method. The (h 0 l) plane has been measured in this study.

In spite of very careful experiments, no significant difference of the scattering intensity has been observed at the 3rd-order satellite above T_N and at 1.4 K. From the statistic error of our measurements the magnetic structure factor of the 3rd-order satellite is expected to be less than 1.9 % of the 1st-order one.

$$\frac{F(Q=(0.5-3\delta,0,0.5))^2}{F(Q=(0.5-\delta,0,0.5))^2} < (1.90 \pm 0.05)\%.$$

The structure factor of the 3rd-order satallite is estimated to be 12% from the model calculations of rectangular wave structure. It is one order of magnitude larger than the experimental results. There are two possibilities to understand the undetectably weak 3rd-order satallite; The magnetic moments exhibit a sinusoidal modulation (spin density wave) or rotate in the c-plane (cycloid structure). As described below, however, the Q-dependence of the magnetic Bragg intensities rules out the cycloid structure.

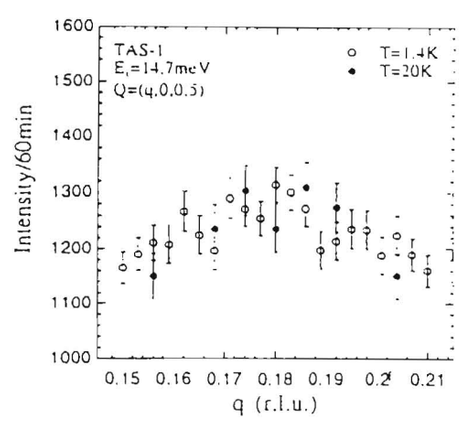

Fig. 1 The elastic neutron scattering profile at the (0.18 0 0.5) 3rd-order satellite.

Figure 2 shows the magnetic Bragg intensity corrected for both the Lorentz factor and the magnetic form factor. The lines are the least-square fits to the models for the various magnetic structures. The best one which reproduces these measurements is that of the LSDW magnetic structure. The cycloid structure is not consistent with the experimental data. Therefore we conclude that UNi_2Al_3 exhibits a sinusoidal modulation of the magnetic moment; the 3rd-order modulation is considered to be very small.

We also calculated the magnetic moment $\mu_U=(0.19\pm0.01)\mu_B$. The above results are consistent with the previous results[2].

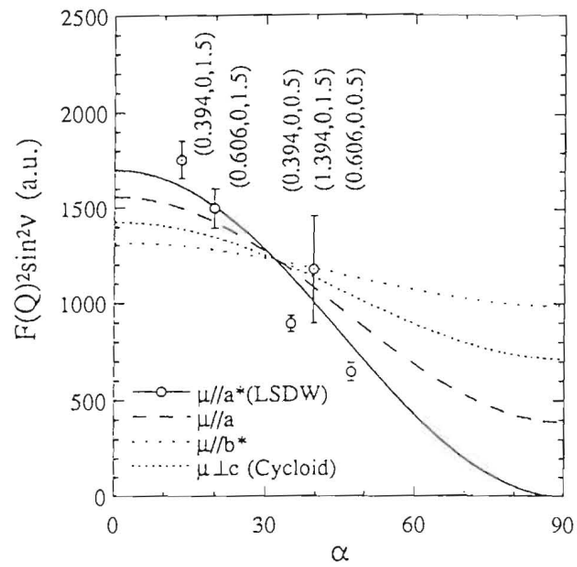

Fig. 2 The intensity of magnetic Bragg points in UNi_2Al_3. α and ν are the angles between Q and c^* axis and between Q and the moment direction, respectively. The lines are the model calculations with differing polarizations μ within the c plane.

References

1) N. Metoki *et al.*, *Meeting Abst. Phys. Soc. Jpn.* 51 (1996) Issue 2, Part 3, 2a-YE-11.

2) A. Schröder *et al.*, *Phys. Rev. Lett.* 72 (1994) 136.

3) N. Sato *et al.*, *J. Phys Soc. Jpn.* 65 (1996) 1555.

2.3.5 Neutron Scattering Studies of Ternary Uranium Antiferromagnet UNiSn

T. Osakabe[1], T. Takabatake[2], M. Shirase[2], E. Yamamoto[1], Y. Haga[1], Y. Ōnuki[1,3]

[1]Advanced Science Research Center, Japan Atomic Energy Research Institute, Tokai, Ibaraki 319-11
[2]Faculty of Science, Hiroshima University,Kagamiyama, Hiroshima 739
[3]Faculty of Science, Osaka University, Toyonaka, Osaka 560

In recent years, the ternary uranium compounds have attracted much interest owing to their large variety in magnetic, structural and transport properties, which are mainly caused by the 5f-ligand hybridization. In these compounds, UNiSn is known to exhibit an unusual phase transition. At higher temperature, this compound is a semiconducting paramagnet with cubic MgAgAs type crystal structure. Below the transition temperature of 43K with the first order nature, the compound becomes a metallic type-I antiferromagnet with distorted tetragonal structure. Thus, the compound shows the antiferromagnetic, semiconductor-metal and structural transitions at 43K. The origin of the transition, however, is unclear yet. To elucidate the origin of the transition from the microscopic point of view, we performed inelastic neutron scattering experiments.

The polycrystalline sample was prepared by melting together the stoichiometric amounts of U, Ni, and Sn using the tetra arc furnace in argon atmosphere and then annealing for 90 days at 800 °C in a vacuum quartz container. Experiments have been performed on the triple axis spectrometer TAS-1(2G) at JRR-3M, JAERI. The spectrometer was set up to generate the incident neutron energy (Ei) of 30.5 meV with open-80'-80'-80' collimation and that of 82.1 meV with 40'-40'-40'-40'. The sample set in the Al container with ^{4}He gas was mounted on the closed cycle refrigerator (CTI).

Fig. 1(a) and (b) show the neuron inelastic scattering spectra of UNiSn in Ei = 30.5 meV and 82.1 meV, respectively. Well-defined peaks are observed at 10 meV in Fig. 1(a) and 40 meV in Fig. 1(b) at low temperature. The intensities of both peaks decrease considerably at higher temperature or higher Q. This indicates that the peaks correspond to the crystalline electric field (CEF) excitations from the ground to first and second excited states of U ion. On the other hand, the peak at around 17 meV corresponds to the phonon contribution.

The results of the experiments indicate that the 5f-electrons of the compound have localized character. Aoki et al.[1] explained the results of their susceptibility measurements by a model based on the localized 5f electrons in the CEF. They determined the CEF level scheme by assuming the $5f^2$ configuration of U^{4+} ion. According to them, the CEF level scheme consists of a non-magnetic doublet ground state Γ_3, a magnetic first excited triplet state Γ_4 with energy of 180K from Γ_3, a second excited singlet state Γ_1 with 430K and a third excited triplet Γ_5 with about 3000K. Suzuki et al. [1] clamed the idea based on the CEF level scheme proposed by Aoki et al. that the transition in UNiSn is originated from a sort of cooperative effect between magnetic(Γ_4) and Jahan-Teller structural instability(Γ_3). Because the obtained CEF level scheme in neutron scattering experiments is near to that proposed by Aoki et al., the above idea to explain the transition is supported. To elucidate the origin of the transition, however, more precise neutron scattering experiments on magnetic form factor are necessary.

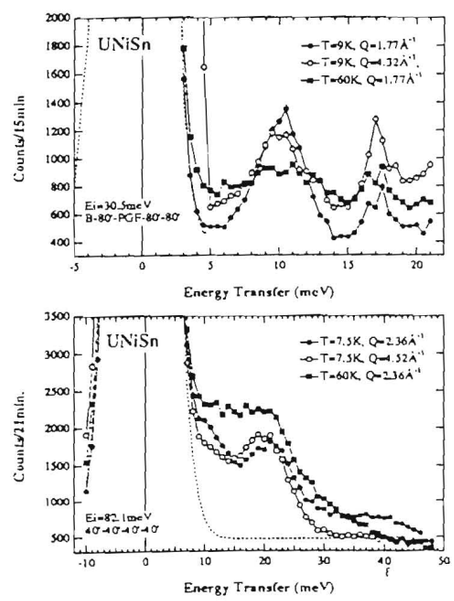

Fig. 1 The neuron inelastic scattering spectra of UNiSn in (a) Ei = 30.5 meV and (b) Ei = 82.1 meV.

References

1) Y. Aoki et al., Physical Review B 47 (1993) 15060
2) T. Suzuki et al., Physica B 199&200 (1994) 483

2.3.6 Magnetic Structures of CeP under High Pressure

T. Osakabe, M. Kohgi[1], K. Iwasa[1], Y. Haga and T. Suzuki[2]

Advanced Science Research Center, Japan Atomic Energy Research Institute, Tokai, Ibaraki 319-11
[1]Department of Physics, Tokyo Metropolitan University, Hachioji, Tokyo 192-03
[2]Department of Physics, Tohoku University, Sendai 980-77

CeP is a low-carrier-density semi-metallic compound with NaCl-type crystal structure. From macroscopic measurements such as resistivity, specific heat and susceptibility, it was found that CeP exhibited unusual properties such as complex magnetic phase diagram under magnetic field and pressure or Kondo-like transport properties [1]. Since it is quite crucial to elucidate unknown magnetic structures in the phase diagram to understand the origin of the unusual properties of CeP, we have started neutron diffraction experiments under magnetic field and pressure. In the previous report [2], we showed results of neutron diffraction experiments under pressure. We explained that the complex P-T phase diagram and the magnetic structures were originated from the interplay between the antiferromagnetism of the CEF ground state Γ_7 and the formation of the Γ_8 magnetic polaron lattice. In this report, we point out residual problems on the neutron diffraction experiments.

Here, we show again the P-T phase diagram and the magnetic structures in Fig.1. As shown in Fig.1, the structure "8" was not observed yet in spite of the wide and systematic change of the magnetic structures with changing pressure. From the recent experiments at around 0.7 GPa, it is concluded that the pressure value where the structure "8" is expected to exist is between 0.60 GPa and 0.75 GPa. However, the structure "8" was not observed directly since it is difficult for piston-cylinder and clamp type high pressure cells such as McWhan type cell to keep well the target pressure value below about 1.0 GPa through the experiments. Thus, not only to find the structure "8" but to determine accurately the phase boundaries, it is necessary to perform the experiments with scanning along the pressure axis in the phase diagram using a gas pressure and load type high pressure cell, which can change pressure continuously in the cryostat.

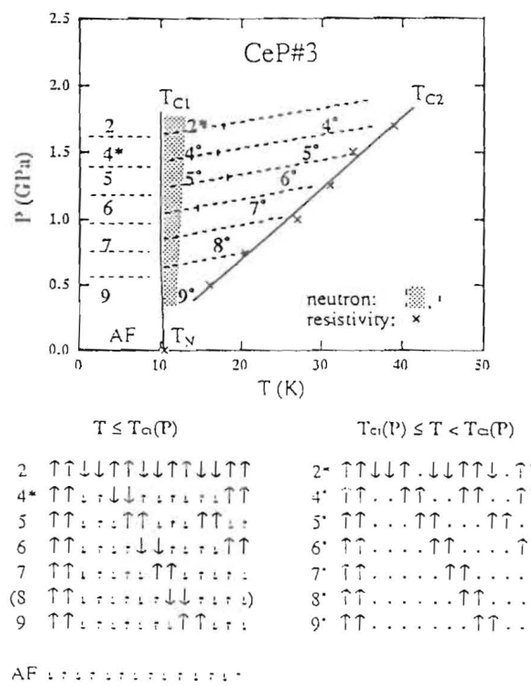

Fig.1 The P-T phase diagram and the magnetic structures of CeP determined by the neutron diffraction experiments. The structure "8" is not observed yet.

Another interesting fact on the P-T phase diagram and the magnetic structures of CeP is that, above about 1.5 GPa, the same magnetic structures as those of CeSb at ambient pressure appear. Thus, it is expected that the P-T phase diagram similar to that of CeSb is observed above about 2.0 GPa. To confirm this point, we now plan to perform neutron diffraction experiments using sapphire-anvil type high pressure cell, which is expected to generate pressure up to about 5.0 GPa.

[1] T. Suzuki, JJAP Series 8 (1993) 267.
[2] T. Osakabe *et al.*, JAERI NSL REPORT (1996) 13.

2.3.7 Vortex Lattice Structure in $CeRu_2$

J. Suzuki[a], N. Metoki[a], Y. Haga[a], E. Yamamoto[a],
H. Kadowaki[b], K. Kakurai[c], M. Hedo[d] and Y. Ōnuki[a,d]

[a]Advanced Science Research Center, Japan Atomic Energy Research Institute, Tokai-mura 319-11
[b]Faculty of Science, Tokyo Metropolitan University, Hachioji 192-03
[c]The Institute for Solid State Physics, The University of Tokyo, Roppongi 106
[d]Graduate School of Science, Osaka University, Toyonaka 560

The mixed state of an f electron superconductor $CeRu_2$ with the large paramagnetic susceptibility has been investigated intensively because of its unconventional peak-effect in dc-magnetization[1]. The presence of the peak-effect indicates strong pinning of vortices over a field range $H^* < H < H_{c2}$ (where H_{c2} is the upper critical field), although weak pining is suggested by almost reversible hysteresis in a field range $H_{c1} < H < H^*$ (where H_{c1} is the lower critical field). The generalized Fulde-Ferrell-Larkin-Ovchinnikov (FFLO) state, in which the reconstruction of vortices due to spatially modulated superconducting order parameter enhances an effective pinning force, is proposed as a possible origin of the anomalous peak-effect phenomenon[2]. However, the original pinning force even in this state is thought to be caused by impurities and lattice imperfections of the sample. In this work we have investigated the relation between the vortex structure and the pinning force for two $CeRu_2$ samples with different residual resistivity ratios (rrr) through a small-angle neutron scattering (SANS) technique.

Two single crystals of $CeRu_2$ (#6 with rrr = 28 and #10 with rrr = 50) were grown by the Czochralski method in a tetra-arc furnace with successive annealing in a vacuum of 10^{-6} Torr at 700°C for one week[3]. Both the samples for SANS experiments were 3-4 mm in diameter, 20 mm in length, and 0.2-0.25 ° in mosaic width (FWHM). SANS measurements using a wavelength of 0.63 nm were carried out at the small-angle neutron scattering instrument SANS-J of the JRR-3M reactor in JAERI. A magnetic field was applied along the [1-10] crystal direction, nearly parallel to the neutron beam with a divergence of 0.17 °.

Figure 1 shows the result of a typical experiment for the #10 single crystal at T = 1.5 K and H_{ZFC} = 0.1 T, where ZFC denotes zero field cooling. We have observed the Bragg spots from the triangle Abrikosov vortex lattice with a reciprocal lattice vector parallel to the [110] crystal direction. Magnetic field distribution around a vortex reflects normal s-wave paring at low magnetic fields. On the other hand, the vortex lattice structure at high fields changes drastically, depending on how to cool the sample, as reported by A. Huxley et al.[4]. The ZFC vortices make a much better aligned lattice than the field cooled (FC) vortices (Fig. 2). This difference seems to be due to the passage through the peak-effect region at the cooling process. According to dc-magnetization measurements, the peak-effect region becomes narrower, that is, H^* approaches to H_{c2}, when the residual resistivity ratio rrr is lower. This result implies that the peak-effect phenomenon is

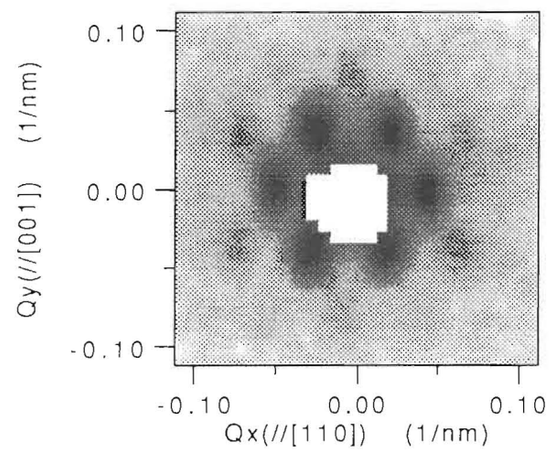

Fig. 1 A 2-dimensional SANS pattern of CeRu2 (#10, rrr = 50) at T = 1.5 K and H_{ZFC} = 0.1 T. A scattering at T = 15K and H = 0 T is subtracted as a background. Qx and Qy is parallel to the [110] and [001] crystal axis, respectively. The field direction is normal to this plane.

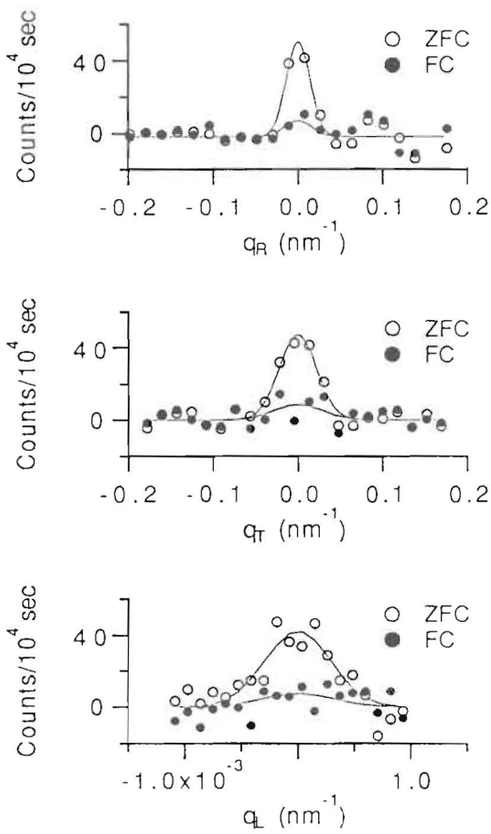

Fig.2 Bragg peaks with different cooling processes measured at T = 1.5 K and H = 3 T. q_R, q_T, and q_L denote the q vectors along the radial, transverse, and longitudinal (// H) directions, respectively.

caused by impurities and lattice imperfections of the sample. Figure 3 shows the temperature independent SANS pattern on the [110]-[001] reciprocal plane of the #6 single crystal at zero field. By rotating the sample around the [001] crystal axis, it becomes clear that the diffuse streaks appear along only the <100>, <110>, and <111> crystal directions. Each scattering reveals almost the same q-dependence. At high-q, the scattering reveals Porod-like q^{-4}-dependence. At below $q \sim 0.1$ nm^{-1}, however, the scattering deviates from the q^{-4}-dependence and changes its intensity slower. This deviation indicates that microstructures with about 50 nm in thickness exist along the <100>, <110>, and <111> crystal directions in the #6 sample with lower quality compared to #10. Such diffuse

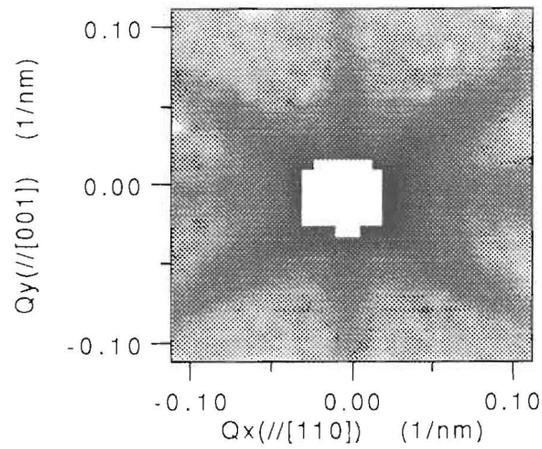

Fig.3 A 2-dimensional SANS pattern of CeRu2 (#6, *rrr* = 28) at room temperature and zero field. Diffuse streaks are observed along the [110], [001] and [111] crystal axes.

scattering was also observed in the #10 crystal, but its magnitude was about 40% of that of the #10 sample. Our data suggest that one of the possible origin of the peak-effect phenomenon is due to the presence of the microstructure containing slight different superconducting characters, because the microstructure may function as the strong pinning force at near H_{c2}. Finer microstructures with about 5 nm in size are also observed by a STM technique[5]. A detailed study to know the superconducting properties of these microstructure is now in progress.

References

1) A. D. Huxley, C. Paulsen, O. Laborde, J. L. Tholence, D. Sanchez, A. Junod, and R. Calemczuk, J. Phys.: Condens. Matter. **5** (1993) 7709.
2) M. Tachiki, S. Takahashi, P. Gegenwart, M. Weiden, M. Lang, C. Geibel, F. Steglich, R. Molder, C. Paulsen, and Y. Onuki, Z. Phys. **B100** (1996) 369.
3) M. Hedo, Y. Inada, T. Ishida, E. Yamamoto, Y. Haga, Y. Onuki, M. Higuchi, and A. Hasegawa, J. Phys. Soc. Jpn. **64** (1995) 4535.
4) A. Huxley, R. Cubitt, D. McPaul, E. Forgan, M. Nutley, H. Mook, M. Yethiraj, P. Lejay, D. Caplan, and J. M. Penisson, Physica **B224** (1996) 169.
5) N. Nishida, private communication.

2.3.8 Existence of Mesoscopic Structure in $NdBa_2Cu_3O_{7-\delta}$ Observed by Small-Angle Neutron Scattering Method

S.Miyata[1,2], K.Osamura[1], J.Suzuki[2], K.Kuroda[3] and N.Koshizuka[3]

[1]Department of Materials Science and Engineering, Kyoto University, Kyoto 606-01
[2]Advanced Science Research Center, Japan Atomic Energy Research Institute, Tokai, Ibaraki 319-11
[3]Superconductivity Research Laboratory, International Superconductivity Technology Center, Koto-ku, Tokyo 135

While in recent years we have performed small-angle neutron scattering (SANS) experiments on the vortex structures of high-T_c superconductors, it is not so easy to detect the signal from the vortices because of the weak magnetic contrasts due to a large penetration depths (λ) compared with those of conventional ones as Nb. The scattering signal is also roughly proportional to $1/\lambda^4$ and then the high-T_c superconductors can give only 10^3-10^4 times smaller signals than that from the Nb sample.

Moreover, it is difficult to grow fine, large single crystals of high-T_c superconductors, so, on SANS experiments, a large amount of scattering from inhomogeneity in the sample makes more difficult to observe the signal from the vortices. However, in the same time, it includes very important structural information of nano-scale about the sample, which can be pinning potential to the vortices.

Recently, $NdBa_2Cu_3O_{7-\delta}$ (Nd123) was reported to have quite large critical current density of 70000 A/cm^2 at 77K, 1Tesla accompanied by peak-effect[1)] and was paid a lot of attention to especially from the view of application research. In Nd123 sample, the Ba ions tend to be easily substituted by the exceeding Nd ions shown as $Nd_{1+x}Ba_{2-x}Cu_3O_{7-\delta}$. The critical temperature (T_c) of the sample $Nd_{1+x}Ba_{2-x}Cu_3O_{7-\delta}$ is reduced as the Nd content (x) increases[2)]. It is then pointed out a possibility that Nd-enriched phases play a important role of pinning potential responsible for the peak-effect phenomenon. In this work we carried out SANS measurements at room temperature in order to investigate the inhomogeneity, giving such pinning potential. The experiments were performed at SANS-J of the reactor JRR-3M using cold neutrons with a wavelength of 1.5 nm. A Nd123 single crystal was prepared by traveling solvent floating zone (TSFZ) method[3)]. Incident beam was parallel to crystallographic *c*-axis, and *a*-axis was aligned along to the horizontal plane. Figure 1 shows a resulting pattern. A diamond-shaped pattern whose main axes corresponds to *a*- and *b*-axes can be seen accompanied with four weak spots on the <110> crystal directions. The positions of these spots suggest the presence of periodic microstructures with a size of about 80nm. This structure is almost consistent with a <110> twin structure due to tetragonal-orthorhombic transition as confirmed by transmission electron microscopy. On the other hand, the diamond-shaped pattern indicates the existence of *a*- and *b*-axis-inclined structure, although the details of the structure is left unresolved.

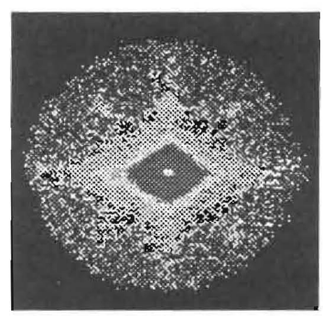

Fig.1 Scattering pattern from Nd123 at room temperature. λ_n=1.5nm. The position of the spot is 0.0783nm^{-1}.

References

1) T.Egi, J.G.Wen, K.Kuroda, H.Unoki and N.Koshizuka, Appl. Phys. Lett. 67 (1995) 2406.
2) K.Takita, H.Katoh, H.Akinaga, M.Nishino, T.Ishigaki and H.Asano, Jpn. J. Appl. Phys. 27 (1988) L57-L60.
3) K.Kuroda, I.H.Choi, H.Unoki and N.Koshizuka, J. Cryst. Growth, to be published.

2.3.9 Charge Ordering in $Pr_{1-x}Ca_xMnO_3$

O. Hino, N. Ikeda[1] and Y. Yamada[1,2]
T. Inami[2] and S. Katano[2]

Advanced Research Center for Science and Engineering,
Waseda University, Ohkubo 3-4, Shinjuku-ku, Tokyo 169, Japan[1]
Japan Atomic Energy reasearch Institute, Tokai, Ibaraki 319-11, Japan[2]

Materials generally expressed by $T_{1-x}D_xMnO_3$ (T: trivalent elements, D: divalent element) has drawn much attention concerning its anomalous transport properties such as giant magneto-resistance. It has been suggested that the key to characterize the system is the subtle balance between the energies associated with electron transfer, electron correlation and electron-phonon coupling. One of the direct manifestation of the characteristics of these materials is seen in the variety of the charge ordering properties.

It was suggested that $Pr_{1-x}Ca_xMnO_3$ (x=0.3) shows charge ordering given by the charge density wave;

$$\rho(\mathbf{r}) = \rho_0 e^{i(1/2, 1/2, 0)\mathbf{r}}.$$

as depicted in Fig. 1 ($\sqrt{2} \times \sqrt{2}$ pattern) which is the same as the well established charge pattern for the case of x=0.5. However, since the x-value is rather close to a stoichiometric value of x=0.25 than x=0.5, it is likely that charge order would give a different pattern from x=0.5 case being locked into the ordering appropriate for x=0.25.

In order to clarify this point, we carried out neutron diffraction measurements, as well as electron diffraction, of a single crystal of $Pr_{0.75}Ca_{0.25}MnO_3$. As is shown in Fig. 2, we observed satellite reflections at 120K at the reciprocal lattice points of

$$Q = (h, k, 0)_c + (\pm 1/4, 0, \pm 1/4)_c.$$

This is certainly different from the diffraction pattern expected for the case of $\sqrt{2} \times \sqrt{2} \times 1$ unit cell for x=0.5 case. At the same time, we observed another type of satellites at Q = (0, 0, l)c + (0, 0, 1/2)c which are prohibited in space group ***Pbmc***. These experimental results are in the process of the analysis to find the proper charge order pattern.

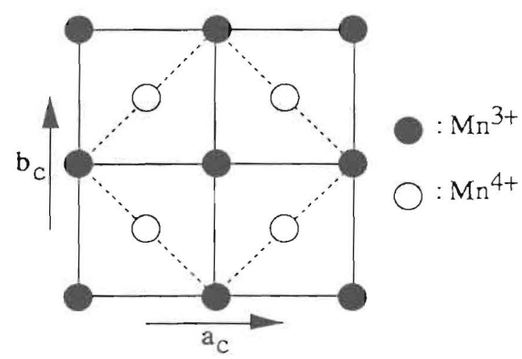

Fig. 1

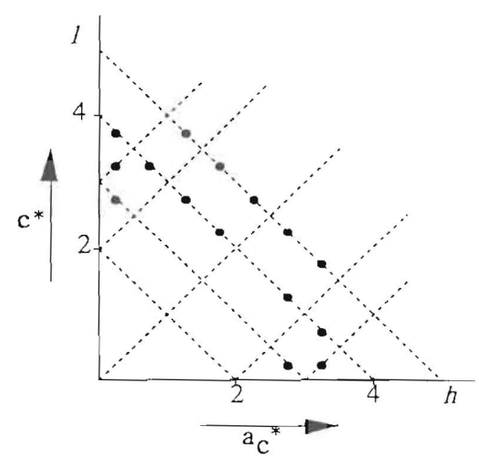

Fig. 2

2.3.10

Neutron Scattering Study on the Structure of the S=1/2 Quasi-one-dimensional Magnet $Sr_{14-x}Y_xCu_{24}O_{41}$

M. Matsuda, K. Katsumata, T. Inami[1] and S. Katano[1]

The Institute of Physical and Chemical Research (RIKEN), Wako, Saitama 351-01, Japan
[1]Japan Atomic Energy Research Institute, Tokai, Ibaraki 319-11, Japan

$Sr_{14}Cu_{24}O_{41}$, which has simple chains and ladders of copper ions[1,2], has been extensively studied since both of the building blocks show interesting ground states. The ground state of a two-leg spin ladder system is a singlet state as observed in $SrCu_2O_3$[3]. The property of the energy gap in spin ladders is interesting from the view point of quantum phenomena in a low-dimensional (between 1 and 2) Heisenberg antiferromagnet. It was theoretically predicted that the spin 1/2 Heisenberg ladder with even numbers of legs has an excitation gap and that the excitation is gapless for the spin ladder with odd numbers of legs[4]. The two-leg ladder system has also attracted many researchers since superconductivity is expected in the carrier doped spin ladder system[5,6]. Recently, Uehara *et al.* found that $Sr_{0.4}Ca_{13.6}Cu_{24}O_{41}$ shows superconductivity below 12 K under a high pressure of 3 GPa[7].

The simple chain in $Sr_{14}Cu_{24}O_{41}$ also has an interesting singlet ground state originating from a dimerization[8,9]. Surprisingly, the dimers are formed between spins which are separated by 2 and 4 times the distance between the nearest-neighbor (n.n.) copper ions in the chain. Recently, NMR studies showed that both Cu^{2+} and Cu^{3+} valence states exist in the chain[10,11]. This is probably related with the localized hole spin in the chain which is expected to couple with the copper spin to form a Zhang-Rice singlet. Then, the dimer can be expressed as <+0-> or <+000->. (+ and - represent the copper spins. 0 represents the Zhang-Rice singlet.)

When a small amount of yttrium is substituted for strontium, which is expected to reduce the number of holes, the dimerized state in the chain is changed drastically[9]. The inelastic peaks originating from the dimerized state of the chain becomes broader in energy, which implies that the dimerized state becomes unstable.

In order to clarify whether the suppression of the dimerized state is related with the structure or not, it is important to study how the structure is changed systematically with yttrium substitution for strontium.

We have started with neutron diffraction experiments on a polycrystalline sample of $Sr_{14}Cu_{24}O_{41}$. The powder samples were prepared by firing stoichiometric ratio of $SrCO_3$ (99.99%) and CuO (99.99%) at 980 ℃ for 30 h in air with intermittent regrinding. The experiments were performed at HRPD spectrometer installed at JRR-3M. The sample was mounted in a closed-cycle refrigerator.

Preliminary Rietveld analysis of the diffraction data shows that the crystal structure is consistent with that determined by McCarron *et al.* Furthermore, the structural change is negligibly small between 8 and 295 K. We are planning to perform experiments on yttrium-substituted samples. Structural studies using single crystals are also required.

References

[1] E. M. McCarron *et al.*, Mat. Res. Bull. **23**, (1988) 1355.
[2] T. Siegrist *et al.*, Mat. Res. Bull. **23**, (1988) 1429.
[3] M. Azuma *et al.*, Phys. Rev. Lett. **73**, (1994) 3463.
[4] For a review, see E. Daggoto and T. M. Rice, Science **271**, (1996) 618.
[5] T. M. Rice, S. Gopalan, and M. Sigrist, Europhys. Lett. **23**, (1993) 445.
[6] M. Sigrist, T. M. Rice, and F. C. Zheng, Phys. Rev. B **49**, (1994) 12058.
[7] M. Uehara *et al.*, J. Phys. Soc. Jpn. **65**, (1996) 2764.
[8] M. Matsuda and K. Katsumata, Phys. Rev. B **53**, (1996) 12201.
[9] M. Matsuda *et al.*, Phys. Rev. B **54**, (1996) 12199.
[10] Y. Kitaoka *et al.*, (private communication).
[11] M. Takigawa *et al.*, (submitted to Phys. Rev. B).

2.3.11

Correlation between Rhombic Distortion and Electronic Anomaly in $La_{1.775}Tb_{0.1}Sr_{0.125}CuO_4$

Y. Koike, T. Adachi, H. Sato and S. Katano[1]

Department of Applied Physics, Graduate School of Engineering, Tohoku University, Sendai 980-77
[1]Japan Atomic Energy Research Institute, Tokai, Ibaraki 319-11

Formerly, in order to clarify the correlation between the superconductivity, the electronic anomaly below about 60 K and the crystal structure at x = 1/8 in $La_{2-x}Ba_xCu0_4$, we investigated the rhombic distortion of the CuO_4 basal plane in the tetragonal low-temperature (TLT) phase in $La_{1.6-x}Nd_{0.4}Sr_xCuO_4$[1] and $La_{1.875-y}Bi_yBa_{0.125}CuO_4$[2]. We concluded that the suppression of superconductivity at x = 1/8 in $La_{2-x}Ba_xCuO_4$ was due to the electronic anomaly in cooperation with the rhombic distortion in the TLT phase, namely, due to the band-Jahn-Teller-like effect. On the other hand, Tranquada et al.[3] concluded that the electronic anomaly was due to pinning of the stripe order of holes and spins by the tilting of the CuO_4 basal plane in the TLT phase. The tilt angle is regarded as being proportional to the rhombic distortion. Here, in order to clarify whether the electronic anomaly is band-Jahn-Teller-like or due to the pinning of the stripe order of holes and spins, we have studied the temperature dependence of the rhombic distortion in $La_{1.775}Tb_{0.1}Sr_{0.125}CuO_4$ where the structural-phase-transition-temperature to the TLT phase T_{d2} is as high as 140 K and very far from the electronic-anomaly-temperature T_s = 70 K.[4,5]

The rhombic distortion of the CuO_4 basal plane was calculated as 2(d-e)/(d+e), using the oxygen positions obtained by the powder neutron diffraction and the Rietveld analysis, where d and e were two kinds of diagonal distance of the CuO_4 rhombus. The powder neutron diffraction was carried out using HRPD at JRR-3M of JAERI. The Rietveld analysis was made with reasonable space groups, $P4_2/ncm$ and Pccn.

Figure 1 shows the temperature dependence of the rhombic distortion, using the space group $P4_2/ncm$ for the Rietveld analysis. Although the error is rather large, it is found that the rhombic distortion is not so dependent on temperature and does not change drastically at T_s. The temperature dependence of the rhombic distortion, estimated using the space group Pccn for the Rietveld analysis, also exhibits the similar bahavior. Therefore, the electronic anomaly at T_s is very likely to be due to the pinning of the stripe order of holes and spins rather than to be band-Jahn-Teller-like. The following scenario appears to be reasonable. That is, the stripe order of holes and spins grows to be in a long range with decreasing temperature, so that it is pinned by the tilting of the CuO_4 basal plane at low temperatures below T_s.

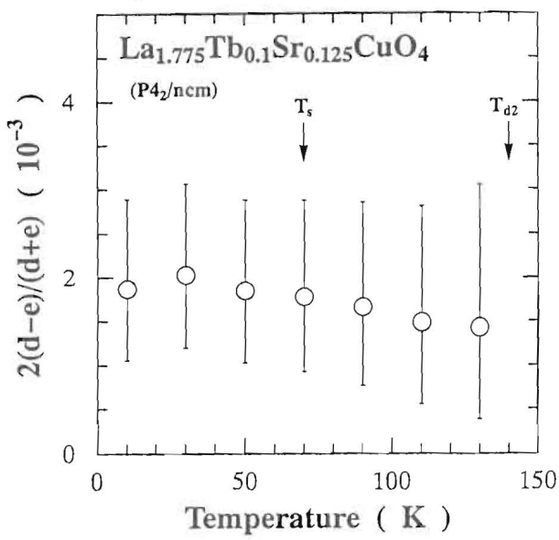

Fig. 1. Temperature dependence of the rhombic distortion 2(d-e)/(d+e) for $La_{1.775}Tb_{0.1}Sr_{0.125}CuO_4$. The space group $P4_2/ncm$ is used for the Rietveld analysis. Here, T_{d2} is the structural-phase-transition-temperature to the TLT phase. T_s is the electronic-anomaly-temperature estimated from the thermoelectric power measurements.

References

1) Y. Koike, A. Kobayashi, S. Takeuchi, S. Katano, S. Funahashi, T. Kajitani, A. Fujiwara, M. Kato, T. Noji and Y. Saito: Physica **B213&214** (1995) 84.
2) S. Takeuchi, C. Imazawa, S. Katano, M. Kato, Y. Ono, T. Kajitani and Y. Koike: Physica **C263** (1996) 298.
3) J.M. Tranquada, B.J. Sternlieb, J.D. Axe, Y. Nakamura and S. Uchida: Nature **375** (1995) 561.
4) T. Suzuki, M. Sera, T. Hanaguri and T. Fukase: Phys. Rev. **B49** (1994) 12392.
5) Y. Koike, S. Takeuchi, H. Sato, Y. Hama, M. Kato, Y. Ono and S. Katano: J. Low Temp. Phys. **105** (1996) 317.

2.4 AMORPHOUS, LIQUID AND DISORDERED MATERIALS

2.4.1 Structure of Molten YCl_3-NaCl System by Neutron Diffraction

H.Hayashi, Y.Okamoto, T.Ogawa, Y.Tsuchiya and S.Katano

Japan Atomic Energy Research Institute, Tokai, Ibaraki 319-11

The liquid structure of trivalent metal halides has been studied by the combination of experimental measurements and computer simulations[1-3]. It has been reported that molten YCl_3 has a stable octahedral structure, in which a cation is surrounded by six anions[1,2]. Saboungi et al.[1] proposed a presence of Cl^--shared medium range order in the melt from the existence of the first sharp diffraction peak(FSDP) in the neutron structure factor S(Q). The purpose of the present study is to observe the effect of the induction of NaCl into molten YCl_3 on the structure including the medium range order.

YCl_3 was purified by distillation at 1273K and NaCl was dried in vacuo at 1073K. Measurements were carried out for pure YCl_3 and YCl_3-NaCl(3:1) mixture. The samples were sealed in vacuo into a cylindrical quartz cell of 5.5mm ID, 6.9mm OD. The sample cell inserted into a vanadium holder was heated to 1023K with an electric furnace. Neutron scattering measurements were carried out with a triple-axis spectrometer TAS-1 at JRR-3. The incident neutron wave length of λ=1.00 Å was employed. The scattered neutron intensity was recorded over the range of 0.45<Q<10.15 $Å^{-1}$ ($Q=4\pi \sin\theta/\lambda$). Intervals of Q's were about 0.05 $Å^{-1}$. The scattering intensity was also measured for an empty cell.

The I/I_0 and the total radial distribution function G(r) for each sample are shown in Fig.1 and Fig.2. For pure YCl_3, FSDP is found around Q=0.9 $Å^{-1}$ in I/I_0, and peaks are observed in G(r) around 2.7 and 3.5 Å which correspond to Y-Cl and Cl-Cl correlations, as in literatures[1,2]. For mixture sample, FSDP is observed in the similar position, but the Y-Cl peak becomes less apparent and shifts to larger distance compared with pure YCl_3.

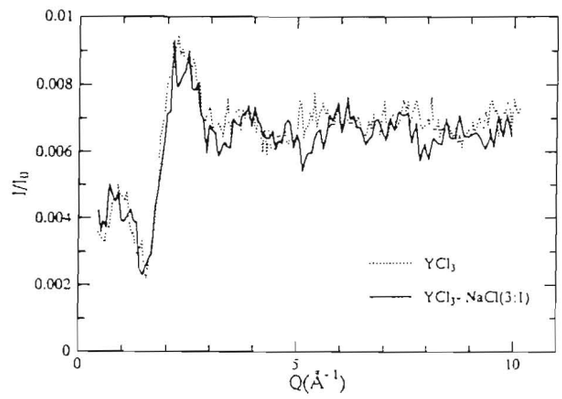

Fig.1 I/I_0 of molten YCl_3 and YCl_3-NaCl mixture

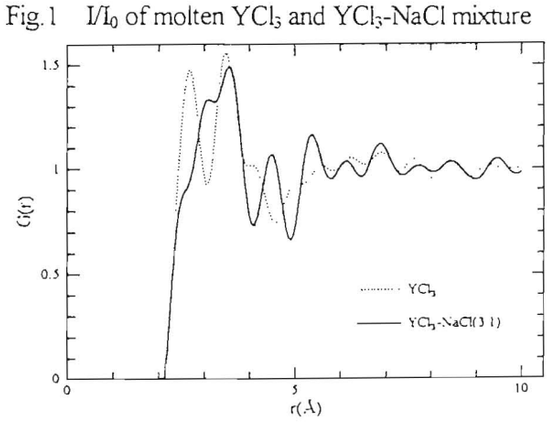

Fig.2 G(r) of molten YCl_3 and YCl_3-NaCl mixture

References

1)M.-L.Saboungi, D.L.Price, C.Scamehorn and M.P.Tosi, Europhys. Lett.,15(1991)283.

2)G.N.Papatheodorou,J.Chem.Phys.,66(1977)2893

3)Y.Okamoto, H.Hayashi and T. Ogawa, J. Non-Cryst. Solids 205-207, 139 (1996).

2.4.2
Characterization of single crystal Ni-base superalloy CMSX-4 with creep damage

K. Aizawa, H. Tomimitsu, H. Tamaki[1] and A. Yoshinari[1]

Japan Atomic Energy Research Institute, Tokai, Ibaraki, 319-11
[1]Hitachi Research Laboratory, Hitachi, Ltd., Hitachi, Ibaraki, 317

The single crystal Ni-base superalloys have developed for gas turbine blades of power plants as a next generation material, which can operate higher temperature to achieve high efficiency. The characterization of microstructure of superalloy is very important, because the mechanical properties are governed by the morphology of γ' phase precipitation in a γ phase matrix. Therefore, it is very interested in a non-destructive evaluation of the expected life of operated blades for practical purpose. In order to check the possibility of non-destructive test of the expected life of operated blades by observation of morphology change of superalloy, we have applied small-angle neutron scattering (SANS) experiments to the standard CMSX-4 superalloy with creep damage as a model case.

Because a detection of morphology change of sample between 10% and 30% creep interruption rate for rupture time is necessary for prediction of the expected life practically, we selected as heat treatment and those creep condition. Samples were loaded tensile stress with 14kgf/mm^2 at 1313K after standard heat treatment. The stress direction was parallel to <001> direction of a sample. Samples were cut into 30mm×30mm×2mm[1]. SANS measurements were carried out by SANS-J instrument with the q-range of 2×10^{-2}-0.25nm^{-1} and PNO instrument with the q-range of 2×10^{-4}-6×10^{-2}nm^{-1} at JRR-3M. Incident neutron beams were parallel to <100> direction of a sample. In SANS-J experiments, two-dimensional scattering pattern showed fourfold symmetry due to aligned cuboidal γ' phase precipitation in the case of as heat treatment sample. On the other hand, we observed 2nd peak from lamella structure which was formed by aggregation of precipitation into perpendicular direction of stress in the cases of stressed samples. Figure 1(a) shows the PNO results in which q is perpendicular to stress direction, while q is parallel to stress direction in fig. (b). In the case of as heat treatment sample, we observed 1st maximum of the cuboidal scattering function with interparticle interference by aligned cuboidal γ' phase precipitation. The 1st peak of the lamella structure is clearly shown in the cases of stressed samples. The average distance between γ and γ' phases, which is obtained from a hollow position around q=0.01nm^{-1} of cuboidal scattering function or 1st peak position of lamella structure, as a function of creep rate for rupture time is shown in fig. 2. The SANS results are good agreement with SEM observation. We conclude that SANS may be applied to non-destructive test for turbine blades.

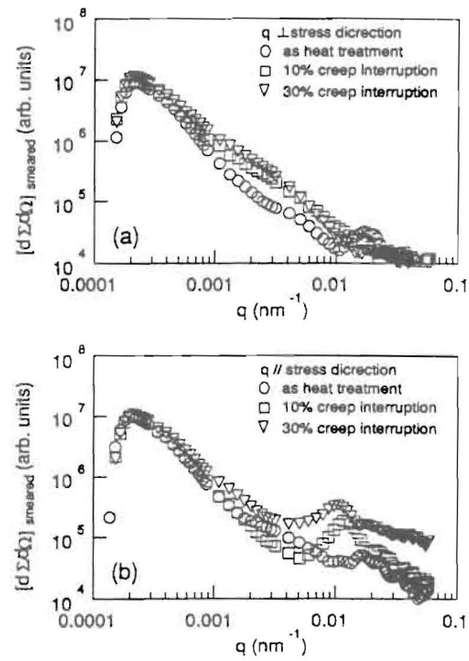

Fig. 1 SANS intensities from CMSX-4. (a) q is perpendicular to stress direction. (b) q is parallel to stress direction.

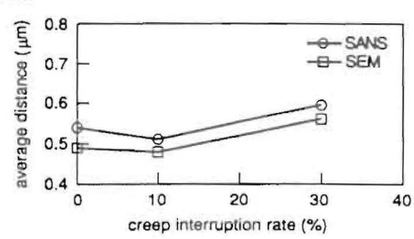

Fig. 2 Average distance between γ and γ' phases as a function of creep interruption rate of rupture time.

2.4.3

Characterization of as-deposited pyrolytic carbon by small-angle neutron scattering

K. Aizawa, H. Tomimitsu and T. Iwata
Japan Atomic Energy Research Institute, Tokai, Ibaraki, 319-11

The carbon materials show various kinds of physical and mechanical properties which depend on production conditions. Therefore, it is important to characterize the structure to understand those properties. Usually those contain defects such as non-carbonization region, lattice distortion, pore and residue. Frequently, the scale of imperfection ranges up to μm. The pyrolytic carbon is one of the carbon materials. That grows on substrate by gaseous carbonization and is not followed by a higher temperature heat treatment to align crystallite. The growth direction, i.e., deposition direction is roughly equal to c-axis of graphite. Though as-deposited pyrolytic carbon has nearly identical graphite density, the distortion of the crystallite is strong. In order to obtain structural information of the as-deposited pyrolytic carbon we have performed small-angle neutron scattering (SANS) experiments using a double crystal diffractometer (DCD) and a conventional pin-hole SANS instrument (SANS-J) at JRR3-M. Sample was deposited on substrate at 1850°C. The density of sample is 2.2g/cm^3. This value is 4.3% less than that of ideal graphite. From neutron diffraction, the c-axis length is 0.681nm which is 1.7% longer than that of ideal graphite and the mosaic spread is about 46.3 degree.

Double crystal diffractometers for SANS experiments are widely used for investigating the structure in a μm range. We installed a DCD in the precise neutron optics (PNO) instrument at the 3G beam hole in JRR-3M. The DCD is set on a vibration isolated table in a temperature controlled chamber. We tested Si perfect single crystals with (1,-1) setting[1] firstly, but now we use channel-cut Si perfect single crystals with (5,-5) setting at λ=0.25nm. Their reflection surfaces are parallel to (111) plane. The signal to noise ratio of the DCD is 3.9×10^4. The peak intensity of a 2nd Si rocking curve without sample is about 1000cps.

Hereafter, we call the deposited direction c-axis for simplicity. The SANS-J experiment revealed that two-dimensional scattering pattern is anisotropic in the case of c-axis being perpendicular to incident neutrons, while that is isotropic in the case of c-axis being parallel to incident neutrons. Figure 1 shows SANS intensity from sample. We conclude that there are two kinds of disk-like pores which align c-axis. From a q^{-4} dependence (Porod law) in a very low-q region, one is μm order pore. Another is small pore with average size of 7.26nm radius and 1.29nm thickness obtained by Guinier plots using around q=0.02 data. Deviation from q^{-4} dependence (the q^{-3} dependence) is seen in a high-q-region. This is due to inhomogeneity of matrix. It seems that the $q^{-2.5}$ dependence in the middle q-range is interparticle scattering of small pores.

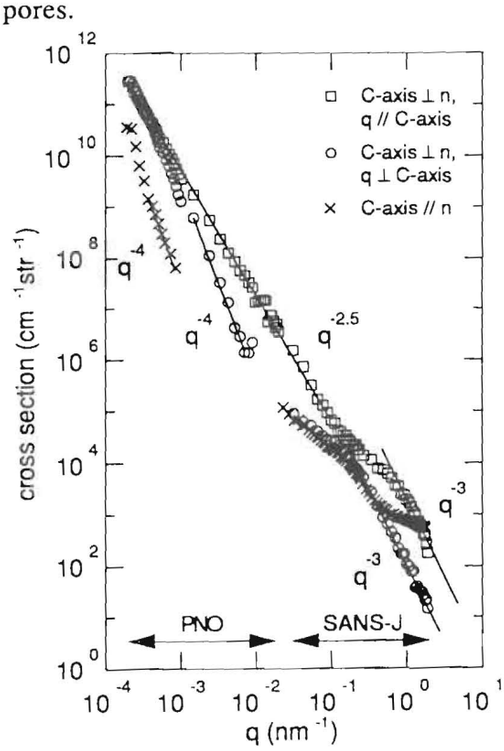

Fig. 1 Absolute SANS cross section from as-deposited pyrolytic carbon. □ : c-axis is perpendicular to incident neutrons and q is parallel to c-axis. ○ : c-axis is perpendicular to incident neutrons and q is perpendicular to c-axis. × : c-axis is parallel to incident neutrons.

References

(1) K. Aizawa and H. Tomimitsu, Physica B **213&214** (1995) 884

2.4.4 SANS Study on Fe-Cu-Nb-Si-B and Fe-Zr-B-(Cu) Nanocrystalline Alloys

M. Ohnuma, K.Hono, H.Onodera and J. Suzuki[1]

National Research Institute for Metals, Tsukuba, Ibaraki 305, Japan
[1]Japan Atomic Energy Research Institute, Tokai, Ibaraki 319-11, Japan

Recently, many types of nanocrystalline alloys which exhibit improved magnetic properties were reported. For understanding mechanisms of micro-structural evolution in these alloys, it is important to obtain information on partitioning and segregation of alloying elements during crystallization processes. In this study, we have employed small-angle neutron scattering (SANS) and atom probe field ion microscope (APFIM) techniques for characterizing microstructures during nanocrystallization processes in Fe(-Cu-Nb)-Si-B and Fe-Zr-B(-Cu) alloys.

Previous APFIM work on Fe-Zr-B(-Cu) nanocrystalline alloys[1)] reported that zirconium atoms segregate at the interface between bcc crystal and amorphous matrix. In our SANS measurement of these alloys, both nuclear and magnetic scattering shows a straight line with gradient of -3. For example, figure 1 shows SANS profiles for $Fe_{90}Zr_7B_3$ alloy annealed at 898K for 30min. Though the scattering from large grain shows the straight line with gradient of -4, another straight line with gradient of -3 can be observed in high q region. This is believed to be attribute to nano-size particle. A peak due to interparticle interference can be observed near 0.4 nm^{-1} in both nuclear and magnetic component. For Fe-Cu-Nb-Si-B alloys, we have reported[2)] that the magnetic scattering profiles in log-log plot have shown a straight line whose gradient is -3 and this asymptotic behavior originates from the steep change in local magnetization contrast between bcc and amorphous matrix near interface. Thus we interpret the gradient of -3 as an indication of segregation layer around the bcc/amorphous interface. In the case of Fe-Cu-Nb-Si-B alloys, nuclear scattering shows the straight line with gradient of -2. Spherical shell is one of the structure whose asymptotic form $I(q) \sim q^{-2}$. Because this structure also has a steep change in scattering density, the asymptotic behavior of nuclear scattering also corresponds to the segregation near the interface. In a previous work[2)], we reported that SANS scattering profiles of nuclear and magnetic components of a Fe-Cu-Si-B alloy without niobium follows Porod law, $I(q) \sim q^{-4}$. Thus, we speculate that the steep change of the scattering density near the interface is mainly attributed to segregation of niobium.

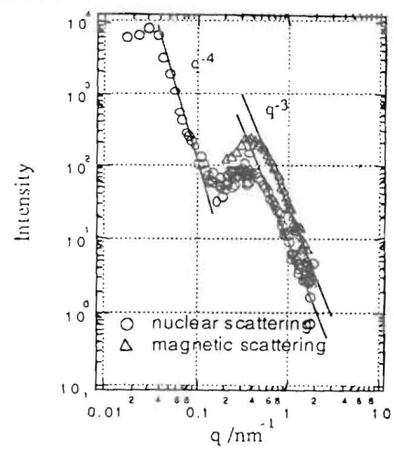

Fig.1 SANS profiles for $Fe_{90}Zr_7B_3$ alloy annealed at 898K for 30min measureed in the magnetic field of 1.16T.

In order to confirm this, atom probe concentration depth profiles were obtained from the same specimens as those measured with the SANS technique. As a result, it is confirmed that niobium atoms are segregated at the bcc/amorphous interfaces in the sample annealed at 723K for 10min[3)]. From these results we conclude that grain growth of Fe(-Cu-Nb)-Si-B and Fe-Zr-B nanocrystalline alloys are controlled by diffusion of slowly diffusing atoms such as Nb and Zr.

References

[1] Y.Zhang, K.Hono, A.Inoue, A.Makino and T.Sakurai: Acta mater., 44 (1996), 1497
[2] M.Ohnuma, J.Suzuki, S.Funahashi, T.Ishigaki, H.Kuwano and Y.Hamaguchi: Matelials Trans., JIM., 36 (1995), 918
[3] M.Ohnuma, K.Hono, J.Suzuki and H.Onodera: Mta. Sci. Eng. A, to be published.

2.4.5 Correlation between medium range order and ionic conduction in superionic conducting glasses

H. Takahashi[1], T. Sakuma[2], Y. Nakamura[2], Y. Shimojo[3] and Y. Ishii[3]

[1]Faculty of Engineering, Ibaraki University, Hitachi 316 Japan
[2]Faculty of Science, Ibaraki University, Mito 310, Japan
[3]Japan Atomic Energy Research Institute, Tokai 311-19, Japan

Several structure models for AgI-containing superionic conducting glasses are proposed to comprehend the mechanism of high ionic conduction on the basis of the structural, thermal and transport properties. Typical model for these glass structure is the cluster model, which is originated from the observation of first sharp diffraction peak (FSDP) of structure factor at about 0.8 $Å^{-1}$. AgI-Ag_2O-V_2O_5 system is used as a model superionic conducting glasses for verification of the cluster model from following reason. First, the coherent scattering cross section for neutron of V ion is very small. So the correlation among Ag, I and O ions mainly contribute to the neutron diffraction. Second, AgI-Ag_2O-V_2O_5 system vitrifies from 0 to 67 mol% of AgI with $(Ag_2O)_{0.6}(V_2O_5)_{0.4}$ composition. X-ray and neutron diffraction experiments are performed along this composition line.

Figure 1 shows that FSDP around 0.8 $Å^{-1}$ can not be observed both X-ray and neutron diffraction in all the composition examined. It is reported that the visibility of the inhomogeneous structure, such as AgI cluster depends on the defferences Δ between the neutron scattering length densities for each phase present.[1] The value of Δ is 3.2 in the present system. It is considered to have enough magnitude to detect FSDP. These results indicate that the existence of the definite size of AgI clusters in the glass network is questionable. It is considered that the observed FSDP in other superionic conducting glasses is originated from the density fluctuation of the supporting glass network. Recently, we observed the difference in the ionic conduction behaviour between low- and high-AgI concentration region in this system. Therefore there is a possibility of the formation of some kind of AgI sub-structure, but not cluster, in high-AgI region. The investigation on the structural features in $3Ag_2O$-$2V_2O_5$ glass by neutron diffraction is in progress. It is expected to obtain information about AgI sub-structure and to clarify the conduction mechanism of superionic conducting glasses.

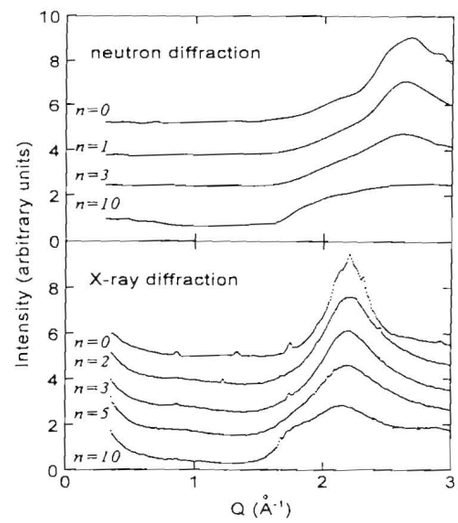

Fig. 1 X-ray and neutron diffraction profiles of the composition nAgI-$3Ag_2O$-$2V_2O_5$ glasses below 3 $Å^{-1}$

References

1) C. Rousselot, J. P. Malugani, M. Tachez, P. Chieux, A. J. Pappin and M. D. Ingram: Solid State Ionics **78** (1995) 211-221.

2.5 POLYMERS

2.5.1

Neutron Scattering Study on Non-Gaussian behavior for Highly Oriented Copolyester Glass.

Satoshi Koizumi

Japan Atomic Energy Research Institute, Tokai, Ibaraki 319-11, Japan.

Introduction.

In a previous paper[1], we have recently studied the rotational motion of aromatic groups, which constitute a random copolyester (vectra), over a wide range of temperature from glassy to liquid crystalline phases. Vectra gives rise to the nematic phase transition at T_m=558K from the semi-crystalline phase, i.e., a mixture of crystalline and amorphous phases (T_g=393K). Because of a rigid backbone, vectra forms spatially anisotropic glassy phase below T_g, which becomes advantage for understanding the glass structural relaxation under a complicated balance of intermolecular interactions. In this report, we report the anharmonic behavior of the local relaxation of glassy vectra, which is also spatially anisotropic.

Experimental.

Vectra is a highly oriented random copolyester of p-hydroxybenzoic acid (HBA) and 2-hydroxy-6-naphthoic acid (HNA) with a faction of 73/27 (mol/mol). The structural heterogeneity induced by the minor component of HNA is crucial to avoid the perfect crystallization. The degree of crystallinity has been estimated by X-ray scattering as a function of temperature[2].

The neutron scattering measurements were performed in a wide range of temperature from far above the glass transition temperature Tg (=393K) to far below Tg, with the triple axis spectrometer (TAS-2) at Japan Atomic Energy Research Institute (JAERI) in Tokai, Japan. The pyloritic graphite PG(002) provided incident neutrons of wavelength λ=1.43 Å.

Figure 1 shows a schematic diagram of the experimental system for neutron scattering. The rigid molecular axis for vectra (*MA*) is highly oriented along the direction of ϕ=0°. The local chain orientation fluctuates around ϕ=0°, which is denoted with an angle of δ°. We have chosen tow optical geometries for neutron scattering measurements, in which the scattering vectors $\tilde{q}$ ($|\tilde{q}|=4\pi/\lambda \sin(\theta/2)$) are normal ($q_\perp$) and parallel ($q_{//}$) to the orientational direction of ϕ=0°.

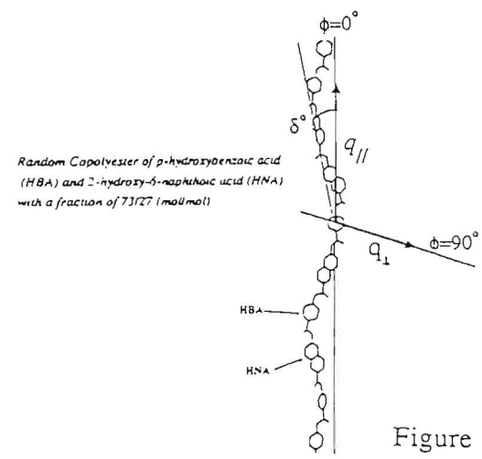

Figure 1

Results and Discussion.

We carried out the elastic neutron scattering measurements observing over a wide q-range from 0.5 up to 6.5 A^{-1}, in which the energy analyzer PG (002) was set to obtain the elastic scattering component determined by its energy resolution of 2.8 mev. The elastic scattering thus obtained $S(q,w=0)$ is described as follows[3],

$$S(q,w=0) \sim S_{el}(q)\, DW[T]. \qquad (1)$$

The first term $S_{el}(q)$ in *eq.(1)* is composed of both elastic coherent and elastic incoherent scattering cross sections. Especially in a region of large q-vector, the coherent contribution becomes negligible. The second term $DW[T]$ is the Debye Waller factor, given as follows,

$$DW[T] \sim \exp[-\alpha q^2 + 1/2\, A\alpha^2 q^4] \qquad (2)$$

where α is the mean square displacement for hydrogen's motion and A is so-called non-Gaussian parameter. The physical meaning for non-Gaussian parameter has been discussed elsewhere[4].

In order to obtain the Debye-Waller factor and these two characteristic parameters, the observed scattering at each temperature was normalize by that obtained at 8K. This analysis is based upon an assumption that the coherent structure factor dose not change in glassy phase. Figure 2 shows the typical results at T=240 K, plotted as a function of q^{-2}. The broken lines in Fig.2 are curve-fitted lines to results with *eq.(2)*. In the case of *q-vector* parallel to *MA*, the Debye-Waller factor decreases linealy in Fig.2 so that the non-Gaussian parameter in *eq.(2)* is negligible. On the other hand, in the case of *q-vector* normal to *MA*, the non-Gaussian parameter is crucial to reproduce the non-linear q-behavior as observed in Fig.2.

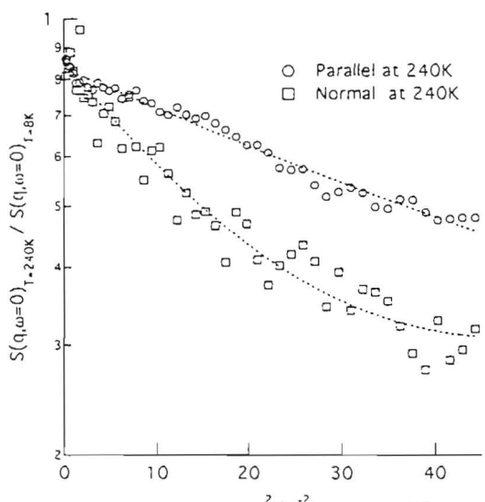

Figure 2

Figure 3 summarizes the temperature dependence of mean square displacement α and non-Gaussian parameter A. In both cases of *q-vector* parallel ($q_{//}$) and normal ($q_{\perp}$) to *MA*, the mean square displacement α increases linealy as a function of temperature. For a overwhole range of temperature, the optical geometry of $q_{\perp}$ has larger displacement α than that for $q_{//}$. The non-Gaussian parameter A for $q_{\perp}$ strongly depends on temperature. As decreasing temperature into the glassy phase, the non-Gaussian parameters obtained for the $q_{\perp}$ become larger, while those for $q_{//}$ are negligible and independent of temperature.

Kanaya et al. have studied the non-Gaussian parameters for several polymer glass systems, which are all random coils, by using the triple axis spectrometer[5]. They extended discussions to a relationship between non-Gaussian parameter and fragility. According to their results, as increasing fragility which means weak glass, the non-Gaussian parameter becomes small.

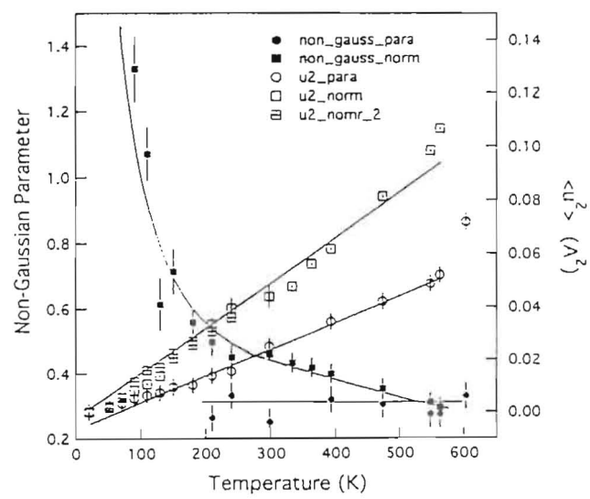

Figure 3

References

[1] S.Koizumi *J. Chem. Phys.* 1997 in press.

[2] S.Koizumi, K. Saijo and T. Hashimoto in preparation.

[3] A.Rhmann *Phys. Rev.* **136**, A405 (1964).

[4] L.J Lewis and G.Wahnström *Solid State. Commun.* **86**, 295 (1993).

[5] T.Kanaya et al. *Proceedings for YKIS'96* in press.

2.5.2

Development of Dynamic Data Acquisition System (DDAS) for Small-Angle Neutron Scattering

S. Suehiro, S. Koizumi[1], O. Makino and T. Hashimoto

Graduate School of Engineering, Kyoto University, Sakyo-ku, Kyoto 606-01
[1]Japan Atomic Energy Research Institute, Tokai, Ibaraki 319-11

Pattern formation observed in soft matter has attracted much attention in recent years in the field of non-linear, non-equilibrium statistical physics, owing to its wide variety of pattern forming characteristics, resulting in various patterns in microscopic, mesoscopic, and macroscopic length scales.

Small-angle neutron scattering (SANS) is a unique technique for such soft matter to provide structural information otherwise never be obtained, e.g., equilibrium single chain dimensions of a polymer in bulk, using deuterium labeling. Furthermore, time-sliced SANS studies, which is characteristic to monitor scattered neutrons for a given time intervals, have produced excellent results to elucidate the initial stage of spinodal decomposition observed for binary polymer blends, in which concentration fluctuations frozen at a non-equilibrium initial state evolved monotonously toward an equilibrium final state.

In order to extend an applicable field of SANS to wider non-equilibrium phenomena, we are developing ***Dynamic Data Acquisition System (DDAS)***. This data acquisition system is conceived for investigating non-equilibrium state of a sample specimen and enables SANS to approach dynamic processes, i.e., rhythmic formation, annihilation and deformation of patterns or internal structures under various external fields such as mechanical, thermal, or electrical fields.

Two data acquisition systems have been built and tested at SANS-J in Tokai. The first one was a prototype system; a personal-computer-based system consisting of host and slave computers. This system was designed only for phase-correlated measurements.

The second system (see Fig. 1) has been further developed to be composed of a unix workstation (Sun SPARC station), which serves as a host computer, a VME-bus CPU module and a custom interface for data acquisition. The histogramming for two dimensional data is performed by the CPU module employing on-board memory as histogram memory. The histogram is asynchronously read by the host computer through a bus adaptor, enabling real-time monitoring of data acquisition. The custom interface is specially designed to have two sets of time-correlating function modules, i.e., (i) an interface for the phase-correlation with a oscillatory external field, and (ii) a timing counter with a prescaler for an accurate synchronization to repetitive phenomena of uniform or of non-uniform intervals.

By using a function (i) for phase-correlated SANS, the preliminary study was carried out with SANS-J spectrometer having a two-dimensional PSPC (see report p. 65). The oscillatory external field of sinusoidal shear strain was imposed on a semidilute polymer solution by a servo-controlled hydraulic deformation device. The shear field induced anisotropic concentration fluctuation in a small angle region.

The function (ii), i.e., an accurate synchronization, is considered to have still wider applications. The potential applications of function (ii) are (1) an observation of self-oscillating open system induced by chemical reactions and (2) a time of flight method for inelastic measurements.

Dynamic Data Acquisition System (DDAS) for SANS-J
New Approach to Non-Equilibrium Complex System

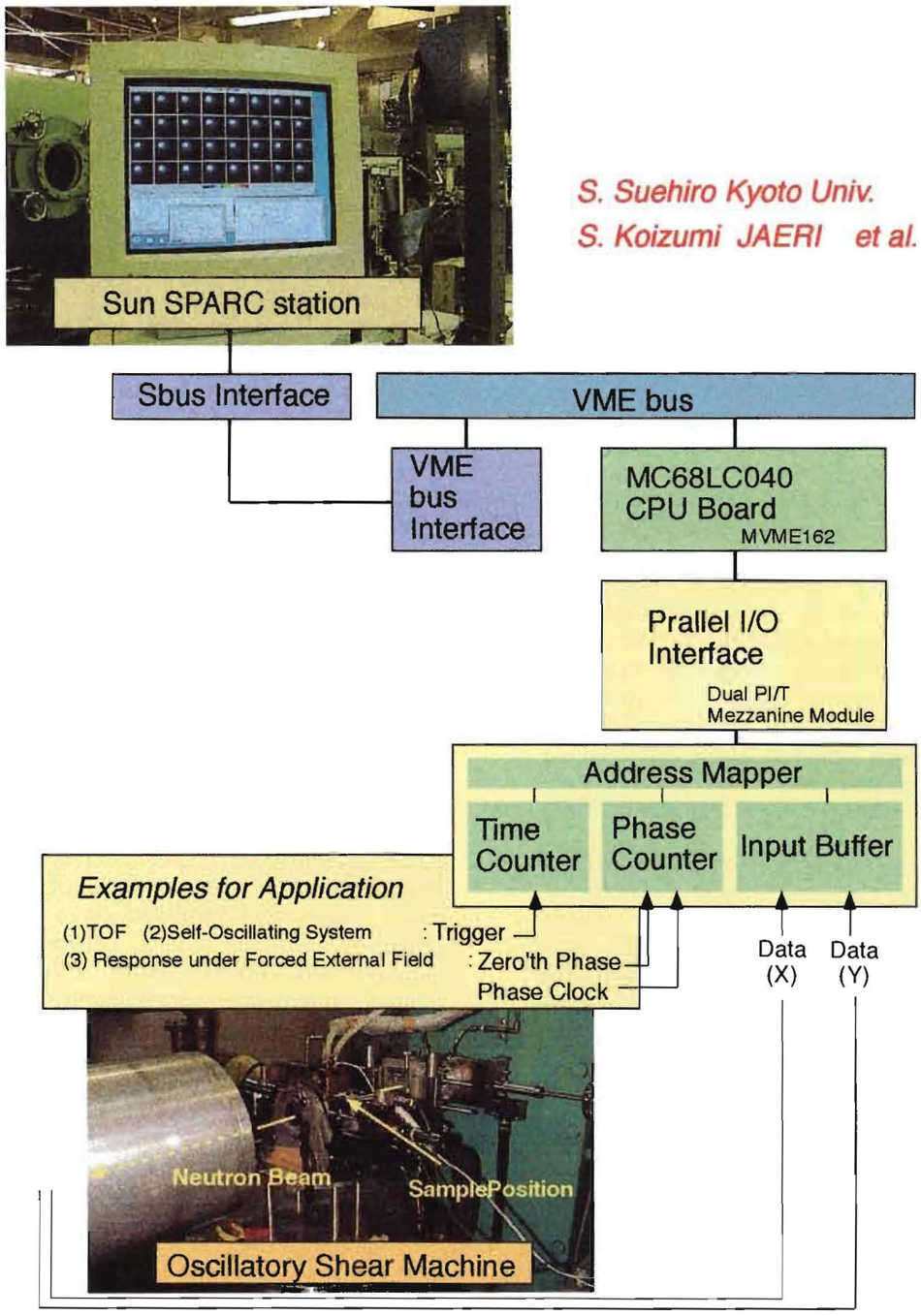

Figure 1

2.5.3

Phase-Resolved Neutron Scattering Study of Semidilute Polymer Solution under Shear Flow

S. Saito, S. Suehiro, S. Koizumi[1], O. Makino, G. Shin and T. Hashimoto

Department of Polymer Chemistry, Graduate School of Engineering, Kyoto University
Yoshida-Honmachi, Sakyo-ku, Kyoto 606-01, Japan

[1]Japan Atomic Energy Research Institute, Tokai 319-11, Ibaraki, Japan

It has been reported that a shear flow, imposed on a semidilute polymer solution in single phase, enhances concentration fluctuations toward phase separation and therefore makes it turbid. This phenomenon is so-called *"shear-induced phase separation"* and has been studied deeply by means of light scattering, optical microscopy and rheology measurements. Here, we report our extensional investigation for such systems under oscillatory shear flow, which is coupled with ***phase-resolved*** small-angle neutron scattering (SANS).

The phase-resolved SANS mesurements were operated by ***the dynamic data acquisition system (DDAS)*** at SANS-J , JAERI, which was newly developed (see report p. 63). *A* sandwich type cell, operated by a servo-controlled hydraulic deformation device, imposes a sinusoidal shear strain on a semidilute polymer solution. The incident neutron beam was passing through this cell along a direction normal to the velocity gradient direction. The phase of oscillatory shear flow is directly coupled with *DDAS* so that we are able to investigate a correlation between oscillatory shear flow and enhanced concentration fluctuations.

In this study, we employed a semidilute solution of high molecular weight deuterated polystyrene dissolved in dioctyl phthalate (8.0wt.%). Recently, we have revealed for this system that shear-induced phase separation occurs not only under a steady shear flow, but also under a oscillatory shear flow, and the occurrence in the latter condition strongly depends on the strain amplitude(γ_0) and the angular frequency(ω). Here, we fixed the strain amplitude at 4.6, and observed the strain phase dependence of a 2D-SANS pattern.

Figure 1 shows the SANS patterns at w=12.27[rad/s], where f represents the strain phase and f=0 means the strain equals to zero. Each scattering pattern is anisotropic at low q and has some kind of double-winged enhancement of concentration fluctuations (*butterfly*) along the flow direction. This butterfly is the scattering pattern indigenous to shear-induced phase separation.

It should be pointed out that the butterfly pattern observed at low q strongly depends on the strain phase. When f is approaching to p/2 and the strain reaches to maximum, the shape of the butterfly shrinks along the flow direction. This observation implies that the growth of shear-induced structures is synchronized with the strain.

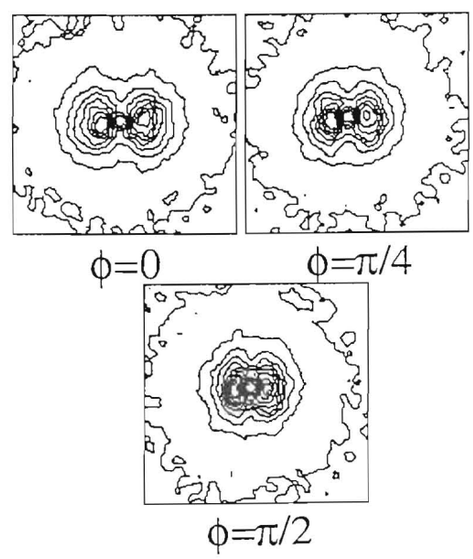

Fig.1 Strain phase dependence of a scattering pattern of d-PS/DOP 8.0wt.% under oscillatory shear flow.

2.5.4

Anomalous Neutron Scattering Behaviors of Polymer Blends near the Glass Transition Temperature

Hiroyuki Takeno, Satoshi Koizumi[1], Hirokazu Hasegawa and Takeji Hashimoto

Department of Polymer Chemistry, Graduate School of Engineering, Kyoto University, Kyoto 606-01
[1]Japan Atomic Energy Research Institute, Tokai, Ibaragi, 319-11

Numerous researchers made great contributions to the studies on the thermal concentration fluctuations (TCF) in the single phase state of polymer blends by using small-angle neutron scattering (SANS). The behavior of the TCF has been verified to obey the de Gennes formula based upon random phase approximation (RPA). However, most of the experimental verifications have been carried out at high temperatures where constituent polymers are free from vitrification.

Recent years, we have investigated the influence of TCF in the single phase state of polymer blends on vitrification of polymers. As the result, while SANS of a deuterated polystyrene (DPS) /poly(vinyl methyl ether) (PVME) blend was well described by the de Gennes formula at the high temperatures far above the glass transition temperature T_g of the blend, it showed an anomalous behavior near the T_g, i.e., the SANS was more suppressed than that expected from the de Gennes formula in the small q region. On the other hand, SANS of deuterated polybutadiene (DPB) /protonated polybutadiene (HPB, hereafter it is designated as HPB-v16) and DPB/polyisoprene (PI) blends did not show any anomaly even near the T_g of their blends. While DPS/PVME has a large difference (ΔT_g=127 K) in the T_g of each component, each component of DPB/HPB-v16 and DPB/PI has almost the same T_g (ΔT_g=4 and 29 K, respectively).

In this work, we studied the SANS for another DPB/HPB which has a large difference (ΔT_g=64 K) in the T_g of each component. (PB has different microstructures in monomer units and therefore, its T_g changes by the fraction of each microstructures included in PB.) While the DPB used in this study is the same as that in the previous study, the HPB is different from HPB-v16 and has 85.7 % 1,2, 2.4 % cis-1,4 and 11.9 % trans-1,4 linkages. Hereafter, we designate the HPB as HPB-v85.

In the small-q region (qR_g<1), the scattering behavior in the single phase state of polymer blends obeys the Ornstein-Zernike representation [$S(q)^{-1} = S(0)^{-1} + Aq^2$], where R_g is the mean square radius of gyration of molecule. Fig. 1 shows a plot of $S(0)^{-1}$ estimated from the Ornstein-Zernike plot vs. reciprocal temperature T^{-1} for DPB/HPB-v85=50.1/49.9 wt.%/wt.%. At high temperatures, $S(0)^{-1}$ linearly increases with T^{-1}. Near the T_g of the blend, $S(0)^{-1}$ deviates upwards from the linearity, indicating that S(0) is more suppressed than that predicted from the linear relation at high temperatures. Below the T_g, $S(0)^{-1}$ becomes almost constant because of vitrification of polymers. This behavior near the T_g is different from that for DPB/HPB-v16 and similar to that for DPS/PVME. Therefore, this result strongly suggests that suppression of the scattering intensity near the T_g is unique for the blends whose each component has largely different T_g.

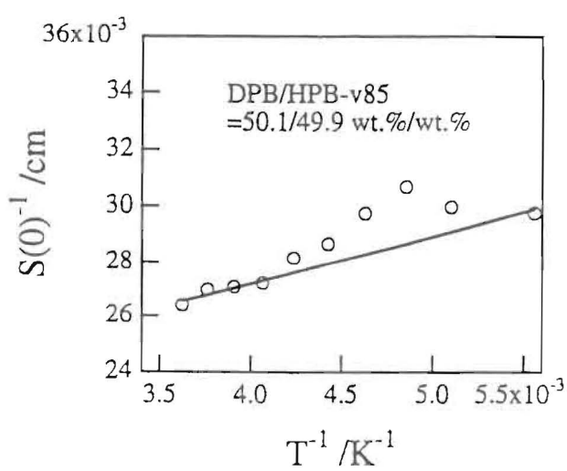

Fig. 1 $S(0)^{-1}$ vs. T^{-1} for DPB/HPB-v85.

2.5.5 Small Angle Neutron Scattering of N-isopropylacrylamide Gel

T.Okamoto[1], Y.Hirokawa[1], K.Kimishima[1], H.Jinnai[1], S.Koizumi[2] and T.Hashimoto[1,3]

[1]Hashimoto Polymer Phasing Project, ERATO, JST, 15 Morimoto-cho, Shimogamo Sakyo-ku, Kyoto 606

[2]Japn Atomic Energy Reserch Institute, Tokai, Ibaraki 319-11

[3]Graduate School of Engineering, Kyoto University, Kyoto 606-1

Gel is an interesting material consisting of a three-dimensionally cross-linked polymer network and a fluid. The network structure influenced by the gelation conditions affect the characteristics of the gels such as optical, mechanical, and swelling properties. Many studies on the gel have been made so far, however, there are not so many reports relating to the internal structures and inhomogeneities of the gel. In order to understand the characteristics of the gel, it is important to study the internal structures.

The gel used in this work is N-isopropylacrylamide gel. The gel samples were prepared at 25°C, 32°C, and 38°C. The gel prepared at 25°C which was lower than the cloud point of the network polymer (32.2°C) was transparent. The gels prepared at 32°C and 38°C were opaque. The observation of the internal structures of the samples was carried out by means of small angle neutron scattering.

Figure 1 shows the double logarithmic plot of the scattered intensity as a function of the wave number q. The slopes in the q range from $0.03nm^{-1}$ to $0.07nm^{-1}$ are expressed by a q^{-4} dependence for all samples. This corresponds to the formation of a sharp interface (Porod's law), which may be due to the presence of the microgels.

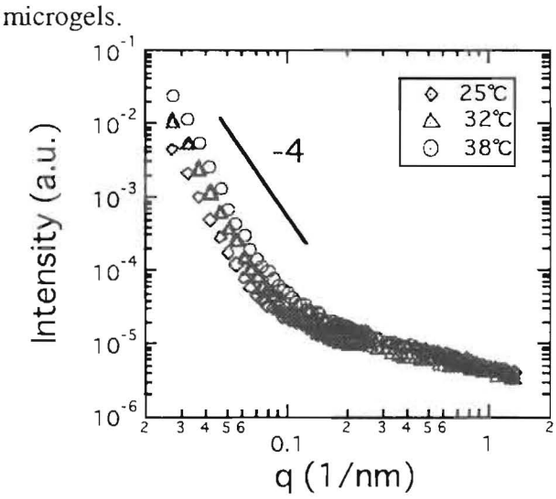

Fig.1 Double logarithmic plot of the scattered intensity as a function of q.

References

1) M.Shibayama and T.Tanaka, Advances in Polymer Science, 109, 1-62(1993).

2) Y.Hirokawa and T.Tanaka, AIP Conference Proceedings No.107, Physics and Chemistry of Porous Media edited by D.L. Johonson and P.N. Sen, 203-208(1984).

3) Y.Hirokawa and T.Tanaka, J. Chem. Phys., 81(12), 6379-6380(1984).

2.5.6

Isothermal Crystallization Mechanism of Isotactic Polystyrene Viewed from Molecular Level

Kohji Tashiro[1], Sono Sasaki[1], Naomi Gose[1] and Satoshi Koizumi[2]

[1] Graduate School of Science, Osaka University, Toyonaka. Osaka 560, Japan
[2] Japan Atomic Energy Research Institute, Tokai, Ibaraki 319-11, Japan

In a series of papers [1, 2] we have investigated the structural change in the crystallization process of polyethylene sample through the measurements of time-resolved FTIR, SAXS and SANS and found that the conformationally-disordered trans form appears transiently on the way of cooling from the random coil of the melt to the regular trans conformation of the orthorhombic crystalline phase, during which the stacked lamellar structure is formed. We advance our study to the other kinds of crystalline polymer such as isotactic polystyrene (is-PS), the molecular chains of which have a helical conformation and are packed in the unit cell in a statistically random fashion as for the upward and downward directions of the chains. This situation is different from the case of orthorhombic polyethylene. In such a meaning, therefore, it is very important to clarify the aggregation mechanism of it-PS chains which should occur during the crystallization process from the melt. This type of study requires us to clarify the change of size of the whole molecular chain or the radius of gyration Rg in the process of crystallization. This is because the Rg is one of the important measures for the structural change of the whole chain and makes us allow to speculate the organization process of the random coil to the crystalline state. In the present paper, we will report the temperature dependence of the Rg of it-PS in the crystallization process from the melt. Although there have been published many numbers of papers concerning the evaluation of Rg of PS, most of them have used the samples of perdeuterated (or hydrogeneous) atactic or isotactic PS chains embedded in atactic PS matrix. In the present study we have used the hydrogeneous it-PS (it-PS-h) embedded in the perdeuterated it-PS (it-PS-d) matrix in order to investigate the crystallization process of the natural aggregation state of the configurationally-equivalent chains.

The it-PS-h of the weight-averaged molecular weight of 10^6 g/mol was mixed with the it-PS-d of 6.5×10^5 g/mol at the concentration of ca. 3 wt%. The sample was set into the high-temperature cell installed in the SANS-J equipment of the JAERI. The temperature dependence of the SANS data was measured at the various temperatures from 250°C to 40°C. After the correction for the sample thickness, transmittance and background, the absolute value of the differential cross-section was evaluated finally by subtracting the contribution of the void scattering which was estimated from the scattering data of the pure it-PS-d sample measured at the same temperatures. The Rg was evaluated by plotting the inverse of the differential cross-section against q^2 (Zimm's plot) where q was a wave vector. As shown in Figure 1, the Rg was evaluated to be ca. 95 Å in the whole region of the measurement temperature covering both the molten state and the crystalline state. That is to say, the molecular chain is crystallized with the averaged expansion of the total chain kept almost unchanged. This information will become important when we discuss the details of the conformation change of chains in the isothermal crystallization process from the melt.

References (1) K. Tashiro, Acta Polymerica, 46, 100 (1995). (2) K. Tashiro et al., Macromolecules, to be published.

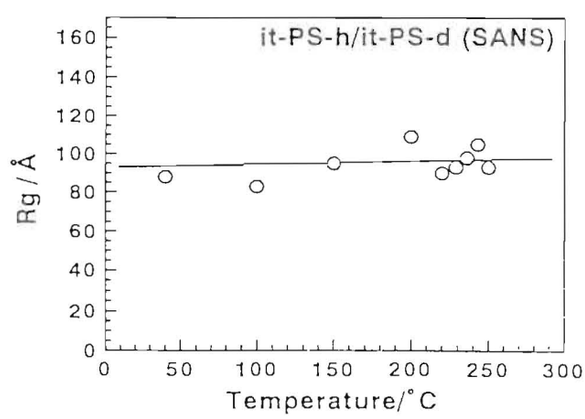

Figure 1 Temperature dependence of Rg of it-Ps

2.5.7 Small-Angle Neutron Scattering Study of Star-Shaped Polystyrenes Having One Deutrium-Labeled Arm in Solution

A. Takano, A. Fukushi, Y. Isono, S. Koizumi[1] and Y. Morii[1]

Department of Chemistry, Nagaoka University of Technology, Nagaoka, Niigata 940-21

[1] Neutron Scattering Laboratory, Japan Atomic Energy Research Institute, Tokai, Ibaraki 319-11

A star-shaped polymer has a high segment density in the vicinity of center point. Therfore it is estimated that the arm chains of star polymers are more expanded than the chain of linear polymers by the exclueded volume effects. In addition, the expansion increases with increasing number of arms. In order to investigate the chain conformations, it is useful to measure the small-angle neutron scattering of a deutrium-labeled arm in a star-shaped polymer.[1)]

In this study, we have attempted to synthesize star-shaped polymers having one deutrium-labeled arm, that is, AB_n type star-shaped polymers (n=0, 2, 4). They were preprared by coupling reaction between polystyrene-d_8 macromonomer having terminal two 1,1-diphenyl-ethylene type vinyl groups (A chain) and living polystyrenes-h_8 (B chains),and further coupling reactions of living B, as illustrated in Figure 1. For the synthesis of the macromonomer, two kind of end-capping agent and quencher were used, as shown in Figure2 . Obtained products were fractionated by GPC.

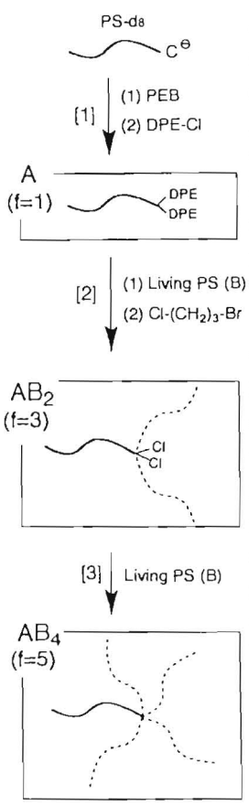

Fig.1 Synthetic scheme of AB_n star polymers.

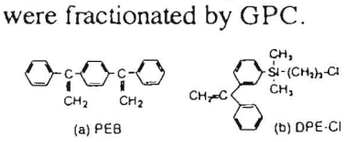

Fig.2 PEB and DPE-Cl

It was confirmed that the obtained products had aimed structures by GPC and GPC-LALLS (Table 1).

Table 1 Characteristics of AB_n star polymers

Sample	10^{-4}Mw	Mw/Mn	f [a]
A	5.67	1.07	—
B	5.53	1.08	—
AB2	15.59	—	2.79
AB4	24.95	—	4.48

[a] Number of arms

The SANS measurements were carried out with SANS-J instrument (λ=0.6nm) equipped with a 10 mm thick quartz cell. Carbon disulfide was used as the solvent. The contrasts of carbon disulfide and polystyrene-h_8 are almost matched.

The apparent R_g of the polystyrene-d_8 part at a certain finite concentration was evaluated by fitting the scattering intensity to the Debye function. And the R_g of the polystyrene-d_8 part was obtained by extrapolation of the apparent R_8 values to infinite dilution.The R_g value for polymer A was obtained by the extrapolation as shown in Figure 3 (R_g=6.60nm). While the R_g of the polystyrene-d_8 part in AB_2 and AB_4 were obtained rather big. It was suggested that the arm chains in star polymers are more expanded than the chains of linear polymers.

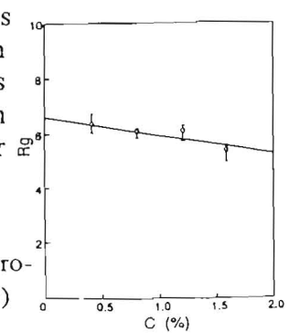

Fig.3 Extrapolation of apparent R_g values to infinite dilution for polymer A.

Reference

1) Y. Matsushita et al. Macromolecules **17**, 1785, (1985)

2.5.8

Microphase-Separated Interfaces of Three-Component Triblock Copolymers

N. Torikai, Y. Matsushita[1], N. Metoki[2] and Y. Morii[2]

School of Engineering, Nagoya University, Furo-cho, Chikusa-ku, Nagoya 464-01
[1]Neutron Scattering Laboratory, ISSP, The University of Tokyo, Tokai, Naka-gun, Ibaraki 319-11
[2]Neutron Scattering Laboratory, JAERI, Tokai, Naka-gun, Ibaraki 319-11

Block copolymers composed of incompatible polymers form microphase-separated structures in bulk. As for diblock copolymers, their microphase-separated structures have been considerably understood at the molecular level owing to a number of studies. The difference between the diblock and three-component triblock copolymers lies in chain conformations in microdomains: both ends of a middle block chain of the triblock copolymer are anchored at different domain boundaries, while one end of diblock copolymer is free. In this study, we investigated the interfaces between microdomains of the triblock copolymers by neutron reflectivity (NR) measurement to understand microphase-separated structures of block copolymers at the molecular level.

Samples used are two poly(isoprene-*b*-styrene-d_8-*b*-2-vinylpyridine)s (IDP). They were synthesized by anionic polymerization. Their molecular characteristics are listed in Table I. They were confirmed to have three-phase four-layer lamellar structures by small-angle X-ray scattering.Thin film specimens were prepared by spin-coating from p-dioxane solutions of IDP on silicon wafers, and they were annealed at 150 °C in vacuum for one week. NR measurement was performed on the triple-axis spectrometer (LTAS) at JRR-3M reactor using neutrons with a wavelength, λ, of 0.63 nm. In this study, specular reflections were observed as a function of neutron momentum transfer, q ($=4\pi\sin\theta/\lambda$), along the direction perpendicular to film surface.

Table I Molecular characteristics of IDP triblock copolymers

Sample Code	$M_n \times 10^{-3}$ [a]	M_w/M_n [b]	ϕ_D [c]
IDP-7	49	1.06	0.36
IDP-6	107	1.03	0.41

[a] M_n is number-averaged molecular weight. [b] M_w/M_n is molecular weight distribution. [c] ϕ_D is the volume fraction of D-block chain.

Figure 1 shows specular reflectivity profile of IDP-6. The profile has been geometrically corrected for finite sample size. It shows several Bragg peaks up to high-q region. This implies that lamellar structures formed in the thin film are highly oriented along the direction parallel to film surface. The detailed analysis of reflectivity data is now in progress.

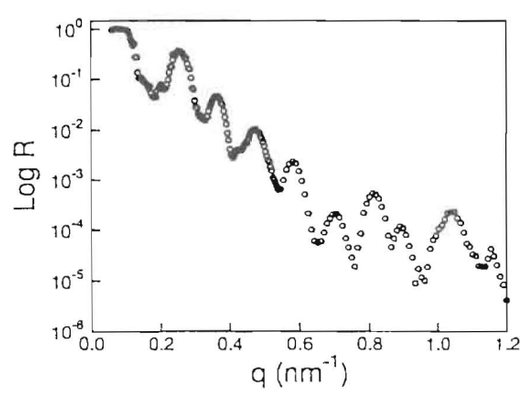

Fig. 1 Specular reflectivity profile of IDP-6 with lamellar structure as a function of q.

2.5.9 Heat Induced Gelation of Bovine Serum Albumin

Y. Izumi, A.Endo, ASakakibara, K.Aizawa[1], S.Koizumi[1] and H.Tomimitsu[1]

Graduate School of Engineering, Yamagata University, Yonezawa, Yamagata 992
[1]Tokai Research Establishment, Japan Atomic Research Institute, Tokai, Ibaraki 319-11

Bovine Serum Albumin (BSA) is one of the globular proteins and abundant in blood plasma. In solution, BSA denatures at a comparatively low temperature, loses some of its α-helical structure, and forms aggregates and gels. Although the thermally induced unfolding, aggregation and gelation of BSA solutions at various pH values and in various concentrations of sodium chloride has been extensively studied, only the structure of gel below 1000A has been studied. The present study is concerned with the direct observation of the gel structure of micron order appeared in the thermally induced gelation of BSA solution using a very small angle neutron scattering (VSANS) technique.

BSA was a pure commercial product from Sigma Chemical Co. (A-7030, lot no. 16H03601) and used without further purification. The concentration of BSA solution was fixed at 15wt%. Two types of gel samples were prepared. One was a transparent and soft gel. The other was opaque and solid gel. VSANS measurements were performed by using the precise neutron optics (PNO) apparatus on a 3G beam hole at JRR-3M.

Fig. 1 shows the VSANS profile of the opaque gel as well as that of D_2O. A prominent difference is observed in a q range larger than 300 pulse. Fig. 2 shows the q-dependence of the excess intensity of the same gel. The scattering data can be analyzed by a simple power-law : $I(q) \sim q^{1-D}$, $q\xi >> 1 >> qa$, in which D is a fractal dimension, ξ is the correlation length of the gel and a is the size of the individual BSA molecule. The VSANS data yielded $D=3.1 \pm 0.05$. For colloidal aggregate structures the experimental D near the gelation threshold ranges between 1.75 and 2.5. The present large value can be interpreted as a structure far below the gelation threshold. On the other hand, the transparent gel gave too very small excess intensity to detect, thereby indicating a structure with a very small contrast or very small junction point.

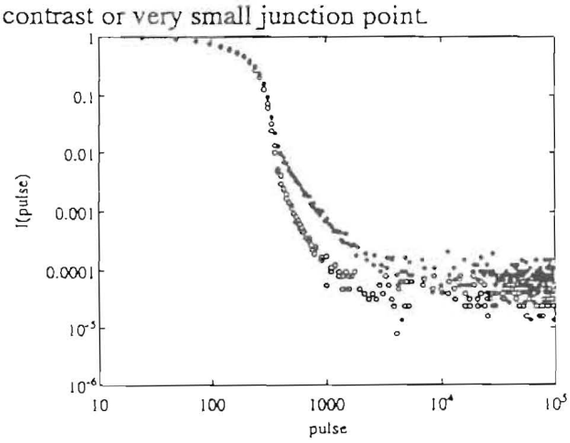

Fig. 1 The VSANS profile of 15wt% BSA gel at 0.2mol NaCl as well as that of D_2O.

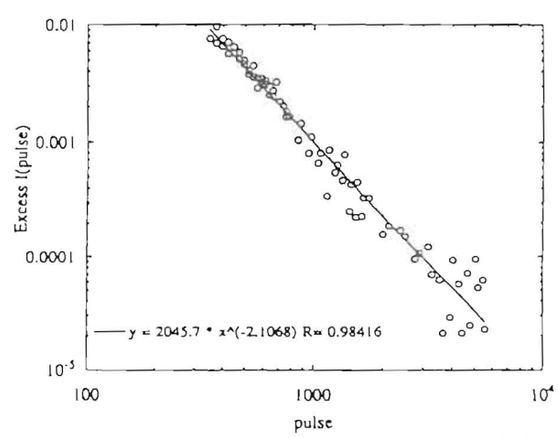

Fig. 2 The q dependence of the excess intensitu of 15wt% BSA gel at 0.2mol NaCl

2.6 BIOLOGY

2.6.1 An Analysis of Hydrogen-Deuterium Exchange Reaction in Cobaloxime Crystals by Single-Crystal Neutron Diffraction

T.Ohhara, Y.Ohgo, J.Harada, Y.Ohashi, I.Tanaka[2], S.Kumazawa[2] and N.Niimura[2,3]
Department of Chemistry, Tokyo Institute of Technology, O-okayama, Tokyo, Japan
Advanced Science Research Center, Japan Atomic Energy Research Institute, Tokai, Ibaraki, Japan[2]
Department of Physics, Tohoku University, Sendai, Miyagi, Japan[3]

It has been found that the chiral cyanoethyl group bonded to the cobalt atom in some cobaloxime complex crystals is racemized on exposure to the visible light without decomposition of the single crystal form. The crystal of the cobaloxime complex with pyridine as an axial base ligand has two crystallographically independent molecules, A and B, in an asymmetric unit. The chiral cyanoethyl group of B is completely inverted to the opposite configuration, whereas that of A remained unaltered. In order to examine the mechanism of the racemization, the cobaloxime complex in which the hydrogen atoms bonded to the chiral carbons of the A and B cyanoethyl groups were replaced by deuterium was prepared and the crystal was exposed to a xenon lamp. The crystal structure after the irradiation was analyzed by neutron diffraction.

Fig. 1 shows the A and B molecules. For the cyanoethyl group of A, the deuterium atom, D14, was exchanged with the hydrogen atom, H16B, of the neighboring methyl group, which is in good agreement with that observed in the similar crystal.[1] For the B cyanoethyl group, on the other hand, the deuterium atom, D30B, was kept in the original position or the equivalent position of the inverted group.

This indicates that the hydrogen-deuterium exchange would occur only if the inversion of the chiral group is prohibited.

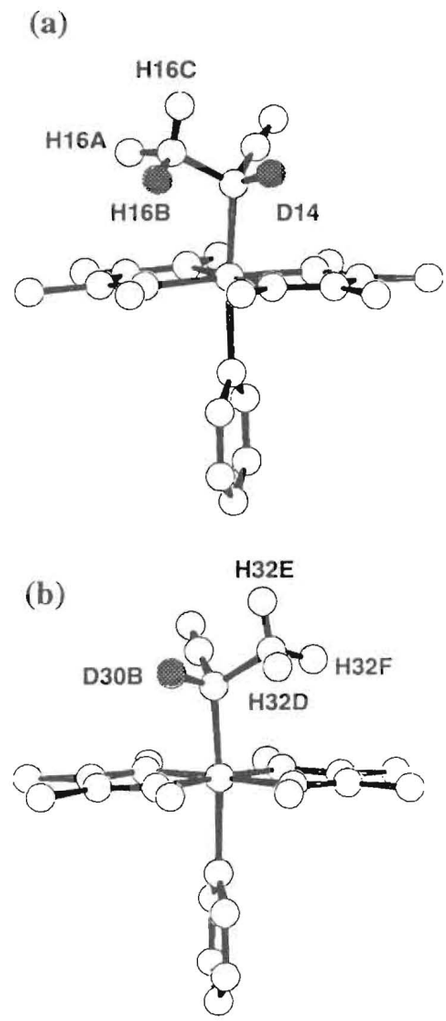

Fig. 1 The molecular structures of (a) A and (b) B chiral cyanoethyl group.

Reference

1) Y.Ohgo, Y.Ohashi, W.Klooster and T.Koetzle, Enantiomer, 2, 241-248 (1997).

2.6.2 A New Diffractometer for Neutron Crystallography in Biology Using Neutron Imaging Plates

S. Fujiwara, Y. Karasawa, I. Tanaka, Y. Minezaki, Y. Yonezawa[1], and N. Niimura

Japan Atomic Energy Research Institute, Tokai, Ibaraki 319-11
[1]Tsukuba College of Technology, Tsukuba, Ibaraki 305

Crystals of biological macromolecules have in general large unit cells so that rather dense diffraction spots are observed. For neutron diffraction measurements of such crystals, detectors with a good spatial resolution and a large sensitive area are required. Neutron Imaging Plates (NIPs) have been recently developed by our group[1]. The NIPs are large flexible sheets of which sensitive area can be several ten-thousands mm^2. They also have a spatial resolution of less than 0.2 mm and more than five orders of magnitudes of dynamic ranges. Such characteristics of the NIPs may be particularly useful for neutron diffraction measurements of biological macromolecules.

We have constructed a neutron diffractometer using the NIP, dedicated to crystallography of biological macromolecules, at the beam port T2-3 in the guide hall of JRR-3M at JAERI. This diffractometer is called BIX-II. 2.2 Å neutrons monochromatized with an elastically bent silicon are used as an incident beam. BIX-II is the first application of the NIPs to the diffractometer for monochromatized neutrons.

Diffraction patterns are detected with the NIP of 400X520 mm^2, bent to a semi-cylindrical shape, at a distance of 150-300 mm from the sample crystals. The thickness of the NIP is 200 μm. The molar ratio of a neutron converter Gd to the photostimulated luminescence materials is 50 %. Data collection can be done either in the step-scanning mode or in the oscillation mode. The IP reader and the eraser are built in BIX-II. A sequence of the measurements (exposure, reading the NIP, erasure, movement of the sample crystal to the next position, and the next exposure) is done automatically. The stored data are processed with the program package for protein crystallography, called Mac-DENZO and SCALEPACK[2].

To check the performance of BIX-II, we measured the diffraction patterns from hen egg-white lysozyme crystals. The patterns were obtained in which many diffraction spots from the lysozyme crystal are observed (see Fig. 5 of "Overview"). It was also confirmed that by using Mac-DENZO and SCALEPACK, these patterns can be processed to obtain the integrated intensity of each spot.

References

1) N. Niimura et al.: Nucl. Instr. Method A349 (1994) 521-525.

2) Z. Otwinowski: in *Data Collection and Processing* (1993) 59-62, and W. Minor: "XDISPLAYF Program", Purdue University (1993).

2.7 INSTRUMENTATION AND METHODS

2.7.1 Performance of LLL-Neutron Interferometer at PNO

Y. Hasegawa, H. Tomimitsu[1], K. Aizawa[1] and T. Takahashi[2]

Department of Applied Physics, University of Tokyo, Bunkyo, Tokyo 113
[1]Japan Atomic Energy Research Institute, Tokai, Ibaraki 319-11
[2]Institute for Solid State Physics, University of Tokyo, Minato, Tokyo 106

A perfect-crystal neutron interferometer (IFM) was constructed and experimentally performed in 1974 by Rauch et al.[1] There, successive Laue case diffractions were used for the beam handling, hence it is conventionally called LLL-IFM. It has stimulated a great deal of new investigations, more or less in the more fundamental and more applied physics; e.g. recently a measurement on the geometric nature of neutron beam is reported.[2] A number of excellent articles of the IFM with perfect crystal were already published.[3-6]

We designed and fabricated a large LLL-IFM. The width, the height and the thickness of each plate are 70mm, 40mm and 1.8mm, respectively. The distance between neighboring plates is about 35mm. This IFM was characterized by x-rays and gave good performances. Magnetic and nuclear phase shifts were observed with the same type of the neutron IFM by our group at JRR-2[7] and preliminary experimental results at JRR-3 were already reported.[8]

In a conventional neutron IFM, a parallel sided Al-plate is inserted between two plates of the IFM as a phase shifter.(Fig.1) When this plate is rotated with an axis vertical to the beams, it increases/decreases an optical path length and introduces the relative phase shift, ϕ, between two split beams. When the phase shift, ϕ, is induced, the intensities, I_0 and I_H, of the O and the H beams would, in practice, change according to

$$I_0 = I_{OSC}(1 + C\cos\phi), \qquad (1)$$

and

$$I_H = I_{BG} + I_{OSC}(1 - C\cos\phi), \qquad (2)$$

where I_{OSC}, I_{BG}, and C represent the intensities of the oscillations, certain theoretical background for the H-beam and the visibility of the interference oscillations. The intensities, I_{OSC} and I_{BG}, depend mainly upon the intensity of the incident beam, beam flux with certain beam cross-section. On the other hand, the visibility, C, depends mainly upon the property of the IFM itself and the experimental conditions.

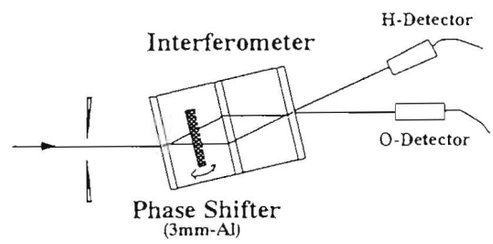

Fig.1 Experimental setup with LLL-Neutron interferometer.

The LLL-IFM was installed at PNO in JRR-3M. The experimental setup is shown in Fig.1. An Al-plate of 3mm in thickness was used as the phase shifter. The wavelength was set to 1.51Å, which gives the Bragg angle of 23.2°. As preliminaries, interference oscillations for O and H beams were measured with and without a solar slit before the graphite double-crystal monochromators. While the amplitudes of the oscillations for two beams are about the same, the visibility for H beam is always lower than the O beam. Since the oscillations for H beam have certain theoretical background as shown in eq.(2), the visibility reduction for H beam is quite reasonable. The interference oscillations for O beam with higher visibilities are of more importance in most cases.

To get interference oscillations with higher visibility, O beam is more important from the theoretical view point. On the other hand, since the direct beam—with inevitable neutrons of higher energy—passes near and parallel to the O beam, the shielding for the O detector from the incident beam is significant. We set a slit of B_4C plates before the detector, and reduced the background as much as possible. The background for O-detector in measuring the

interference oscillations by about 0.1 count/s was accomplished. Typical interference oscillation for O-beam with least square fit is shown in Fig.2, when the beam cross section was 2×4mm^2. The visibility of 42.6% and the amplitude of the interference oscillation of 3.28 count/s were obtained. This intensity is in the same order of that at MURR in USA where many investigations with LLL-IFM are having been made.

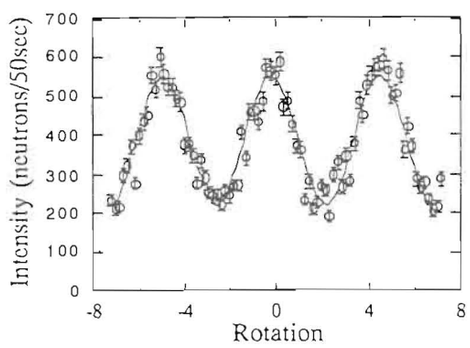

Fig.2 Typical interference oscillation with least squares fits.

A graphite double-crystal monochromator together with various solar slits are equipped at PNO. We have changed the wavelength and collimations with these devices and measured the interference oscillations. There, we found the intensity of the beam has a maximum around with the wavelength of 2Å without any solar slits. But the visibility of the interference oscillations slightly decreased with the beam of longer wavelength. This may be due to an imperfection of the interferometer used here; e.g. distances of each plate of the interferometer were not exactly the same. Interference oscillations with various beam size were measured as well. High visibility oscillations remained even with large beam sizes, which shows that the IFM used here was well fabricated.

Spatial (in)homogeneity of the interferometer was investigated with changing the region of the interferometer. There, we obtained oscillations with somehow higher visibility. Now, we are looking for the exact region, where the highest visibility oscillations can be obtained with the interferometer used here, and the experimental conditions to be improved.

We fabricated another neutron interferometer in larger scale, which was intended to be used also with the wavelength of 2Å with higher intensity. In the near future, it would be possible to optimize the experimental conditions at PNO for neutron interferometry. In addition, we are planning to install some equipments to use the polarized neutron beam, which enables polarized neutron interferometry with perfect crystal neutron interferometer.

Neutron interferometry at PNO in JRR-3M was demonstrated, where the visibility of 43% with the counting rate of the amplitude of the interference oscillation of more than 3.3 count/s was obtained. Further improvements for higher visibility can bring more counting rate of the amplitude of the oscillations. It is feasible to perform the neutron interferometry at PNO with advantages of wavelength-variable and low background double-crystal monochromators, the equipment for the constant temperature control with high accuracy, and the compact and small detector shield with low background. We are planning to perform further neutron interferometry, e.g., new neutron IFM with separated two perfect crystals which will bring a new flavor to a neutron interferometry.

References

[1] H.Rauch, W.Treimer, and U.Bonse, Phys. Lett. **A47** (1974) 369.
[2] Y. Hasegawa, M. Zawisky, H. Rauch and A.I. Ioffe, Phys. Rev. **A53** (1996) 2486.
[3] U.Bonse and H.Rauch (Eds.), Neutron Interferometry, (Oxford Univ. Press, London, 1979).
[4] A.G.Klein, S.A.Werner, Rep. Progr. Phys. **46** (1983) 259.
[5] G.Badurek, H.Rauch and A.Zeilinger (Eds.), "Matter WaveInterferometry" Physica **B151** (1988).
[6] S. Kawano, T. Kawai and A. Kawaguchi (Eds.), "Advance in Neutron Optics and Related Research Facilities" J. Phys. Soc. Jpn Vol. 65 Sppl. A (1996).
[7] S.Nakatani, Y.Hasegawa, H.Tomimitsu, T.Takahashi and S.Kikuta, Jpn. J. Appl. Phys. **30** (1991) L867.
[8] H. Tomimitsu, Y. Hasegawa, K. Aizawa and S. Kikuta, Physica **B213&214** (1995) 836.

2.7.2 Determination of the Scattering Lengths of the Gallium-Isotopes by Neutron Interferometry at the PNO in JRR-3M

Hiroshi Tomimitsu, Yuji Hasegawa[1], Kazuya Aizawa and Seishi Kikuta[1]

Advanced Science Research Center, JAERI, Tokai, Ibaraki, 319-11 Japan
[1]Faculty of Engineering, Tokyo University, Hongo, Bunkyo, Tokyo, Japan

Nowadays, the low-energy neutrons are very important tool for the investigation of condensed matter and nuclear physics. Consequently, the neutron scattering length of every elements or isotopes are very important as the basic quantity, and many values determined by various methods have been tabulated[1]. It seems, however, that several values of them should be made much more accurate.

We determined the accurate values of the coherent scattering lengths of gallium isotopes with the interferometry at the PNO-apparatus.

Neutron interferometry was carried out at the PNO. With the beam-collimator of 30min. of arc., the wavelength was selected as 0.15123nm. The cross section of the neutron beam was restricted to 2mm in width and 4mm in height.

An LLL-type Si interferometer was used in the measurements[2].The experimental set-up is schematically shown in Fig.1, where the beam-paths are also shown. Because of their small amount, the specimens were set so as to receive the transmitted-beam only behind the 1'st reflecting plate(splitter) of the interferometer, as indicated in Fig.1.

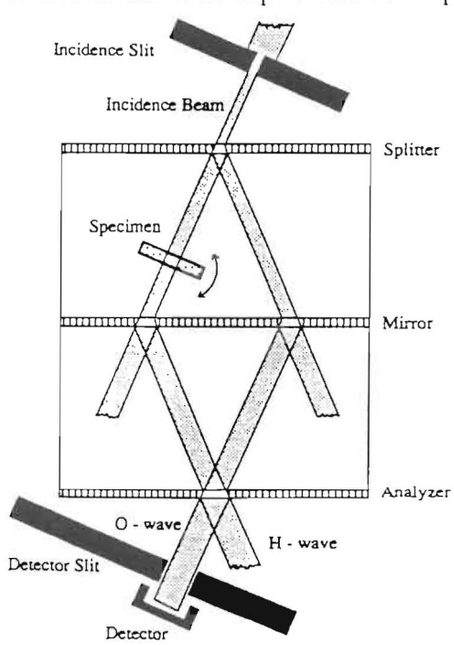

Fig.1 Schematic Drawing of the Experimental Set-Up. The LLL-type interferometer and the specimen are shown with the beam paths.

^{69}Ga of 99.7% purity and ^{71}Ga of 99.6% purity were used as the specimen. They were melt in a warmed water bath, and put in a flat glass cell, respectively. The resultant thickness was 2.000 mm for both specimen and the surface area of around 1*1cm^2. Those isotopes stayed in the supercooled liquid state during all the measurements.

We measured the oscillation of the intensities with the specimen-rotation within ±30 deg. of arc. or so. The measuring period was 300 sec for every specimen position. Measurements were repeated ten times for both specimens, and very similar curves were obtained, respectively.

Fig.2 and Fig.3 show the typical examples of the measured oscillation curves of ^{69}Ga and ^{71}Ga,

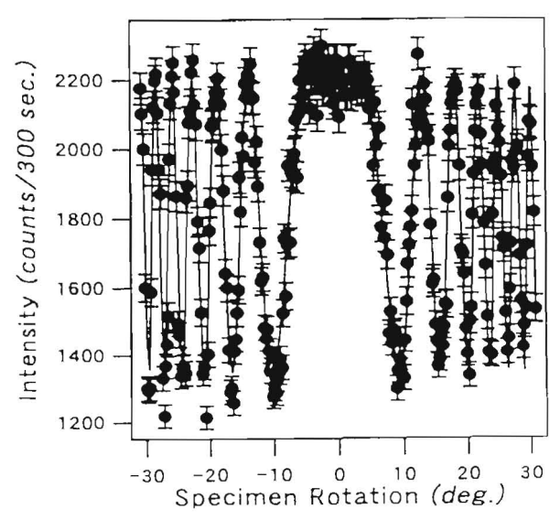

Fig.2 Example of the Intensity Oscillation Curve of ^{69}Ga with the Least Square Fitting.

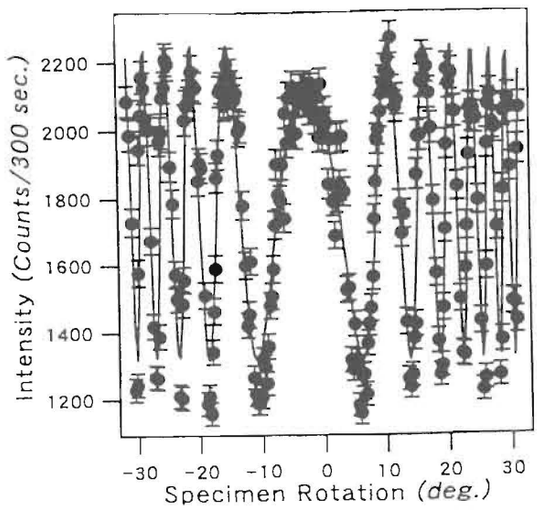

Fig.3 Example of the Intensity Oscillation Curve of ^{71}Ga, with the Least Square Fitting.

respectively, with the least square fits, to be mentioned bellow, on the experimental data with the standard error bars.

In addition, we also measured the oscillations of the vacant glass cell to obtain its effect on the specimens contained in it, a typical example being shown in Fig.4.

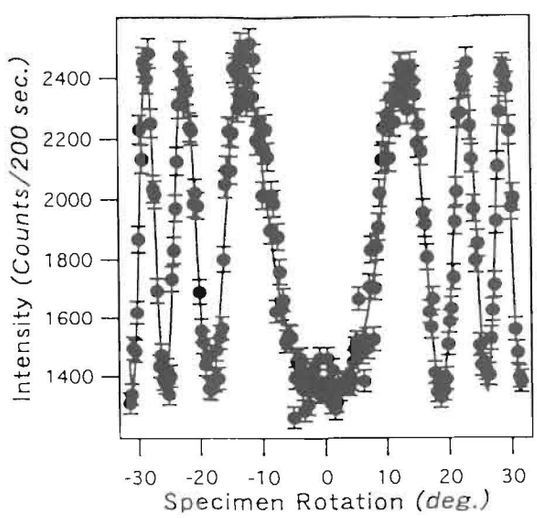

Fig.4 Example of the Intensity Oscillation Curve of the vacant glass cell, with the Least Square Fitting.

Next, we analyzed the experimental data following the equation;

$$I=A\cos(B/\cos(\omega+C))+D \quad \cdots\cdots(1),$$

where the parameters mean as following;

ω: the amount of specimen rotation from the original angular position,
A: apparent amplitude of the intensity-oscillation,
B: this includes all of the physical meanings as

$$B=-N\lambda tb \quad \cdots\cdots(2)$$

with N=atomic density of the specimen,
λ=wavelength of the neutron used,
t=thickness of the specimen, and
b= the coherent scattering length to be determined;
C: amount of the angular mis-setting from the ideal origin of the specimen, and
D: apparent back-ground part in the intensity-oscillation including all of the imperfectness of the experimental condition, respectively.

With a conventional least square method, we analyzed all the experimental curves, as already shown in Fig.2-4, and obtained the B's for the Eq.(2) as 127.97 for ^{69}Ga and 98.08 for ^{71}Ga, respectively, after reducing the effect of the glass cell.

Finally, we obtained the accurate value of the coherent neutron scattering length as b=6.156 fm for ^{69}Ga, and b=8.030 fm for ^{71}Ga, respectively.

Results, determined above, were significantly different from the known values obtained by other method. On the other hand, the values of the high purity aluminum, niobium and natural gallium, which were also measured as the standard specimens in the present experiment, were almost the same as the known values.

The coherent neutron scattering lengths of ^{69}Ga and ^{71}Ga were, thus, successfully obtained by the interferometry at the PNO.

References

1) L.Koester, H.Rauch and E.Seymann: Atomic Dta and Nuclear Data Tables 49(1991) 65.
2) The characterization of the interferometer used is described in p. of this issue.

2.7.3

Fabrication and Characterization of NiC/Ti monochromator with a period of 40Å

Kazuhiko SOYAMA

Japan Atomic Energy Research Institute, Tokai, Ibaraki, 319-11

Artificial multilayer monochromator with very short d-spacing of 40 Å has been fabricated in order to manipulate cold neutron and ultra cold neutron.

NiC_x/Ti multilayers[1] and Ni/Ti multilayer consisting of 100 bilayers with a period of 40Å were deposited with changing carbon mixing ratio in the nickel layer using an ion beam sputtering deposition system. They were deposited on silicon substrates with a size of 100 mm × 100 mm and with a surface roughness of 2 Å rms. Mixing carbon effect to the neutron reflectivity of the NiC_x/Ti multilayer has been investigated.

The reflectivity profiles of the NiC_x/Ti multilayers with a typical carbon mixing ratio x, at which the multilayer shows the highest reflectivity, is shown in Fig.1. The maximum reflectivity displays 10% at Q=0.165. The small peak at Q=0.08 is the reflected signal of second order neutrons. The specular reflectivity was measured at a neutron reflectometer installed on C2-1 port at JRR-3M. The incident neutron has 3 Å.

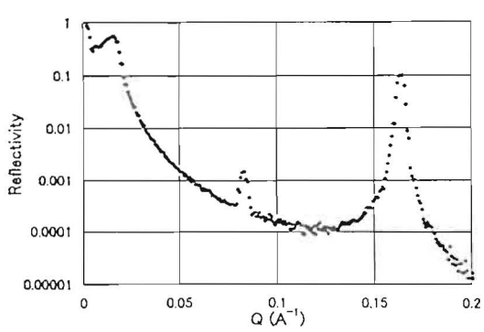

Fig.1 Specular neutron reflectivity of NiC_x/Ti multilayer with a period of 40 Å

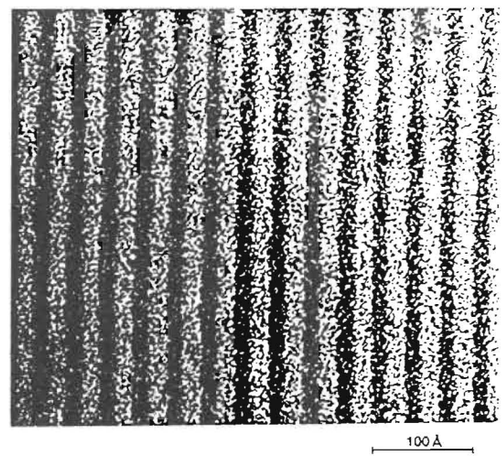

Fig.2 TEM image of of NiC_x/Ti multilayer with a period of 40 Å

TEM cross-sectional observations were conducted using TEM (H-9000NAR) at 300kV acceleration voltage. The NiC_x/Ti multilayers with various carbon contents and Ni/Ti multilayers were prepared. Each multilayer consists of 100 bilayers and is with a period of 40Å. Fig.2 shows a TEM image of the above mentioned NiC_x/Ti multilayer. NiC_x layers (dark area) shows almost amorphous structure, while Ti layers are micro-crystalline structure. The multilayer structure shows a small degradation caused by titanium micro-crystalline. The observed d-spacing is 33Å, and layer thickness ratio is 1.5.

This monochromator can reflect neutrons with a wavelength of 20 Å at a reflection angle of 29°, so it could be used to deflect or focus slow neutrons for the various neutron experiments.

References

1) J.Wood :SPIE Vol.1738 (1992) 22

2.7.4

Tunneling Abstraction Reactions of Tritium Atoms with mixtures of H_2 and D_2 in Super- and Normalfluid ^{3}He - ^{4}He media at 1.3 K

Y.Aratono, T.Matsumoto,[1] T.Takayanagi, T.Kumada, K.Komaguchi [2] and T.Miyazaki[1,2]

Japan Atomic Energy Research Institute, Tokai, Ibaraki 319-11
1 School of Engineering, Nagoya University, Chikusa-ku, Nagoya 464-01
2 Faculty of Engineering, Hiroshima University, Higashi Hiroshima 739

The abstraction reactions, T + $H_2(D_2)$→ HT(DT) + H(D) were studied experimentally in liquid ^{3}He-^{4}He media at 1.3 K and theoretically using the gas-phase reaction model. The experimental reaction system has two characteristics; one is that the tritium atom(T) is produced from one of the constituents, ^{3}He, through ^{3}He(n, p)T nuclear reaction and the other is that super- or normalfluid reaction medium can be chosen arbitrarily by changing the composition and temperature of the sample.

The mixture of ^{3}He, ^{4}He, and 1 mol % of the reactants, H_2, D_2 or H_2 + D_2, was introduced into Pyrex glass reaction vessel(about 3.8×10^3 cm^3) with quartz-made irradiation tube(6 mm in inner diameter, 1 m in length) and cooled to 1.3 K. The atomic compositions of the liquefied solution were ^{3}He : ^{4}He = 0.670 : 0.330(normalfluid solution), and ^{3}He : ^{4}He = 0.282 : 0.718(superfluid solution). Thermal neutron irradiation was performed at JRR-2(DMNS) and JRR-3M(TAS-1) for about 10-50 hrs at 1.30±0.02K. The irradiated sample was analyzed by radiogas chromatograph equipped with a gas-flow proportional counter. The reaction products, HT and DT, were separated at 77 K using γ-alumina column coated with Fe_2O_3.

Table 1 shows the product distribution and isotope effects under the various experimental conditions. The effect of D_2 addition is very suggestive. In spite of no addition of H_2, 62.8±2.9 % of T is observed as HT. The most plausible source of H is considered to be impurity included in D_2 gas. If so, the result suggests a large isotope effect for HT and DT formation. In order to confirm the isotope effect definitely, a predetermined amount of H_2/D_2 =1/9 was added in the system. A clear evidence of preferential formation of HT over DT was observed in this reaction system. From the yields of HT and DT shown in Table 1, the isotope effects, defined as $\{[HT]/[H_2]\}/\{[DT]/[D_2]\}$, were calculated to be 158 for superfluid and 146 for normalfluid solutions.

The isotope effects for T + $H_2(D_2)$ → HT(DT) + H(D) above 77 K have been experimentally examined by some workers. The present results exceed by about two orders of magnitude over the gas phase values and are rather close to the isotope effects of the abstraction reactions of H and D in the solid H_2, D_2, and HD at around 4 K, where the importance of the tunneling in the abstraction reaction was well established.[1-3] The large isotope effects of 158 and 146 are qualitatively explained by the large isotope effect of about 10^6 calculated theoretically. From the comparison of experimental isotope effects with theoretical ones, we propose the tunneling abstraction reaction through van der Waals complex as shown below.

Since the interaction of T and H_2 or D_2 has a long-range and attractive force and the experimental temperature is very low, the formation of a van der Waals complex

$(T \cdots H_2)_{comp.}$ or $(T \cdots D_2)_{comp.}$ prior to the abstraction reaction is considered to be reasonable. Actually, the van der Waals complex of a hydrogen atom and a hydrogen molecule has been predicted theoretically[4,5] and observed experimentally very recently by the authors in tunneling reaction HD + D → H + D_2 in argon matrix at 20 K.[6] According to the ab initio calculation by Boothroyd et al.,[5] well depth of van der Waals interaction is reported to be 0.047 kcal mol^{-1}. The geometry at the minimum of the van der Waals Well is collinear and the distance between H and the center of mass of H_2 is to be 3.7A. If we take the formation of this van der Waals complex into our kinetic model, the possible pathways leading to the formation of HT and DT may be expressed as follows,

$$T + H_2 + (He) \rightarrow (T \cdots H_2)_{comp.} - (reaction) \rightarrow HT + H \quad (1)$$

or the complex would dissociate by the collision with He,

$$(T \cdots H_2)_{comp.} + He - (dissociation) \rightarrow T + H_2 \quad (2)$$

The similar reaction scheme will hold for T + D_2 ,

$$T + D_2 + (He) \rightarrow (T \cdots D_2)_{comp.} - (reaction) \rightarrow DT + H \quad (3)$$

or $$(T \cdots D_2)_{comp.} + He - (dissociation) \rightarrow T + D_2 . \quad (4)$$

Although the branching ratio of the reaction to the dissociation has not been well known, it seems to be reasonable that the life time of $(T \cdots D_2)_{comp.}$ is longer than that of the complex $(T \cdots H_2)_{comp.}$ and thus the reaction (1) might prevail over the reaction (3) to lead to the preferential formation of HT. Further theoretical and experimental investigations are necessary for the quantitative understanding of the reaction mechanism.

Acknowledgements

The authors thank to Mr. Minagawa H. and Mr. Shimojyo M. of Neutron Scattering Research Group of Japan Atomic Energy Research Institute for their many advices in neutron irradiation and to Dr. Yonezawa C. and Mr. Sasajima F. for their help in activation analysis of Au-foil. The present research was supported in part by a Grant in Aid for Scientific Research from the Japanese Ministry of Education, Science and Culture.

References

1) T. Miyazaki, Radiat. Phys. Chem., **37**(1991) 635.
2) T. Miyazaki, S. Kitamura, H. Morikita, K. Fueki, K. J. Phys. Chem. **96**(1992) 10331.
3) T. Kumada, K. Komaguchi, Y. Aratono, T. Miyazaki, Chem. Phys. Lett., **261**(1996)463.
4) T. Takayanagi and S.Sato: J. Chem. Phys. **92**(1990) 2862.
5) A. I. Boothroyd, W. J. Keogh, P. G. Martin, M. R. Peterson: J. Chem. Phys., **95**(1991) 4343.
6) K. Komaguchi. T. Kumada, Y. Aratono, T. Miyazaki: Chem. Phys. Lett. (in press).

Table 1 Distribution of HT and DT under the various experimental conditions and experimental isotope effects

^3He:^4He	state	additives	HT (%)	DT (%)	isotope effects
0.282:0.718 [(a)]	s	H_2, 1 vol %	100	0	-------
(b)	s and n	D_2, 1 vol %	62.8±2.9	37.2±2.9	-------
0.282:0.718	s	H_2/D_2=1/9, 1 vol %	94.6±1.1	5.4±1.1	158
0.670:0.330	n	H_2/D_2=1/9, 1 vol %	94.2±0.8	5.8±0.8	146

(a) deuterated quartz tube (b) ^3He : ^4He=0.670 : 0.330 and 0.282 : 0.718

2.7.5 Performance Test of a System for Generating Triple Extreme Conditions for Neutron Scattering Experiments

A. Moriai, S. Ichimura, A. Ohtomo, S. Kawano[1], S. Fukui[1],
A. Onodera[2], F. Amita[3], S. Katano[4]

Department of Research Reactor, JAERI, Ibaraki, 319-11
1 Research Reactor Institute, Kyoto University, Osaka, 590-04
2 Faculty of Enginering Science, Osaka University Toyonaka, 560
3 Faculty of Science, Kyoto University, Kyoto, 606
4 Advanced Science Research Center, JAERI, Ibaraki, 319-11

Summary

A new system generating conditions of high pressure, high magnetic field and low temperature simultaneously for neutron scattering experiment have been developed. The performance test for the system is now in progress by neutron scattering experiment using TAS-2 at JRR-3M of JAERI.

Constitution of the system

The system as shown in Fig. 1 is equipped with a non-magnetic clamp-type high pressure cell which aims at 2.5 GPa, a superconducting magnet attainable to 5 Tesla vertically and a variable-temperature insertion containing the cell which is cooled with evaporated helium. Furthermore, a couple of coils with asymmetric shape enable polarized neutron scattering experiments.

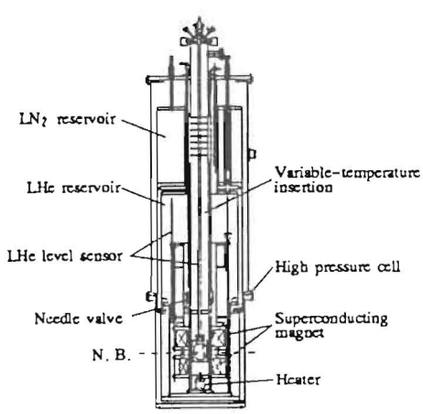

Fig. 1 Cross-sectional view of the system for generating triple extreme conditions for neutron scattering experiments.

Performance test

As one of the performance tests for the system, a magnetic phase transition of $TbNi_2Si_2$ single crystal have been observed under low temperature and high magnetic field by neutron scattering measurment. The single crystal was mounted in the system as c-axis is vertically oriented to make scans in the a*-b* reciprocal lattice plane for 1.7 K - 20 K and 0 Tesla - 5 Tesla.

Figure 2 shows field dependence for magnetic scattering peaks. With increasing magnetic field, ferromagnetic (110) phase grows with typical multi-step metamagnetic process. While, some antiferromagnetic phases, which associate with incommensurate propagation vectors Q, appear and disappear succesively. The present results are in good agreement with those of recent study[1].

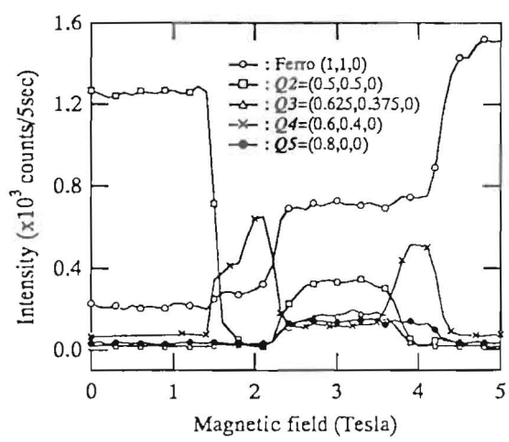

Fig. 2 Field dependence of magnetic scatterig peaks.

The performance test under high pressure (0.7GPa), high magnetic field and low temperature as next step is now in progress, and then polarized neutron test is also planned.

References

1) J. A. Blanco *et al.*
J. Magn. Magn. Mat. 97 (1991) 4-14

2.7.6 Development of liquid ^{4}He free dilution refrigerator for neutron scattering

Y. Koike[1], Y. Morii[1], T. Igarashi[2] and M. Kubota[2]

[1] *Advanced Science Research Center, JAERI, Tokai, Ibaraki 319-11*

[2] *Institute for Solid State Physics, University of Tokyo, Roppongi, Tokyo 106*

The ^{3}He/^{4}He dilution refrigerators (DR) are now widely available for the typical temperature region from 1 K to 10 mK. Recently demand of the DR in neutron scattering experiments becomes greater to study attractive phenomena at low temperatures. Therefore we decided to construct liquid ^{4}He free DR in order to give not only easy operations but also less running cost to the experimenters. We have designed a DR named mK cryocooler and made a prototype refrigerator to develop. The main characteristics are as follows.

A two-stage hybrid cryocooler consisted of Gifford-MacMahon (G-M) cycle and pulse tube refrigerator was adopted for 4.2 K precooling stage. The cooling power of the hybrid cryocooler is about 0.3 W at 4.2 K [1], which is enough power to operate the DR without liquid ^{4}He and N_2 coolants.

The DR is Joule-Thomson (J-T) type, which has not pumped ^{4}He stage (1 K pot). The ^{3}He/^{4}He mixture gases are cooled below inversion temperatures of J-T expansion to be liquefied. Evaporating ^{3}He gas is used for precooling the entering gas. We mounted a turbomolecular pump on the top flange of the mK cryocooler to increase the cooling power of the DR.

We are carrying on the running tests of the mK cryocooler.

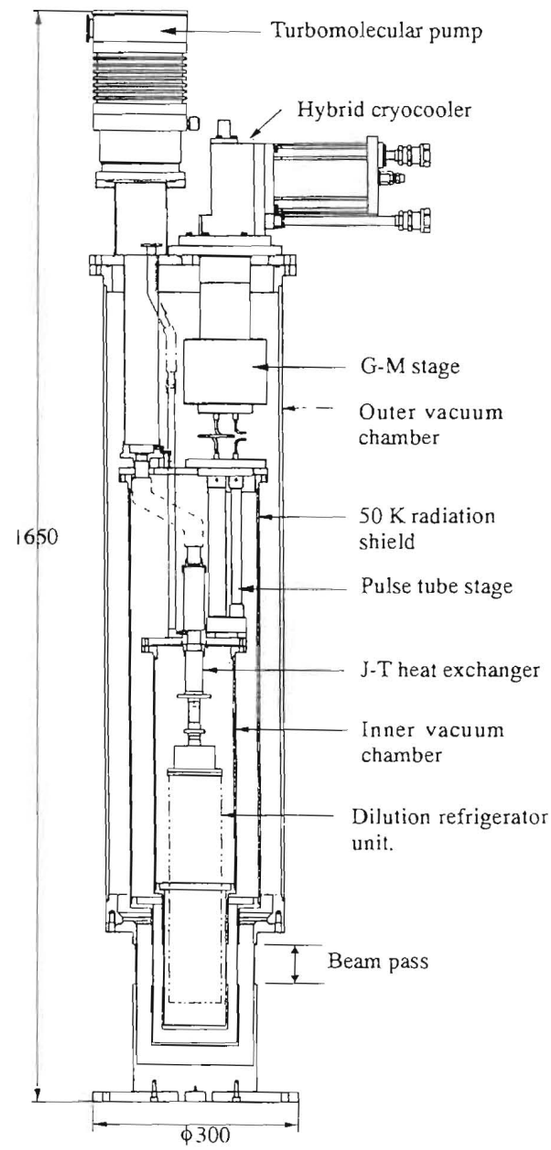

Schematic drawing of the mK cryocooler

Reference

[1] K. Tanida, J. L. Gao, Y. Hiresaki and Y. Matsubara: Proceedings of ICEC16/ICMC (1996) 303.

2.7.7 Polarization analysis option on TAS-1

T.INAMI and S.KATANO

Japan Atomic Energy Research Institute, Tokai, Ibaraki 319-11

Application of polarized incident neutrons and analysis of the polarization of scattered neutrons are powerful tools in neutron scattering experiments. Since we have installed polarization analysis options on TAS-1 (2G), we report on the results.

The polarization analysis apparatus consists of a monochromator, a spin flipper, coils which apply a magnetic field to a sample, guide fields and an analyzer. For a monochromator and an analyzer, the Heusler (111) reflection was employed. Both crystals are used in the reflection geometry and, in order to saturate the magnetization, they are inserted between NdFeB magnets. The spin flipper is a π flipper, which is made up of two $\pi/2$ flippers.

A performance of a polarization analysis instrument is indicated by its flipping ratio. We thus measured the intensities of a (111) reflection of a Ge single crystal when the flipper was on and when the flipper was off, for several incident neutron energies. An example is shown in fig.1. The measured flipping ratios – (intensity at flipper-off) / (intensity at flipper-on) – are summarized in table 1. At low incident energies, we obtained extremely good flipping ratios of $\sim$ 50. The intensities of the detected neutrons were about 1/50 of these at an unpolarized setting using PG(002) monochromator and analyzer.

As a demonstration, we measured paramagnetic scattering of MnF_2. In order to detect only the magnetic scattering, which contains spin flip process, the spin flipper was in operation during the measurement. In addition, to remove the neutrons scattered incoherently by nuclear spins, we measured the difference between the intensities when the neutron polarization was parallel to the scattering vector and those when vertical to the scattering vector. The result is shown in fig.2. One can see that the observed intensities follow the square of the magnetic form factor of Mn^{2+}.

In conclusion, polarized neutrons and polarization analysis are now available on TAS-1. Very good flipping ratios are obtained at low incident energies. This option is expected to be very useful for the measurements to determine the direction of ordered moments or to find out the polarization direction of magnetic excitations.

Table 1: Obtained flipping ratios

incident energy (meV)	13.6	14.7	30.5	34	42
flipping ratio	48.5	42.7	18.8	22.1	16.0

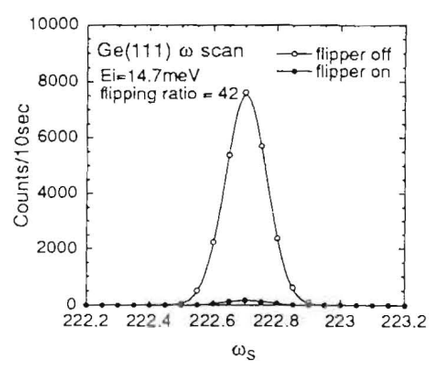

Figure 1: Rocking curve of Ge (111)

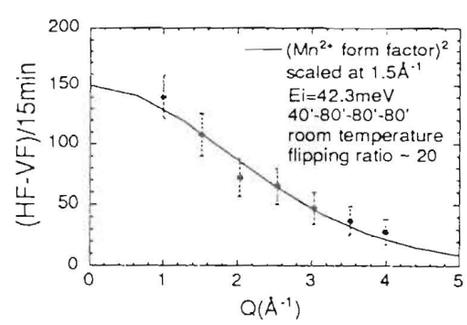

Figure 2: Paramagnetic scattering of MnF_2

2.7.8 Application of techniques for intense beam reflection to neutron monochromator

N. Minakawa, Y. Morii, Y. Shimojo, A. Moriai
Japan Atomic Energy Research Institute, Tokai Ibaraki 319-11

1. Introduction

It is quite important to develop techniques for neutron monochromators which utilize valuable neutrons more effectively. There are two methods to make monochromated beam, one is the velocity selector method, and the other diffraction method by single crystals.

We have developed technology to increase neutron intensity at the sample position using single crystal. We applied stress to bend silicon single crystal and to increase mosaic spread of the perfect crystal. Utilizing the bent silicon crystals, we can focus monochromated neutron beam in the horizontal direction, and increase diffracted beam intensity simultaneously. In order to focus neutron beam in the vertical direction, several single crystals were arrayed in the vertical direction with the adjusted tilt angles. We made a bending and focusing monochromator system and succeeded in increasing neutron beam intensity at the sample position.

2. The monochromator system

The size of the silicon crystals was 20 mm in length, 100 mm in width and 5 mm in thickness. The largest plane of the crystal is 311 plane. The crystal was grown by FZ method by Shin-etu chemical Co. Piano wire of which diameter is 0.9 mm was used to bend the crystal. Eleven strips of silicon crystal were used for High Resolution Powder Diffractometer(HRPD) and five for Diffractometer for Residual Stress Analysis(RESA). HRPD monochromator system enables us to adjust crystal ω angle independently within $\pm$ 2 degrees. A remote control of the tilt angle of the each crystal is available in the range from – 0.5 to + 4.5 degrees in the vertical direction. We applied a bending stress of approximately 66 MPa to the each crystal.

3. Result

In the case of the flat monochromator, only 4.4 % of monochromated beam can be used for the typical sample of which size is 10mm in diameter and 35mm in height. While in the case of the focusing monochromator, neutron beam can be converged to the size of 20mm in width and 35mm in height, which was measured by a neutron camera. This means that about 50% of focusing neutrons can be used for the scattering experiment, therefore that ten times as intense as neutron beam becomes available.

The observed diffraction intensity from a standard silicon powder sample with the bent silicon monochromator was about 45% of that with the PG monochromator using a similar wavelength of 0.21nm. (See Fig-1)

Since we can increase bending stress up to approximately 124MPa where the crystal was broken, it is expected to obtain even stronger neutron beam intensity.

Fig-1 Si(220)POWDER DIFFRACTION WITH PG AND Si MONOCHROMATOR

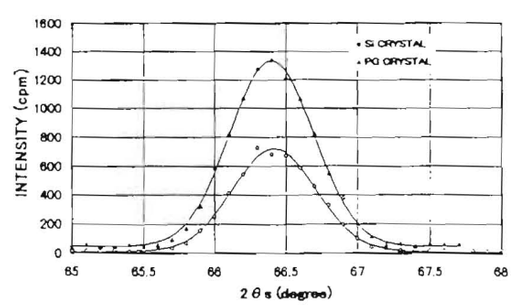

2.7.9 An Elastically Bent Silicon Monochromator for Neutron Diffractometers — Thickness Optimization —

I. Tanaka and N. Niimura[1]

Advanced Science Research Center, JAERI, Tokai, Ibaraki 319-11
1 Advanced Science Research Center, JAERI, Tokai, Ibaraki 319-11 (on leave from Tohoku University)

An elastically bent perfect crystal Si (EB-Si) can be used as a monochromator and an analyzer for several types of neutron instruments, such as diffractometer for bio-crystallography[1)], triple axis spectrometer[2)] and small angle scattering diffractometer[3)] due to its high luminosity and its low angle divergence. We have successfully applied the EB-Si monochromators to two diffractometers for bio-crystallography (BIX-I[1)] and II) installed at 1G-A and T2-3 in JRR-3M, JAERI. In this report the preliminary results of thickness optimization of EB-Si will be shown.

Several symmetrically cut Si(220) plates (large surface) with dimensions of 170 × 20 × 2.5 (thickness) mm^3 were stacked, bent at fixed R ~ 6m and set at the monochromator (M) position of triple axis spectrometer (TAS-2) located at the end of the guide tube, where $2\theta_M=68^\circ$ and the incident beam width was 20mm. Reflected intensity was measured by a neutron imaging plate (NIP). The NIP and a beam narrower (slit) were set at 1.3m and at 1.0m far from M respectively. There were no collimations between M and the beam narrower.

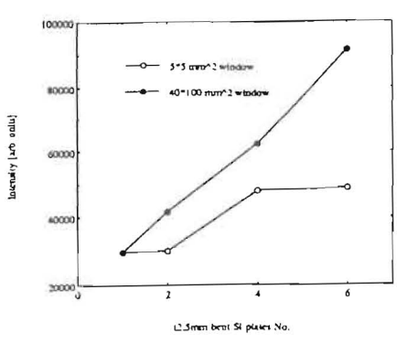

Fig. 1 Relation between cross section intensities and number of bent Si plates at the same curvatures.

Fig. 1 shows cross section intensities versus crystal thickness' of 1, 2, 4 and 6 stacked plates. Open circles indicate intensities when the beam narrower was 5 × 5mm^2 (collimated beam), and closed circles indicate intensities when the beam narrower was 40 × 100mm^2 (fully opened beam).

While the intensity of fully opened beam increases in proportion to thickness, the collimated beam increases only to 10mm thickness. It should be noted, however, that a cross section image of 15mm thickness was widely spread so that only 3 to 4 plates fraction of stacked 6 plates contributed the peak intensity (Fig. 1 and 2). If one aligns each plate correctly, the collimated beam should also increase according to thickness and more neutrons will be expected till the geometrical limit, for example, 24mm in thickness and then $\Delta\lambda/\lambda \fallingdotseq 5\%$ in the case of BIX-II.

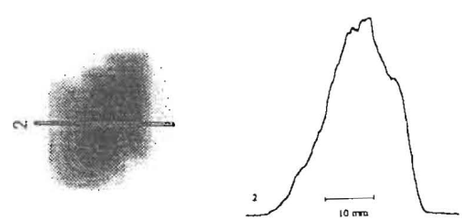

Fig. 2 Cross section (left) and its profile (right) of reflected beam from 6 plates. Note that cross section images from each satcked plate are shifted.

References

1) N. Niimura, I. Tanaka and *et al.* , Physica B **213&214** (1995) 786-789.
2) J. Kulda and J. Saroun, Nucl. Instr. Meth. A **379** (1996) 155-166.
3) M. Popovici, W. B. Yelon, R. Berliner and B. J. Heuser, J. Phys. Chem. Solids **56** (1995) 1425-1431.

2.7.10 What to be considered for Practical Use of Neutron Imaging Plate.

Y.Karasawa and N.Niimura

Advanced Science Research Center, Japan Atomic Energy Research Institute, Tokai, Ibaraki, 319-11

We have developed a Neutron Imaging Plate (NIP) as a new neutron detector and already reported the basic properties of the NIP[1].

Although the NIP is a high quality detector , there are some problems to be solved when we apply it to neutron experiments.

1) neutron wavelength dependence of the NIP

The wavelength dependence of the NIP efficiency is important especially in a Laue case where white neutrons are used. The NIP efficiency is a product of the neutron capture efficiency, the color center creation efficiency and the absorption effect of read-out laser and luminescence from the NIP itself.

We have observed PSL intensity of the NIP by changing neutron wavelength at TAS-2 and LTAS.

Observed PSL was normalized by the incident neutron intensity monitored with a ^{3}He detector. The ^{3}He detector efficiency is assumed to be 100% in this wavelength range. The normalized value corresponds to the PSL intensity created by one incident neutron.

In case of Gd-IP, since neutron capture efficiency is nearly 100% in this wavelength range, PSL does not depend on the wavelength. On the other hand, in case of ^{6}Li-IP, PSL increases as neutron wavelength becomes longer because neutron capture efficiency is so low,14% at 1.0 Å. Since the energy of the secondary particles of ^{6}Li(α : 2.05MeV and ^{3}H : 2.74MeV) emitted by neutron capture is higher than that of Gd (conversion electron : 70keV) , PSL/neutron of ^{6}Li-IP is higher than that of Gd-IP.

2) γ -ray sensitivity

Since the PSL materials of the NIP are the same as that of X-ray IP, the NIP is sensitive to γ -ray. Consequently shielding of γ -ray as well as neutron is required for neutron beam experiments. The γ -ray sensitivity of the NIP and γ -ray shielding effect of lead for the NIP have been examined.

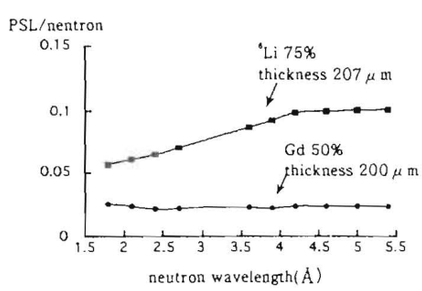

Fig.1 wavelength dependence of the NIP
50% of Gd doped and 75% ^{6}Li doped , respectively

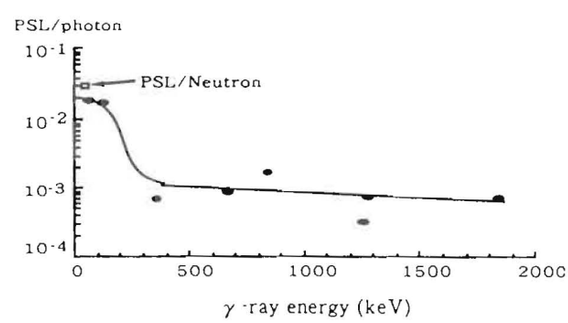

Fig.2 γ -ray sensivity of NIP
Abscissa ; γ -ray energy
Ordinate ; PSL created by one photon

Fig.2 shows the energy dependence of the γ-ray sensitivity of the NIP. Radioactive isotopes such as ^{88}Y, ^{22}Na, ^{60}Co, ^{54}Mn, ^{134}Cs, ^{133}Ba, ^{57}Co and ^{241}Am were used as γ-ray sources. Observed PSL was normalized by the incident γ-ray intensity monitored with a Ge detector. The energy dependence of the Ge detector efficiency is corrected. The normalized value corresponds to the PSL intensity created by one γ-ray photon.

The PSL/photon at higher energy than 300keV γ-ray decreases to 1/20 of the PSL/neutron. At the low energy (less than 30keV) γ-ray, the PSL/photon is about half of the PSL/neutron.

The γ-ray shielding effect of lead was examined at the BIX-I site in the reactor JRR-3M. The X-ray IP has been used instead of the NIP in order to avoid the neutron detection effect where the γ-ray sensitivity of NIP and Xray-IP is assumed to be the same.

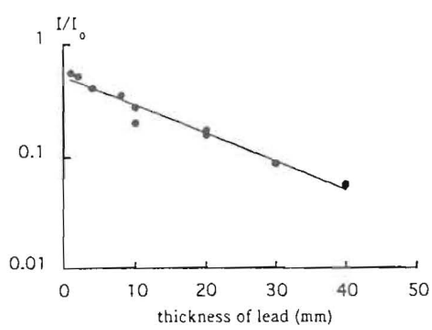

Fig.3 lead shield effect in the reactor room

Fig.3 shows the γ-ray shielding effect of lead. Abscissa is thickness of lead. Ordinate is shielding effect of lead (I is the PSL intensity shielded by lead and I_0 is PSL intensity without Pb). This suggests that 2.5cm thick lead is required to reduce γ-ray background to 10%.

(3) The effect of radioactive products in the NIP created by irradiated neutron

Some elements of the NIP might be radioactivated by neutron and they create the color center which causes background. We measured the PSL intensity caused by radioactivated product and identified the isotope.

Fig.4 shows the intensity decay of the PSL created by radioactivated products. Consideration of half life time of the possible radioactive isotope indicates that there are at least three components of possible isotopes, ^{152}Eu (9.16hrs), ^{80}Br (17.68min), ^{82}Br (1.47day) . Total PSL intensity created by radioactivation is less than 0.04% of PSL created by neutron. Consequently radioactivation will not affect to neutron experiments.

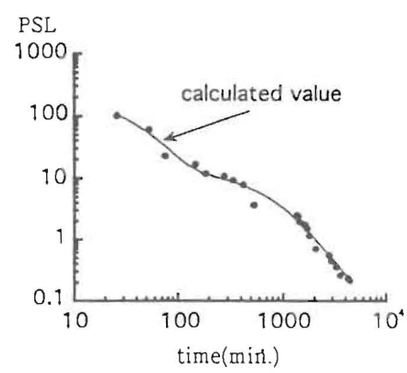

Fig.4 The intensity decay of the PSL created by radioactivated products

References

1) N.Niimura et al, Nucl.Instr.Mehtods, A349,521-525(1994)

2.7.11 Development of Nondestructive Method for Evaluation of Material Strength

K. Tanaka, M. Hayashi[1], K. Inoue[2], Y. Tsuchiya[3] and N. Minakawa[3]

Faculty of Engineering, Nagoya University, Nagoya, 464-01
1 Mechinical Engineering Research Laboratory, Hitachi Ltd., Hitachi, 317
2 Faculty of Science and Technology, Ryukoku University, Otsu, 520-21
3 Japan Atomic Energy Research Institute, Tokai, Ibaraki, 319-11

A method of neutron diffraction was developed to analyze nondestructively the residual stress in the interior of crystalline solids, and to evaluate the strength and fatigue damage of struturtal materials. The residual stress can be obtained from the neutron diffraction measurement of lattice strains in solids by using the theory of elasticity. The strains in three principal directions are required for stress calculation as shown in Fig. 1, where the axial, circumferencial and radial strains are measured at the same point in tubular samples.

The experiments were carried out by using the system developed for stress measurement at Guide Tube T2-1 of JRR-3M in Japan Atomic Energy Research Institute, called RESA. Bent crystals of silicon single crystals were used for a monochromator to increase the intensity of the nutron beam. A computerized system of positioning samples was developed on the goniometer to map the residual stress distribution. The accuracy was proved to reach a few tens of MPa.

The RESA system was applied to measure the distribution of the residual stress in various engineering strutural components. Figure 2 shows the weld joint of stainless steel tubes. The distribution of the axial residual stress in the shaded area in Fig. 2 was successfully obtained as shown in Fig. 3. The residual stress near the weld is tension near the interior surface of the tube, while compression near the outer surface. The RESA system was further applied to measure the distribution of the residul stress in tubular components made of Incoloy 908 to house super-conducting wires and in quenched steel tubes used for oil drilling. The sources of errors of stress measurements were identified as the determination of the stress-free lattice constant and the anistropy due to material textures. The mean stress in each phase of a composite of aluminum alloy reinforced with silicon particles was successfully measured by the neutron diffraction technique. The neutron diffraction method is concluded to be a potential nondestructive tool for evaluating the strength and fatigue damage of engineering components.

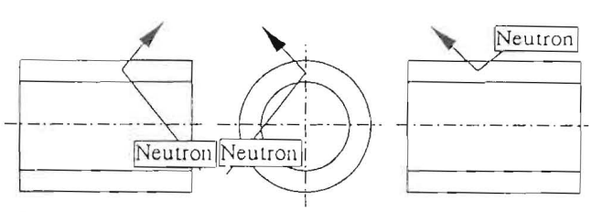

(a) Longitudinal Strain (b) Hoop Strain (c) Radial Strain

Fig. 1 Determination of three principal strain.

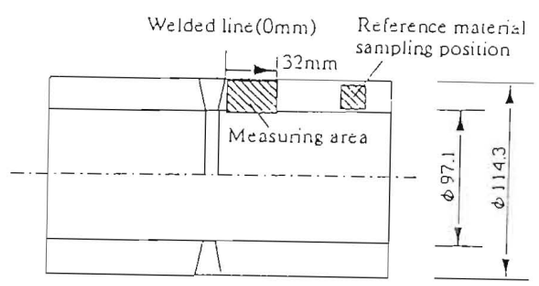

Fig. 2 Welded tube.

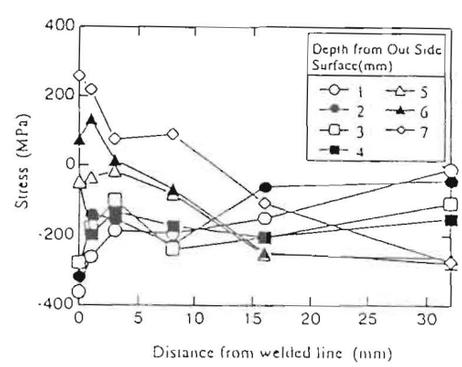

Fig. 3 Axial residual stress distribution in welded tube.

2.7.12 Residual Strain Measurements of a Heat Treated Steel Pipe

K.INOUE, H.KAWASHIMA, J.SAKAGUCHI, T.HORIKAWA,
N.MINAKAWA,[1] Y.TSUCHIYA[1], Y.MORII[1] and Y.YAMAGUCHI[2]

Fac. Sci. & Tech. Ryukoku Univ. Seta, Otsu 520-21, Japan
[1]Japan Atomic Energy Research Institute, Tokai-Mura, Ibaraki 319-11, Japan
[2]IMR Tohoku Univ. Aoba-ku, Sendai 980, Japan

The desired strength of the 13% Cr steel pipe for the oil well is obtained through suitable heat-treatment after plastic rolling. The pipe was quenched from 900℃ to the room temperature by spraying the water on the outer surface. The crystal structure of the material becomes bcc, owing to the martensitic transformation. As the rate of cooling is different at each position of the wall thickness, the residual strain appears.

To know the strain at each position of the wall thickness, we have made the neutron diffraction study and observed a small change of the lattice spacing in x,y,z three directions at intervals of 1mm of the wall thickness. RESA, a special neutron diffractometer for the measurements of residual strain, installed at T2-1 port in JRR-3M was used. The wave length of the neutron beam was 2.0107 Å. To observe a small area of the x(perpendiculr to the radius) and y(perpendicular to the circumference) planes, the size of the slit is 2×16mm^2 for incident beam and 2×20mm^2 for reflected beam, while to observe the z(perpendicular to the axis) plane, the slits of 2mm diameter for both incident and reflected beams were used. The (200) reflection of each plane was observed.

The photograph of the pipe installed on RESA is shown in Fig.1. The obtained thickness dependence of each lattice spacing is shown in Fig.2. It is found that, for x and y direction, the lattice is elongated at the middle area of the wall thickness and shrunk near both inner and outer surfaces. For z direction, none of the thickness dependence is observed. This fact for z direction is contrary to our expectation. Small (200) signal presumably due to the texture prevents the accurate measurements.

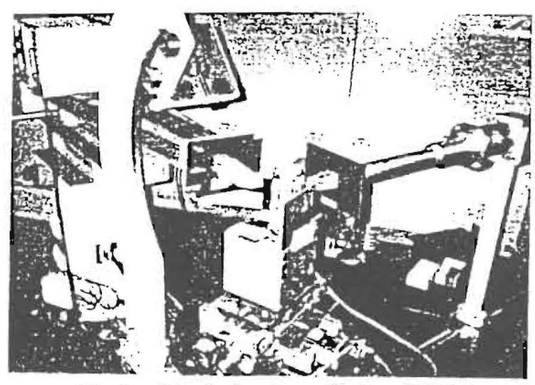

Fig.1 Steel pipe installed on RESA.

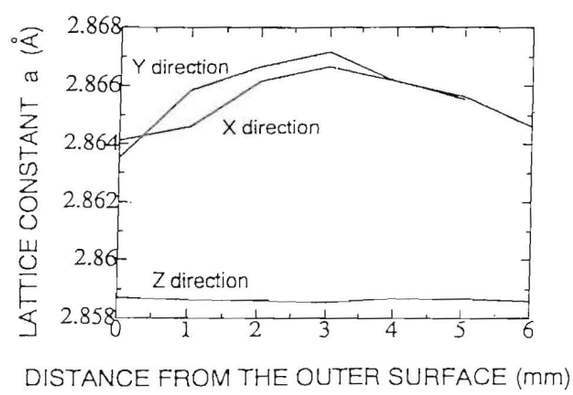

Fig.2 Thickness dependence of each lattice constant.

2.7.13

Residual Stress Measurement of Butt-Welded Stainless Steel Pipe by Neutron Diffraction

Shinobu Okido, Makoto Hayashi, Yukio Morii[1], Nobuaki Minakawa[1] and Yoshinori Tsuchiya[1]

Mechanical Engineering Research Laboratory, Hitachi, Ltd., Hitachi, Ibaraki, 317
1 Japan Atomic Energy Research Institute, Tokai, Ibaraki, 319-11

Structural components have differing characteristics based on their different heat and/or machining histories. Residual stresses appear around and in weldments, through heating and cooling processes. Tensile residual stress existing adjacent to weldments may induce stress corrosion cracking in certain environments[1]. The growth rate of stress corrosion cracking must be monitored in order to predict the remaining life of components. Residual stress measurement around welds is necessory to predict crack growth behavior. In the work described in this paper, the residual stress around the weld in a type 304 stainless steel pipe was measured using a residual stress analyzer (RESA) established in JRR3M.

The shape and dimensions of the stainless steel pipe used for the measurement is shown in Fig. 1. Measurement were taken at 0,1,3,8,16 and 32 mm away from the fusion line and the area for measurement was limited to 2 x 4 mm^2 limited by using a Cd slit. The reference lattice constant do which is the lattice constant without strain was measured at a distance of 4 mm away from the edge of the pipe using a 20 x 20 mm^2 aCd slit. Stresses were calculated by using Hooke's law from the strain values measured in three directions. The diffraction geometry for the welded pipe is shown in Fig. 2.

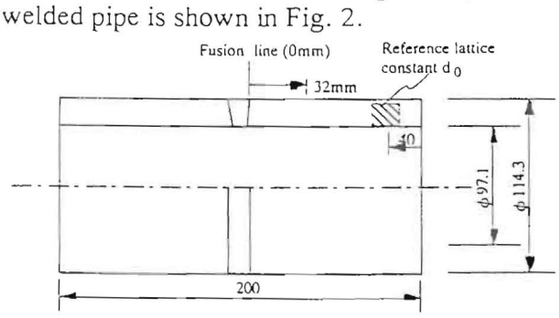

Fig. 1. Shape of stainless steel pipe.

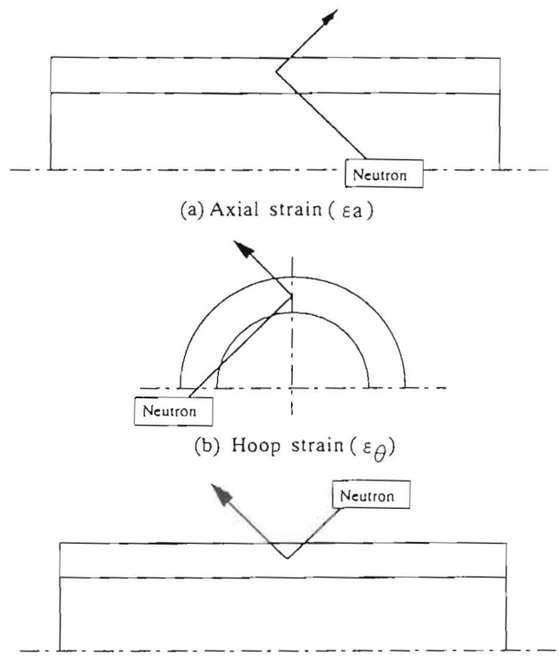

Fig. 2. Diffraction geometry for butt-welded pipe joint.

The residual strain distribution in the axial direction near the weldment is shown in Fig. 3. The axial residual strain on the fusion line was compressive except for the inner surface side. The compression strain was found at depths ranging from 1 to 5 mm from the outer surface decreased with the increasing distance from the fusion line, disappearing at a distance of 32 mm away from the fusion line. On the inner surface, the compressive strain increased with increasing distance from the fusion line.

The axial residual stress distribution near the fusion line is shown in Fig. 4. Compressive stresses between -300 and -400 MPa were

obtained on the fusion line at depths between 1 and 4 mm from the outer surface. The compressive axial residual stresses decrease to about -150 MPa at a distance of 3 mm away from the fusion line and likely to become to zero at 32 mm. At a depth of from the outer surface, the slightly remaining compressive stress on the fusion line decreased to 0 MPa at a distance of 3 mm away from the welded line and increased to -260 MPa at a distance of 32 mm. At the inner surface side, tensile ranging between 100 ~ 250 MPa residual stress was remained on the fusion line and decreased with the distance from the fusion line.

Comparison of the axial residual stresses measured by the neutron diffraction method and that calculated by the finite element method is shown in Fig. 5. The distribution pattern of the axial residual stresses agree with each other, but the values of residual stress differed about 50 MPa. Because the two methods had similar values for d_0 when a solution-treated type 304 stainless steel pipe was used, this error mey be explained by the uncertainly of d_0. Residual stress values measured by the neutron diffraction method depend on d_0. In applying the neutron diffraction method to evaluate residual stress in actual components, only the d_0 obtained at a location where the material receives a relatively small of heating and machining processes can be used. The alternative evaluation method of residual stress using X-ray had been provided by the Society of Material Science, Japan for solving this problem[2].

Additional discussion is necessary to be able to use the method by neutron diffraction in the future.

References

[1] K. Hirano at al.: Material Science in Japan,47(1996)740.
[2] Standard of stress measurement by X-ray:Yokendo(1982).

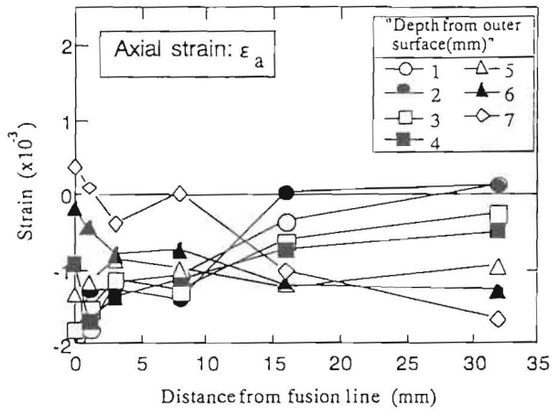

Fig. 3. Axial residual strain distribution in welded pipe.

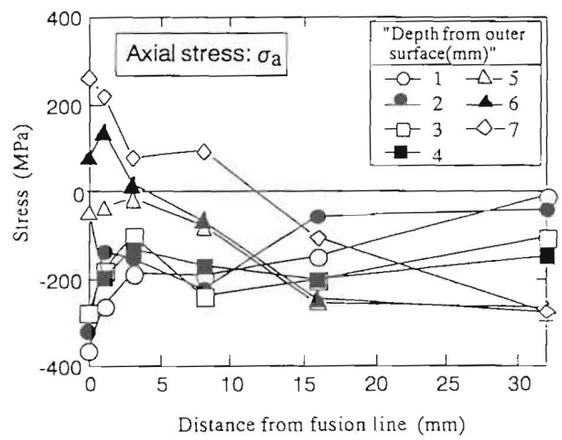

Fig. 4. Axial residual stress distribution in welded pipe

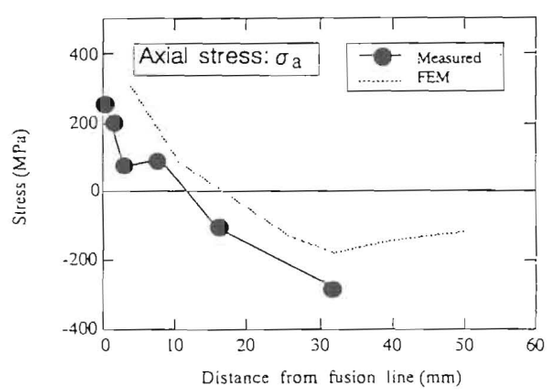

Fig. 5. Comparison of residual stress on the inside surface by the neutron diffraction method and finite element method.

2.7.14 RESIDUAL STRESS OF A JACKET MATERIAL FOR ITER SUPER-CONDUCTING COIL

Y. Tsuchiya, N. Minakawa, Y. Morii, T. Kato[1], H. Nakajima[1], K. Hamada[1], I. Watanabe[1], K. Ishio[1], T. Abe[1] and H. Tsuji[1]

Advanced Science Research Center, Japan Atomic Energy Research Institute, Ibaraki 319-11 Japan
[1]Naka Fusion Research Establishment, Japan Atomic Energy Research Institute, Ibaraki 319-01 Japan

The jacket material, Incoloy 908, of the central solenoid coil (CS coil) for International Thermonuclear Experimental Reactor (ITER) is a nickel-iron based precipitate hardening type superalloy. Incoloy 908 has a possibility of fracture due to Stress Accelerated Grain Boundary Oxidation (SAGBO) in the region of tensile residual stress above 200MPa with under the conditions of temperature region of 500~850°C and atmosphere of oxygen concentration above 0.1ppm. The heat treatment of CS coil will be performed at 650°C for 240hours. If the residual stress of the jacket exceeds 200MPa, there is a risk of fracture by SAGBO at the heat treatment. In order to avoid SAGBO condition in the jacket, we performed internal residual stress measurement of the jacket using neutron diffraction method.

The sample is a part of CS coil before heat treatment with length of 150mm and cross section of 45 × 45mm^2. It was bent with radius of 500 mm. The jacket part of the coil is made of Incoloy 908 that shows FCC phase. The thickness of the jacket for the measurement is 4.5 mm. A solid solution of Incoloy 908 was used as the standard sample of stress-free condition. Neutron diffraction measurements were carried out with the neutron diffractometer, RESA, installed at JRR-3M in JAERI. The incident beam wave length of 2.155Å was used. In order to define the sampling volume within the sample, incident beam and scattering beam slit of 2 × 4mm^2 were set before and after the sample. The elastic constants evaluated by a tensile test using neutron diffraction on the triple-axis neutron spectrometer, TAS-2, installed at JRR-3M in JAERI with a loading machine.

For the three principal orientations x, y and z corresponding to longitudinal, transverse and vertical directions of the sample, (111) plane spacings were measured scanning from outer surface to inside of the jacket by RESA. A depth dependence of the lattice strain in the jacket sample was obtained from the (111) plane spacing. On the other hand, Young's modulus and Poisson's ratio for (111) plane were estimated at E=133GPa and ν=0.168, respectively, from stress-strain curve by the tensile test on TAS-2. A residual stress was calculated from the lattice strain, Young's modulus and Poisson's ratio using Hooke's law for the three orientations of the jacket. The residual stress distributions of the CS coil jacket are shown in fig. 1. The residual stresses for each direction at the outside of the jacket are in compress. σ_x shows almost constant residual stress of compress for the measurement region. σ_y and σ_z increase with depth of jacket and show a tensile residual stress at the inside region of the jacket. The tensile residual stresses for y and z directions exceed 200MPa. The result shows that the CS coil jacket is in the SAGBO condition for residual stress at some regions.

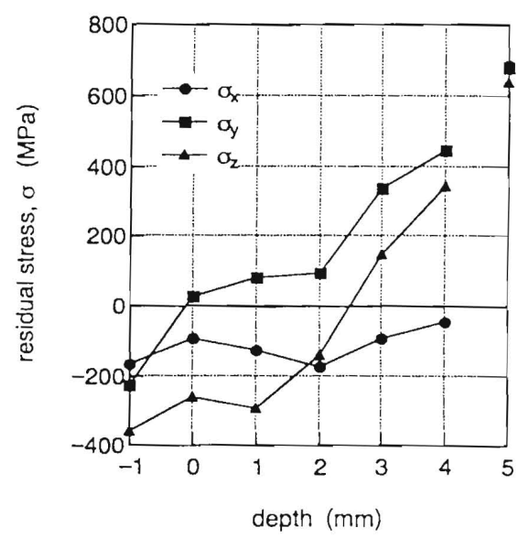

Fig. 1. The residual stress distributions for the three principal orientations of the CS coil jacket. Depth of zero mm shows just the outer surface of the sample.

APPENDIX A

Neutron Scattering Research Committee of 1996

(Chairman)	Nobuyoshi	Wakabayashi	Professor, Faculty of Science and Technology, Keio University
(Vice-Chairman)	Shinzo	Saito	Deputy Director General, Tokai Research Center
	Hironobu	Ikeda	Professor, National Laboratory for High Energy Physics
	Yasuo	Ito	Associate Professor, Researh Center for Nuclear Science and Technology, the University of Tokyo
	Masahiko	Utsuro	Professor, Research Reactor Institute, Kyoto University
	Yasuo	Endoh	Professor, Graduate School of Science, Tohoku University
	Koichi	Katsumata	Principal Researcher, The Institute of Physical and Chemical Research
	Nobuhiro	Go	Professor, Faculty of Science, Kyoto University
	Takeji	Hashimoto	Professor, Graduate School of Engineering, Kyoto University
	Makoto	Hayashi	Department Manager, Mechanical Engineering Research Laboratory, Hitachi Ltd.
	Hironobu	Fujii	Professor, Faculty of Integrated Arts and Sciences, Hiroshima University
	Yasuhiko	Fujii	Professor, the Institute for Solid State Physics, the University of Tokyo
	Yasuo	Yamaguchi	Professor, Institute for Materials Research, Tohoku University
	Hideo	Ohno	Director, Advanced Photon Research Center (JAERI Kansai)
	Satoru	Funahashi	Director, Department of Materials Science and Engineering, Tokai Research Establishment
	Shiro	Nagai	Deputy Director, Advanced Science Research Center
	Fumio	Sakurai	General Manager, Tokai Research Establishment
	Nobuo	Niimura	Invited Researcher, Advanced Science Research Center
	Toru	Ogawa	Principal Scientist, Tokai Research Establishment
	Yasusada	Yamada	Invited Researcher, Advanced Science Research Center
	Yukio	Morii	Principal Scientist, Advanced Science Research Center
(Secretary)	Shuji	Takagi	Head, Advanced Science Research Center
	Susumu	Katano	Principal Scientist, Advanced Science Research Center

APPENDIX B

Themes of Cooperative Research Projects with Universities in JFY 1996

1.	Study on Superconducting Materials and Low-Dimensional Spin Systems	J. Akimitsu	Aoyama Gakuin Univ.
2.	Vortex Structures in Large Anisotropic Superconductors	K. Osamura	Kyoto Univ.
3.	Correlations between Superconducting Properties and Crystal Structures in High-Tc Superconductors	Y. Koike	Tohoku Univ.
4.	Magnetic Structure and Magnetic Excitaiton in the Strongly Correlated Ce-Pnictides Systems	M. Kohgi	Tokyo Metropolitan Univ.
5.	Structural Fluctuations and Transport Properties in Oxides Conductors	Y. Yamada	Waseda Univ.
6.	Magnetic Structure and Lattice Distortion in Frastrated Antiferromagnet in RMn_2	M. Shiga	Kyoto Univ.
7.	Pattern Formation in Multicomponent Polymer Alloy	T. Hashimoto	Kyoto Univ.
8.	Static Hierarchical Structure of Multicomponent Macromolecular Systems	Y. Izumi	Yamagata Univ.
9.	Development of Dilution Refrigerators for Neutron Experiments	M. Kubota	The Univ. of Tokyo
10.	Study of Neutron Powder Diffraction with MEM Method	K. Ishida	Science Univ. of Tokyo
11.	Neutron Reflectometry for the Study of Polymer Interfaces	Y. Matsushita	The Univ. of Tokyo
12.	Study of Neutron Optics with Dynamical Diffraction Effect	T. Takahashi	The Univ. of Tokyo
13.	Study of Internal Damage for Metals by Neutron Diffraction Method	T. Horikawa	Ryukoku Univ.
14.	Study of Structural Phase Transition under a High Pressure of Alkari Halides	A. Onodera	Osaka Univ.
15.	Study of Structural Phase Transition in Dielectric Compounds at Low Temperature	Y. Noda	Chiba Univ.

16.	Study on Crystal Structures and Physical Properties of Electronic Device Materials	T. Kajitani	Tohoku Univ.
17.	Study on Superionic Conductors and Proton Conductive Materials	M. Nagasaki	Nagoya Univ.
18.	Study of Magnetic Structure and Phase Transition of γ -Mn Alloy	T. Hori	Shibaura Inst. Tech.
19.	Study of Magnetic Structure	Y. Hinatsu	Hokkaido Univ.
20.	Development of Non-destructive Method for Evaluation of Material Strength	K. Tanaka	Nagoya Univ.

APPENDIX C

Themes of Cooperative Research Projects with Private Enterprises and National Laboratories in JFY 1996

1.	Residual Stress Measurement by Neutron Diffraction	M. Hayashi	Hitachi Ltd.
2.	SANS Study on Miscibility and Phase Separation of Multicomponent Polymer Blend	H. Jinnai	Japan Science and Technology Corporation
3.	NDT-observation of the Ni-based Superalloy Single Crystals	A. Yoshinari	Hitachi Ltd.
4.	Neutron Scattering Study on Magnetism of Materials Related to High-Tc Superconductors	K. Katsumata	RIKEN
5.	Diffuse Scattering Studies of Ag_3SI	Aziz K. Jahja	BATAN
6.	Structure of Solid	F. Izumi	National Institute for Research in Inorganic Materials
7.	SANS Study of Nanocrystalline Alloys	M. Ohnuma	National Research Institute for Metals

APPENDIX D
Publication List in the Period of JFY 1996

1. Small- Angle Neutron Scattering Study of Amorphous Mixing Behaviors in Deuterated Polystyrene/poly(vinyl methyl ether) Mixtures near the Glass Transition Temperature
H. Takeno, S. Koizumi, H. Hasegawa, and T. Hashimoto
Macromolecules **29** (1996) 2440-2448

2. Observation of Magnetic Flux Distribution in Type II Superconductors by Means of Small Angle Neutron Scattering
K. Osamura[*1], S. Miyata, M. Kosaka[*2], and J. Suzuki ([*1]Kyoto Univ. , [*2]KEK)
Ouyo Butsuri **65-4** (1996) 367-371

3. Neutron Scattering Studies of the Effects of Uniaxial Stress and Ageing on the β_1-Cu-Al-Zn Alloy
A. Nagasawa[*], M. Yamada[*], and Y. Morii ([*]Nara Wemen's Univ.)
J. Phys. Soc. Jpn. **65** (1996) 778-781

4. Polaron Ordering in Low-doping $La_{1-x}Sr_xMnO_3$
T. Inami, Y. Yamada[*], M. Hino[*], S. Noudo[*], R. Kaneo[*], and S. Katano ([*]Waseda Univ.)
Phys. Rev. Lett. **77-5** (1996) 904-907

5. The Phase Diagram of the New Superconductor $Sr_2CuO_2(Co_3)_{1-x}(BO_3)_x$
S. Katano, S. Nakada[*], H. Okajima[*], T. Yokoo[*], A. Yamashita[*], and J. Akimitsu[*] ([*]Aoyama Gakuin Univ.)
Physica C **263** (1996) 344-348

6. Correlation between Superconductivity Electronic State and Crystal Structure in $La_{2-y-x}Bi_yBa_xCuo_4$
S. Katano, S. Takeuchi[*], C. Imazawa[*], M. Kato[*], Y. Ono[*], T. Kajitani[*], and Y. Koike[*] ([*]Tohoku Univ.)
Physica C **263** (1996) 298-301

7. Magnetization Process of the Trianguler Lattice Antiferromagnets, $RbFe(MoO_4)_2$ and $CsFe(SO_4)_2$
T. Inami, Y. Amishiro[*1], and T. Goto[*2] ([*1]Fukui Univ., [*2]The Univ. of Tokyo)
J. Phys. Soc. Jpn. **65-8** (1996) 5601-5603

8. Measurement of Internal Stress of Ceramics by Neutron Diffraction Method
Y. Sakaida[*1], K. Tanaka[*2], S. Harada[*1], N. Minakawa, Y. Morii, and Y. Ikeda[*1]
([*1]Fine Ceramics Center, [*2]Nagoya Univ.)
Transactions of the Japan Society of Mechanical Engineers 96 **62-600** (1996) 1924-1930

9. Double Magnetic Transition in UPt_2In
Y. Maeda[*1], T. Takabatake[*1], Y. Bando[*1], H. Fujii[*1], K. Oda[*2], K. Sugiyama[*2], K. Kindo[*2], K. Izawa[*1], T. Suzuki[*1], T. Fujii[*1], and Y. Morii ([*1]Hiroshima Univ., [*2]Osaka Univ.)

Physica B **223-224** (1996) 228-230

10. Magnetic Properties and Magnetic Phase Diagram of bcc Cr-Fe-Mn Alloys
Y. Tsuchiya, T. Bitoh[*1], S. Murayama[*2], S. Chikazawa[*2], and Y. Hamaguchi
([*1]ALPS Electric Co., Ltd., [*2]Muroran Institute of Technology)
J. Phys. Soc. Jpn **65** (1996) 3289-3293

11. Obsevation of Non-linear Effects in a Quasi-One-Dimentional Antiferromagnet : Magnetic Excitations in $CsVCl_3$
T. Inami, K. Kakurai[*1], and H. Tanaka[*2] ([*1]The Univ. of Tokyo, [*2]Sophia Univ.)
J. Phys. : Condens. Matt. **9** (1997) 1357-1368

12. Reactor Neutron
Y. Morii and M. Isshiki
RADIOISOTOPES **45-11** (1996) 717-721

13. Diffuse Neutron Scattering from Superionic Phase of Ag_2Te
T. Sakuma[*], T. Aoyama[*], H. Takahashi[*], Y. Shimojo, and Y. Morii ([*]Ibaraki Univ.)
Solid State Ionics **86-88** (1996) 223-230

14. A Neutron Reflectometer Installed at the Cold Neutron Triple-Axis Spectrometer (LTAS, C2-1) in JRR-3M
K. Soyama, N. Metoki, N. Minakawa, Y. Morii, N. Torikai[*1], and Y. Matsushita[*2]
([*1]Nagoya Univ., [*2] The Univ. of Tokyo)
J. Phys. Soc. Jpn. **65** Suppl. A (1996) 133-135

15. Neutron Polarization Control by Interferometer
S. Nakatani[*], T. Takahashi[*], H. Tomimitsu, and S. Kikuta[*] ([*]The Univ. of Tokyo)
J. Phys. Soc. Jpn. **65** Suppl. A (1996) 77-79

16. NDT-Observation of Superalloy Single Crystals Grown Into the Gas-Turbine Blade
H. Tomimitsu, K. Iijima[*], K. Aizawa, and A. Yoshinari[*] ([*]Hitachi Ltd.)
J. Phys. Soc. Jpn. **65** Suppl. A (1996) 252-254

17. SANS Study on Static Structure formed by Block Copolymer
S. Koizumi
Kaigai Kobunshi Kenkyu (1996) 16-17

18. Microheterogeneities of Polymer Blends near the Glass Transition Temperature
H. Takeno[*], S. Koizumi, H. Hasagawa[*], and T. Hashimoto[*] ([*]Kyoto Univ.)
Kobunshi Ronbunshu **53-12** (1996) 846-851

19. Molecular Form and Stereoregularity of Polystyrenes in Glassy State
M. Kobayashi[*], S. Hanafusa[*], T. Yoshioka[*], and S. Koizumi ([*]Osaka Univ.)

Kobunnshi Ronbunshu **53-10** (1996) 575-581

20. Magnetic Phase Diagram of CeP
M. Kohgi[*1], T. Osakabe, K. Iwasa, J. M. Mignot[*2], I. N. Goncharenko[*2,3], Y. Okayama[*4], H. Takahashi, N. Mori[*5], Y. Haga[*1], and T. Suzuki[*6]
([*1]Tokyo Metropolitan Univ. , [*2]CEA-CNRS, [*3]Kurchatov Institute, [*4]Saga Univ., [*5]The Univ. of Tokyo, [*6]Tohoku Univ.)
J. Phys. Soc. Jpn. **65** Suppl. B (1996) 99-104

21. Effect of Tb Substitution on the Helical Modulation Vector of YMn_2
H. Nakamura[*], M. Shiga[*], and N. Metoki ([*]Kyoto Univ.)
J. Magn. Magn. Mater. **163** (1996) L1-L4

22. Pulse Neutron Source in the Next Generation - Long Pulse and Short Pulse
Y. Morii and Y. Oyama (Eds.)
JAERI-memo **09-100** (1997)

23. Options for a Next Generation Neutron Source for Neutron Scattering Based on the Projected Linac Facility at JAERI
F. Mezei[*], N. Watanabe, N. Niimura, Y. Morii, K. Aizawa, and J. Suzuki ([*]Hahn-Meitner-Institut)
JAERI-Tech **97-019** (1997)

24. Meganetic Microstructures Produced by Compositional Separation in Co-Cr Based Alloy Thin Films
Y. Maeda[*], D. J. Rogers[*], O. Song[*], K. Takei[*], T. Ohkubo[*], S. Hirono[*], J. Suzuki, and Y. Morii
([*]NTT)
IEEE Trans. Magn. **33-1** (1997)

25. Novel Magnetic Structures of the Low-carrier System CeP under High Pressure
T. Osakabe, M. Kohgi[*1], K. Iwasa[*1], N. Nakajima[*1], J. M. Mignot[*2], I. N. Goncharenko[*2,3], Y. Okayama[*4], H. Takahashi[*5], N. Mohri[*5], Y. Haga, and T. Suzuki[*6]
([*1]Tokyo Metropolitan Univ., [*2]CEA-CNRS, [*3]Kurchatov Institute, [*4]Saga Univ., [*5]The Univ. of Tokyo, [*6]Tohoku Univ.)
Physica B **230-232** (1997) 645-648

Author Index

A T. Abe 2.7.14
T. Adachi 2.3.11
K. Aizawa 2.1.3, 2.4.2, 2.4.3, 2.5.9, 2.7.1, 2.7.2
J. Akimitsu 2.2.3
F. Amita 2.7.5
Y. Aratono 2.7.4
N. Aso 2.3.1, 2.3.4

E A. Endo 2.5.9
Y. Endoh 2.3.4

F O. Fujii 2.2.3
S. Fujiwara 2.6.2
S. Fukui 2.7.5
A. Fukushi 2.5.7
S. Funahashi 2.2.5

G N. Gose 2.5.6

H Y.Haga 2.3.1, 2.3.2, 2.3.3, 2.3.5, 2.3.6, 2.3.7
K. Hamada 2.7.14
Y. Hamaguchi 2.1.4
J. Harada 2.6.1
H. Hasegawa 2.5.4
Y. Hasegawa 2.7.1, 2.7.2
T. Hashimoto 2.5.2, 2.5.3, 2.5.4, 2.5.5
H. Hayashi 2.4.1
M. Hayashi 2.7.11, 2.7.13
M. Hedo 2.3.7
Y. Hinatsu 2.2.4
O. Hino 2.3.9
Y. Hirokawa 2.5.5
K. Hojou 2.2.5
K. Hono 2.4.4

H T. Hori 2.2.5
T. Horikawa 2.7.12

I S. Ichimura 2.7.5
N. Ikeda 2.3.9
T. Inaguma 2.7.6
Y. Inaguma 2.1.3
T. Inami 2.3.9, 2.3.10, 2.7.7
K. Inoue 2.7.11, 2.7.12
K. Ishida 2.1.8
Y. Ishii 2.1.2, 2.1.4, 2.1.5, 2.1.6, 2.1.8, 2.4.5
K. Ishio 2.7.14
Y. Isono 2.5.7
M. Itoh 2.1.3
D. Iwanaga 2.1.3
K. Iwase 2.3.6
T. Iwata 2.4.3
F. Izumi 2.1.9
Y. Izumi 2.5.9

J Aziz K. Jahja 2.1.4
H. Jinnai 2.5.5

K H. Kadowaki 2.3.7
K. Kakurai 2.3.7
T. Kajitani 2.2.6
Y. Karasawa 2.6.2, 2.7.10
S. Katano 2.2.3, 2.3.9, 2.3.10, 2.3.11, 2.4.1, 2.7.5, 2.7.7
T. Kato 2.7.14
K. Katsumata 2.3.10
S. Kawano 2.1.5, 2.7.5
H. Kawashima 2.7.12
S. Kikuta 2.7.2

K	K. Kimishima	2.5.5
	T. Kobayashi	2.1.8
	M. Kohgi	2.3.6
	Yoji Koike	2.3.11
	Yoshihiro Koike	2.2.1, 2.3.1, 2.3.2, 2.3.3, 2.7.6
	S. Koizumi	2.5.1, 2.5.2, 2.5.3, 2.5.4, 2.5.5, 2.5.6, 2.5.7, 2.5.9
	K. Komagushi	2.7.4
	T. Komatsubara	2.3.4
	N. Koshizuka	2.3.8
	T. Kumada	2.7.4
	S. Kumazawa	2.1.8, 2.6.1
	M. Kubota	2.7.6
	K. Kuroda	2.3.8
M	O. Makino	2.5.2, 2.5.3
	M. Matsuda	2.3.10
	T. Matsui	2.1.2
	T. Matsumoto	2.7.4
	Y. Matsushita	2.5.8
	N. Metoki	2.2.1, 2.2.2 2.3.1, 2.3.2, 2.3.3, 2.3.4, 2.3.7, 2.5.8
	Y. Michiue	2.1.9
	N. Minakawa	2.1.4, 2.7.8, 2.7.11, 2.7.12, 2.7.13, 2.7.14
	Y. Minezaki	2.6.2
	S. Miyata	2.3.8
	T. Miyazaki	2.7.4
	A. Mori	2.1.5, 2.1.6
	A. Moriai	2.7.5, 2.7.7
	Y. Morii	2.1.1, 2.1.2 2.1.3, 2.1.4, 2.1.5, 2.1.6, 2.1.8, 2.1.9, 2.2.1, 2.5.7, 2.5.8, 2.7.6,
M		2.7.8, 2.7.12, 2.7.13, 2.7.14
N	T. Nagasaki	2.1.2
	H. Nakajima	2.7.14
	A. Nakamura	2.2.7
	H. Nakamura	2.2.2
	Y. Nakamura	2.4.5
	N. Niimura	2.6.1, 2.6.2, 2.7.8, 2.7.9
	M. Nishi	2.2.3
	N. Nitani	2.2.4
	N. Noda	2.1.2
	Y. Noda	2.1.1
O	T. Ogawa	2.4.1
	Y. Ohashi	2.6.1
	Y. Ohgo	2.6.1
	T. Ohhara	2.6.1
	M. Ohnuma	2.4.4
	A. Ohtomo	2.7.5
	Y. Oka	2.2.6
	T. Okamoto	2.5.5
	Y. Okamoto	2.4.1
	S. Okido	2.7.13
	Y. Ono	2.2.6
	A. Onodera	2.1.5 2.1.6, 2.7.5
	H. Onodera	2.4.1
	Y. Onuki	2.2.1, 2.3.1, 2.3.2, 2.3.3 2.3.5, 2.3.7
	T. Osakabe	2.3.5, 2.3.6
	K. Osamura	2.3.8
S	S. Saito	2.5.3
	J. Sakaguchi	2.7.12
	A. Sakakibara	2.5.9
	T. Sakuma	2.4.5
	S. Sasaki	2.5.6
	H. Sato	2.3.11

S	K. Sato	2.2.6
	N. Sato	2.3.4
	T. Sato	2.2.6
	R. Settai	2.2.1
	S. Shamoto	2.2.6
	M. Shiga	2.2.2
	Y. Shimojo	2.1.3, 2.1.9, 2.2.4, 2.2.5, 2.4.5, 2.7.8
	G. Shin	2.5.3
	M .Shirase	2.3.5
	H. Shiratori	2.2.5
	K. Soyama	2.7.3
	K. Sugimoto	2.1.8
	S. Suehiro	2.5.2, 2.5.3
	J. Suzuki	2.3.7, 2.3.8, 2.4.4
	T. Suzuki	2.3.6
T	T. Takabayashi	2.3.5
	H. Takahashi	2.4.5
	T. Takahashi	2.7.1
	A. Takano	2.5.7
	T. Takayanagi	2.7.4
	H. Takeno	2.5.4
	H. Tamaki	2.4.2
	I. Tamura	2.1.1
	I. Tanaka	2.6.1, 2.6.2, 2.7.9
	K. Tanaka	2.7.11
	K. Tashiro	2.5.6
	H. Tomimitsu	2.4.2, 2.4.3, 2.5.9, 2.7.1, 2.7.2
	N. Torikai	2.5.8
	Y. Tuchiya	2.2.5, 2.4.1, 2.7.11, 2.7.12, 2.7.13, 2.7.14
	H. Tsuji	2.7.14
W	I. Watanabe	2.7.14
	M. Watanabe	2.1.9
Y	Y. Yamada	2.3.9
Y	Y. Yamaguchi	2.7.12
	E. Yamamoto	2.3.5, 2.3.7
	Y. Yonezawa	2.6.2
	Y. Yoshida	2.2.1
	K. Yoshii	2.2.7
	A. Yoshinari	2.4.2